

ALMA MATER STUDIORUM · UNIVERSITÀ DI BOLOGNA

---

Scuola di Scienze  
Dipartimento di Fisica e Astronomia  
Corso di Laurea in Fisica

# Performance study of Kalman Filter track reconstruction algorithms in the FOOT experiment

**Relatore:**  
Prof. Mauro Villa

**Presentata da:**  
Francesca Neri

**Correlatore:**  
Dott. Matteo Franchini

Anno Accademico 2016/2017



## Abstract

Negli ultimi anni, il rapido progresso tecnologico ha portato all'evoluzione delle tecniche di radiazione oncologica, tra cui spicca il trattamento conosciuto come *adroterapia*, che utilizza particelle cariche come protoni e ioni carbonio. Il vantaggio rispetto alla radioterapia convenzionale, che utilizza raggi X e  $\gamma$ , è la peculiare curva di rilascio di dose di particelle cariche nei tessuti, che presenta un massimo localizzato (picco di Bragg), alla fine del cammino nel mezzo. L'obiettivo di un trattamento adroterapico è la localizzazione della massima dose nel volume tumorale e il rilascio della minor dose possibile ai tessuti sani circostanti. Oggigiorno, il Treatment Planning System (TPS) non considera appieno gli eventi di frammentazione, sia del bersaglio di materia organica nel caso di fasci di protoni, sia del proiettile in caso di fasci di ioni pesanti. Questa pratica clinica può portare alla sottostima della dose rilasciata nei tessuti sani e negli organi a rischio, compromettendo così l'efficacia del trattamento.

Il nuovo esperimento FOOT (FragmentatiOn Of Target) si incarica di sopperire alla mancanza di dati sperimentali sulla sezione d'urto dei frammenti prodotti nell'interazione tra particelle cariche (protoni e ioni pesanti come  $^{12}\text{C}$ ,  $^4\text{He}$  e  $^{16}\text{O}$ ) e tessuti biologici alle energie di  $\sim 200\text{-}400$  MeV/u. Questi dati saranno essenziali sia per il miglioramento dei trattamenti di adroterapia, sia per lo studio e l'ottimizzazione di meccanismi di radioprotezione per gli astronauti in orbita, sottoposti ai violenti raggi cosmici. L'apparato di FOOT consiste in un sistema di tracking in campo magnetico ad alta precisione ed utilizzando l'approccio di cinematica inversa, permette il calcolo della sezione d'urto differenziale di frammentazione nucleare con un'incertezza minore del 5%. La ricostruzione delle tracce si basa sul software SHOE (Software for Hadrontherapy Optimization Experiment), che utilizza il toolkit GENFIT ed il suo algoritmo Kalman di ricostruzione.

Questa tesi si occupa dello studio di metodi per l'ottimizzazione della ricostruzione delle tracce, focalizzandosi in particolare sul filtro di Kalman e le sue performances nell'esperimento FOOT.



# Contents

<b>Introduction</b>	<b>1</b>
<b>1 Interaction of Radiation with Matter</b>	<b>4</b>
1.1 Photons	4
1.1.1 Photoelectric Effect	6
1.1.2 Compton Scattering	6
1.1.3 Electron Pair Production	7
1.2 Electrons and Positrons	7
1.3 Heavy Charged Particles	8
1.3.1 The Bethe-Block Formula and Stopping Power	8
1.3.2 Penetration Range	10
1.3.3 Nuclear Fragmentation	12
1.4 Radiobiology: Physical and Biological Aspects	13
1.4.1 Radiation Effect on Cells	14
1.4.2 Absorbed Dose	15
1.4.3 Linear Energy Transfer	16
1.4.4 Relative Biological Effectiveness	16
1.4.5 Oxygen Enhancement Ratio	17
<b>2 Applications in Modern Science</b>	<b>19</b>
2.1 Cancer Treatment	19
2.1.1 Radiotherapy	20
2.1.2 Hadrontherapy	24
2.2 Radio-protection in Space	33
2.2.1 Galactic Cosmic Radiation	35
2.2.2 Solar Particle Events	36
<b>3 The FOOT (FragmentatiOn Of Target) experiment</b>	<b>37</b>
3.1 Measurements of target fragmentation	38
3.1.1 Inverse kinematic	38
3.1.2 Target Material	39

3.2	The FOOT apparatus design criteria . . . . .	41
3.2.1	Heavy Ions Setup . . . . .	41
3.2.2	Light Charged Particles Setup . . . . .	47
3.3	Expected Performances . . . . .	49
3.3.1	Momentum measurement . . . . .	50
3.3.2	Particle identification . . . . .	50
<b>4</b>	<b>Tracking</b>	<b>56</b>
4.1	Kalman Filter . . . . .	58
4.2	GENFIT . . . . .	61
4.2.1	GENFIT Modular Design . . . . .	61
4.3	Software, SHOE . . . . .	64
4.3.1	Simulation . . . . .	64
4.3.2	Reconstruction . . . . .	67
4.4	Current Status of the Momentum Reconstruction . . . . .	69
<b>5</b>	<b>Kalman Filter Performance in FOOT</b>	<b>71</b>
5.1	The Code . . . . .	72
5.2	Tests and Results . . . . .	73
5.3	Perspectives . . . . .	83
	<b>Conclusions and Perspectives</b>	<b>84</b>

# Introduction

Cancer is one of the major widespread health problems and a leading cause of death worldwide, accounting for 8.8 million deaths in 2015, according to World Health Organization (WHO).

Nowadays there are different techniques to treat neoplastic diseases. Although, when possible, surgery is considered a standard treatment approach to remove or reduce the solid tumor, most of cancer diagnosed patients receive support treatment to surgical removal. One of the most widespread option is radiation therapy, used as therapeutic or adjuvant treatment. In recent years, the rapid advance in technology has led to the evolution of radiation oncology techniques, bringing an alternative to conventional radiotherapy, which uses X and  $\gamma$  rays, in favor of Charged Particle Therapy, also called *hadrontherapy*. Particle Therapy exploits accelerated charged hadrons ( $\sim 200$ - $400$  MeV/u energy), such as protons or heavy ions like  $^{12}\text{C}$ ,  $^4\text{He}$  and  $^{16}\text{O}$ .

The main advantage of hadrontherapy lies in its specific dose release profile which outlines a low dose at the beginning of the path, a maximum release in a narrow region called "Bragg Peak" at the end of the path and almost no dose beyond the peak. The particle range inside a target strongly depends on the initial energy of the particle beam. For this reason, the Bragg Peak depth can be varied changing the beam parameters and allowing so a high irradiation accuracy of the tumor volume, depositing the maximum of the dose on the cancer region and sparing the surrounding healthy tissues. Furthermore, the increase in Linear Energy Transfer (LET), which is the energy deposition by a ionizing radiation along its path in a tissue, in the Bragg Peak region induces an enhanced biological effectiveness in cancerous cell killing, compared to conventional radiotherapy. The higher radiobiological effectiveness results from a higher capability of producing direct Double Strand Breaks (DSB) to the DNA helix of tumor cells. Nowadays charged particles are used to treat deep sited tumors, due to both the high localization of their dose release and the sparing of organs at risk surrounding the tumor volume.

Notwithstanding the effectiveness of hadrontherapy and its increasing use in patient treatment worldwide, there is a lack of experimental measurements of nuclear reaction cross sections for fragments produced during the interaction of hadrons with biological target nuclei (H, C, N, O, Ca). These data are required to improve the precision of the treatments with protons and heavy ions, since different studies have shown a possi-

ble underestimate or overestimate of the biological effectiveness assumed in the current treatment planning systems.

In proton therapy, the nuclear inelastic interactions of the incident beam with the target tissues may lead to the fragmentation of the target nuclei, producing a significant variation in local dose deposition, as studies show that the heavy particles produced by fragmentation have small ranges. At present, in treatment planning, the proton Relative Biological Effectiveness (RBE) is assumed to have a constant value of 1.1, which can lead to an underestimation of the biological damage in the entrance channel (plateau region in the Bragg curve).

In heavy ions treatments the fragmentation process results in the break up of the incident particle. The projectile fragments are produced mostly in the forward direction causing the collateral effect of an overdose delivered to tissues beyond the tumor volume.

In order to improve the knowledge on nuclear fragmentation in the hadrontherapy energy range, the measure of cross sections for both heavy fragments ( $Z \geq 2$ ) produced by target fragmentation in proton therapy and for projectile fragmentation of carbon and oxygen beams are needed.

The measurements of nuclear fragmentation are crucial even for other applications, like radioprotection in space. NASA and other space agencies have started since several years the study of health risk assessment for astronauts during long lasting space exploration journeys. Space is, in fact, an unsafe environment for humans as the high uncertainty on precise risk estimates and the lack of effective countermeasures make cosmic radiation one of the main health concerns for space exploration.

The FragmentatiOn On Target (FOOT) experiment is a INFN project devoted to cover the missing and needed nuclear measurements in these hadrontherapy and space exploration fields. The FOOT main goal is the measurement of the differential nuclear fragmentation cross section for particles used for hadrontherapy or radioprotection purpose with an uncertainty of less than 5%. The measurement performed by the FOOT experiment could be crucial for the design and optimization of spacecraft shielding and for a better understanding of radiation induced damage. For these reasons, a detailed knowledge of the fragmentation processes is strongly required.

The general idea of FOOT is to design a portable experimental setup, able to detect those fragments of interest. The apparatus should be easily transportable allowing data taking in various treatment and research centers.

Unfortunately, it is hard to achieve the desired acceptance for all secondary fragments with an apparatus of limited size. Considering that lower mass fragments can be emitted within a wider angular aperture with respect to heavier nuclei, the FOOT experiment will operate with two different and complementary setups:

- **Heavy Ions Setup:** a setup based on electronic detectors and a magnetic spectrometer, covering an angular acceptance of 10-20° with respect to the beam axis, for the identification and measurements of fragments heavier than  $^4\text{He}$ .

- **Light Ions Setup:** a setup with an emulsion spectrometer for the detection of fragments at large angles ( $\sim 70^\circ$ ); a specific emulsion chamber is needed to measure the production of light charged fragments as protons, deuterons, tritons and alpha particles.

To measure the fragment production due to protons and heavier ions, we need to study the impact of carbon and oxygen beams ( $\sim 100\text{-}300$  MeV/u) on a  $\text{C}_2\text{H}_4$  target. In fact, in order to overcome the difficulties related to the fragments short range in target fragmentation ( $\sim \mu\text{m}$ ), the FOOT experiments adopts an inverse kinematic approach. Data of the cross section of H can be extracted by subtraction from the coupled data obtained using both  $\text{C}_2\text{H}_4$  and pure C target.

The software of FOOT plays a fundamental role in the experiment and has been named SHOE, *Software for Hadrontherapy Optimization Experiment*; it is composed of two main units, the simulation framework and the reconstruction one. The FOOT simulation has been built in the framework of the FLUKA code. FLUKA is an advanced Monte Carlo simulation tool for the calculation of particle transport and interactions with matter. During the planning phase it has been used for the optimization of the experimental setup by examining the MC simulations of different detector configurations. The reconstruction tool performs the reconstruction on the real data, followed by charged track identification which is the basis for the cross section measurement. The reconstruction is performed by a ROOT based framework, the GENFIT tracking tool, which implements a variety of track fitting algorithms, among which, an extended Kalman filter, a Kalman filter with reference track and one Deterministic Annealing Filter (DAF). At present, the specific implementation in FOOT experiment uses the extended Kalman filter algorithm; different studies are ongoing on the possible use of the DAF, which should be more powerful and appropriate in the presence of multiple background hits. The aim of this thesis is to present a preliminary study aimed to check the stability and feasibility of including a more efficient Kalman Filter algorithm than the one currently implemented in the FOOT reconstruction code.

This thesis is organized as follows. In Chapter 1 there is a quite detailed description of the physics and radiobiology of the interaction of radiation with biological matter. In Chapter 2 the motivations to study physical applications both in the biomedical and radio-protection fields are discussed. In Chapter 3, the motivations of FOOT experiment are outlined, summarizing also the detector design, its performance study and depicting the collaboration work which inspired its project. In Chapter 4, the study of various possible methods for the optimization of track reconstruction is presented, focussing on the Kalman filter application. The performances of the Kalman tracking algorithm of the FOOT experiment are presented and explained inside the framework of the SHOE software. Lastly, in Chapter 5, I present my work of thesis, a preliminary study aimed to check the stability and feasibility of including a more efficient Kalman Filter algorithm than the one currently implemented in the FOOT reconstruction code.

# Chapter 1

## Interaction of Radiation with Matter

The interaction of radiation with matter is one of the most studied subjects in modern physics. In the last decades, both the progress in technology and the improvement in knowledge of the physics of fundamental interactions have allowed numerous application in a variety of different disciplines and the development of related new techniques. One of the most interesting application of radiation studies lies in the biological field and in particular in the tumor treatment, on which the following chapters are focussed.

The propagation of radiation in a medium and its interaction with organic matter varies depending on the radiation type, energy and target material, according to the laws of quantum mechanics. The first distinction can be made between neutral and charged radiations. Neutral radiation mainly includes photons (the energy range of medical interest is between 100 keV and 10 MeV), while charged radiation has to be further distinguished in light and heavy charged radiation, such as electrons and positrons as opposed to protons, alpha particles and other ions.

### 1.1 Photons

The behavior of photons interacting with matter is different from that of charged particles. The principal mechanisms of interactions are (Fig. 1.2):

- photoelectric effect;
- Compton scattering;
- pair production;

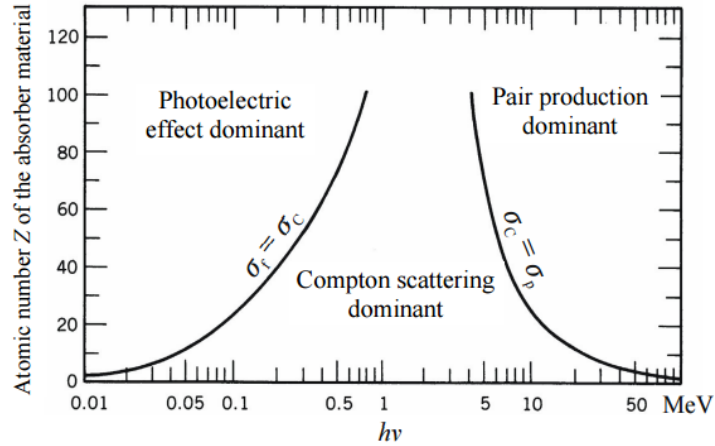


Figure 1.1: The graphic shows the relative importance of the photoelectric absorption, Compton scattering and pair production in different absorbing media ( $Z$ ) and energies.

The three kinds of interaction have different predominance according to the energy range. The graphic (1.1) shows their relative importance in distinct media and at different energies.

All these processes can lead to a partial or complete photon energy transfer to atomic electrons or nuclei. As a consequence, a photon that interacts with the target is completely removed from the incident beam. In this way, a beam of photons crossing a medium is not degraded in energy (with the exception of Compton scattering) but only attenuated in intensity, according to the exponential law,

$$I = I_0 \exp[-(\mu/\rho)x] \quad (1.1)$$

for a narrow beam of mono energetic photons with an incident intensity  $I_0$  that penetrates a material of thickness  $x$  and density  $\rho$ . The quantity  $\mu$  is the probability per unit length for an interaction, called *total absorption coefficient* obtained multiplying  $\sigma_{tot}$  by the atom density  $N$ , hence given by

$$\mu = N\sigma_{tot} = \sigma_{tot}\rho\frac{N_A}{A} \quad (1.2)$$

where  $N_A$  is Avogadro's number ( $6.022045 \times 10^{23} \text{mol}^{-1}$ ) and  $A$  is the relative atomic mass of the material. The total probability for a photon to interact with matter can be expressed as the sum over contributions from the principal cross sections, each of which will be explained in the next paragraphs.

$$\sigma_{tot} = \sigma_{pe} + \sigma_C + \sigma_{pp} \quad (1.3)$$

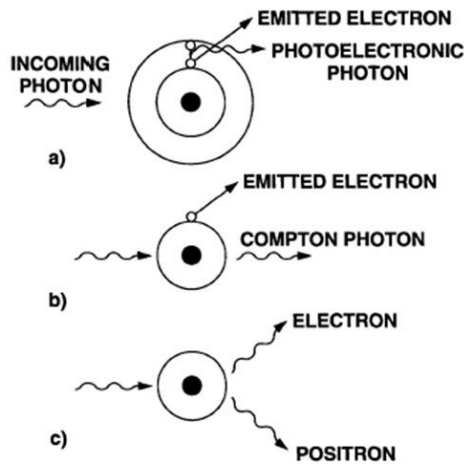


Figure 1.2: Different types of interaction between photons and atoms: (a) photoelectric absorption, (b) Compton scattering, (c) pair production.

### 1.1.1 Photoelectric Effect

The photoelectric effect is a two-step event in which an atomic electron from an inner shell is ejected after receiving all the energy of an incident photon. When a core electron is removed, leaving a vacancy, an electron from a higher energy level may fall into the vacancy, resulting in a release of energy. Although most often this energy is released in the form of an emitted photon (X-ray), the energy can also be transferred to another electron, which is ejected from the atom; this second ejected electron is called an Auger electron.

The most tightly bound electrons give the most important contribution to the atomic photoelectric cross section; these electrons belong to shell K, the innermost shell, closest to the nucleus. Cross section depends from the atomic number  $Z$  and the energy of the photon ( $\sigma_{pe} \propto Z^y/E^{7/2}$  with  $y$  varying between 4 and 5).

### 1.1.2 Compton Scattering

In Compton scattering, a photon collides with a weakly bound electron, called recoil electron, transferring to it part of its energy. After the interaction, the photon is deflected from its original direction and the electron is expelled leaving the ionized atom ( $\sigma_C \propto Z/E$ ).

The energy of light quanta depends only on the frequency of the light. Assuming that each scattered X-ray photon interacts only with one electron, the mathematical relationship between the shift in wavelength and the scattering angle of the X-rays is

$$\lambda_f - \lambda_i = \Delta\lambda = \frac{h}{m_e c} (1 - \cos \theta) \quad (1.4)$$

where  $\lambda_i$  is the initial wavelength,  $\lambda_f$  is the wavelength after scattering,  $h$  is the Planck constant,  $m_e$  is the electron rest mass,  $c$  is the speed of light, and  $\theta$  is the scattering angle.

The Compton effect may occur when photon energies range from approximately 50 keV to 3 MeV, becoming more dominant at energies above 100-150 keV (see Figure 1.1).

### 1.1.3 Electron Pair Production

At higher energies, the most frequent interaction occurring between photons and matter is the electron pair production. A photon having an energy of at least 1.022 MeV (value of the mass at rest of two electrons) can convert into an electron-positron couple. All the exceeding energy carried by the photon goes into kinetic energy shared by the electron and the positron. The positron may subsequently annihilate with another electron of the medium, producing two annihilation photons as secondary products of the interaction, while the electron can emit a high-energy photon by interacting with the nuclear electronic field (Bremsstrahlung effect, see Ch. 1.2). This will lead to the production of an electronic shower that may propagate as long as the energy of photons and electrons decreases below the process threshold.

The cross section related to this process is  $\sigma_{pp} \propto Z^2 \ln E$  for low energies and  $\sigma_{pp} \propto Z^2$  for high energies.

## 1.2 Electrons and Positrons

Differently from photons, electrons are charged particles, therefore they lose energy interacting with matter in a different way, following two principal mechanisms. At low energy, electrons and positrons lose energy by Coulomb collision when passing through matter; at high energies they dissipate energy by emitting electromagnetic radiation, a process called *Bremsstrahlung* ("braking radiation") caused by the deflection of the particle passing through the Coulomb field of the nucleus. The energy loss during the bremsstrahlung process is more relevant for low mass particles, being the cross section  $\sigma \propto (e^2/mc^2)^2$  inversely proportional to the mass of the incident particle.

The total energy loss of positrons and electrons can be expressed by the sum of two terms:

$$-\left(\frac{dE}{dx}\right)_{tot} = -\left(\frac{dE}{dx}\right)_{rad} - \left(\frac{dE}{dx}\right)_{coll} \quad (1.5)$$

## 1.3 Heavy Charged Particles

A heavy charged particle passing through a material, can either collide with the atomic electrons or the nuclei of the atoms. Between these two electromagnetic processes, the inelastic collision with the atomic electrons is the dominating contribute to the loss of energy. In fact, two particles interact via Coulomb force as the heavy charged particle passes nearby. The valence electron can take up an appreciable amount of energy from the incident particle, rising up to a higher shell or, if the energy is enough, undergo ionization. No significant deflection of the primary particle trajectory will be observed, as the electron mass is much smaller than the heavy charged particle mass. Despite the particle energy loss being limited in every single electron-nucleus interaction, thanks to the great number of collisions per unit length, the total energy loss through the medium is significantly appreciable, even in a thin layer of material[1].

On the other hand the elastic interaction with the atomic nuclei produce a smaller energy loss, due to the lower frequency of the interaction. This is true even if the scattering center (the atomic nucleus) is more massive than the electron.

Because of their greater charge, massive nuclei scatter the incident particle, causing particle deflections that are anyhow confined to small angles. Hence the energy loss by heavy charged particles occurs almost entirely in collisions with electrons.

Another important process responsible for the particle energy loss is the nuclear fragmentation, the details of which will be described further on.

### 1.3.1 The Bethe-Block Formula and Stopping Power

As mentioned before, the number of inelastic collisions between charged particles and atomic electrons per unit path length is usually large, so interactions have a statistical interpretation with a given quantummechanical probability. Anyway, since fluctuations in the total energy loss are small, it is possible to consider the average energy loss per unit path length, the so called *stopping power*  $dE/dx$ . This quantity was first calculated by Niels Bohr in 1915 using classical mechanics equations and was later corrected by Bethe, Bloch and others [2] who took into account a complete quantum mechanical dissertation of the energy loss.

During collision, if the particle velocity is greater than the electron orbital velocity, the bound atomic electron can be treated as a free particle and initially at rest. The momentum transfer can be assumed to be sufficiently small, so the particle trajectory is essentially not deflected and the recoiling electron does not move during the interaction. Then, assuming also that the particles magnetic interaction is negligible, since the electron is basically at rest, we obtain the *Bethe-Bloch equation*

$$-\left(\frac{dE}{dx}\right) = 2\pi \frac{N_A Z \rho}{A} \frac{m_e r_e^2 c^2 z^2}{\beta^2} \left[ \ln \left( \frac{2m\gamma^2 v^2 W_{max}}{I^2} \right) - 2\beta^2 - \delta(\beta\gamma) - 2\frac{C}{Z} \right] \quad (1.6)$$

The constants and values used in the equation (1.6) above are summarized in table 1.1 below.

---

$N_A$	Avogadro's number	$6.022 \times 10^{23} \text{mol}^{-1}$
$Z$	target atomic number	
$A$	target atomic mass	
$\rho$	Target density	
$r_e$	classical electron radius	$2.817 \times 10^{-13} \text{ cm}$
$m_e$	electron mass	0.510998 MeV
$c$	light speed	
$z$	unitary charge of the projectile	
$\beta$	$v/c$ of the projectile	
$\gamma$	Lorentz factor	
$W_{max}$	maximum energy transfer in a single collision	
$\delta$	density correction	
$C$	shell correction	

---

Table 1.1: Variables used in the *Bethe-Bloch equation* (1.6)

The corrections  $\delta$  and  $C$  become significant respectively at high and low energy. The *density correction*  $\delta$  takes into account the fact that the incident particle has an electric field that tends to polarize the atoms along its path inside the target, shielding the electrons far from the particle trajectory and giving a negative contribution to the energy loss.

The *shell correction*  $C$  arises instead when the velocity of the particle is comparable to or even smaller than the orbital velocity of the atomic electrons. In these cases, the hypothesis that the electron is stationary with respect to the incident particle, by which assumption the equation (1.6) was obtained, is no longer valid.

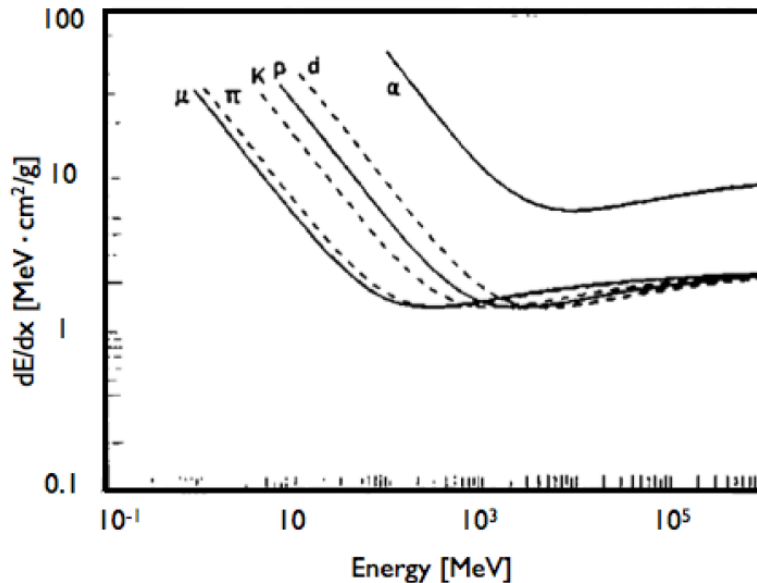


Figure 1.3: The stopping power as a function of the kinetic energy for different particles [1].

In Figure (1.3) the stopping power as a function of the particle energy is represented; it shows that a charged particle crossing a medium loses most of its energy at low velocity. As the kinetic energy increases, the stopping power decreases like  $1/\beta^2$  until it reaches a minimum at  $v \sim 0.96c$ , at which point particles are usually referred to as *Minimum Ionizing Particles* (MIP). At the MIP point all charged particles have similar stopping power. After this point, the  $1/\beta^2$  factor remains almost constant and the stopping power rises again due to the contribution of the logarithmic part of the Bethe-Block.

When a heavy charged particle enters into a medium with a given velocity and a given kinetic energy, it starts to lose energy. If it enters at velocities above the MIP point the deposited energy per unit path length is approximately constant for all particles. When it reaches velocities below the MIP point, the stopping power increases with time reducing the velocity at a greater rate, increasing in turn the deposited energy. Hence it deposits more energy per unit path length at the end of its path inside the target, rather than at its beginning; this behaviour is shown in Figure 1.4 and the characteristic function is named *Bragg curve*.

### 1.3.2 Penetration Range

The range of a particle is its penetration depth through a medium until it loses all of its kinetic energy. For a heavy charged particle the energy loss is continuous, due to interactions with both atomic electrons and nuclei.

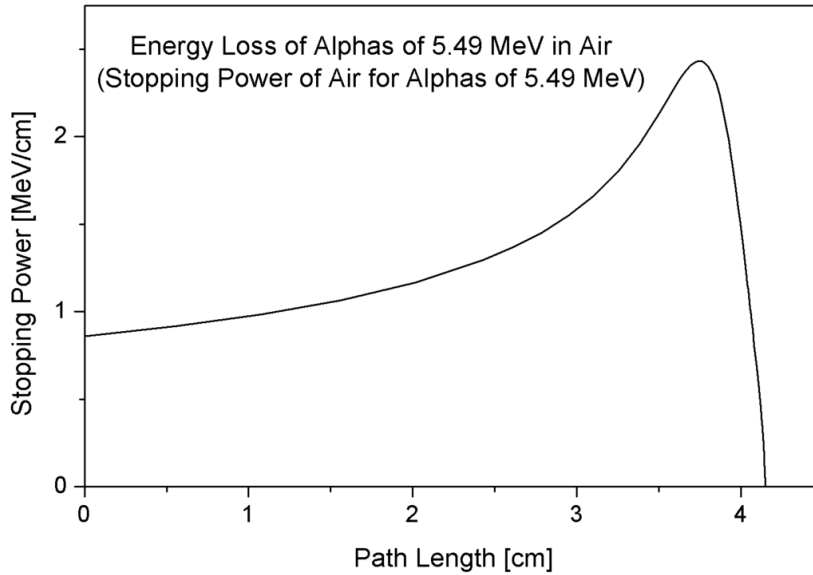


Figure 1.4: A typical Bragg curve, showing the stopping power as a function of the target depth.

The penetration range of a particle depends on its mass and charge, on its initial energy and on the crossed material. Due to the large number of collisions the energy loss is a stochastic process which can be approximated with a Gaussian expression. The statistical fluctuation of the energy loss results in a broadening of the *Bragg peak* as shown in Figure (1.5). Therefore, the range is subject to fluctuations: two identical particles will not undergo the same number of collisions; this phenomenon is called *straggling* [3].

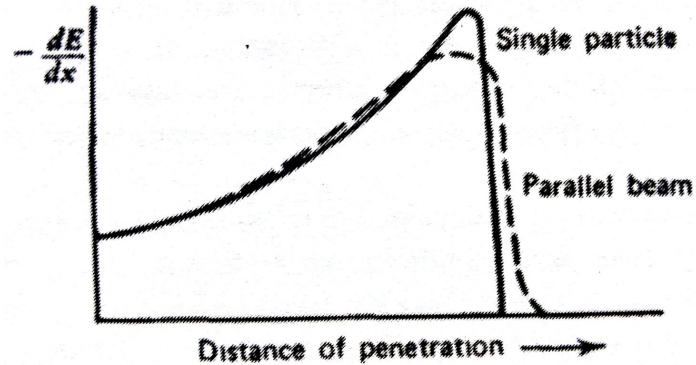


Figure 1.5: Example of Bragg curve vs penetration depth for  $\alpha$  particle of 7 MeV. The two curves differ due to the effects of straggling.

### 1.3.3 Nuclear Fragmentation

There are two main physical effects that contribute to the lateral spread of the ion beams: the electromagnetic interactions and the nuclear interactions. The electromagnetic ones are the main processes occurring as a charged particle enters into a target. However, even if the nuclear interactions have a small probability of occurring, they must be taken into account as they can lead to significant consequences. In particular the nuclear fragmentation must be considered when heavy charged particles have a kinetic energy of 100 MeV/u or more.

There are two types of nuclear interaction: elastic and inelastic. If the incident particle undergoes elastic collision, the kinetic energy is conserved, leading to an average small angular deviation of the projectile. However, the most relevant effects happen during inelastic collisions, as they do not conserve the kinetic energy and may result in the fragmentation of the projectile and/or of the target nuclei.

The nuclear collisions between the particle projectile and the target nuclei can be distinguished in central and peripheral by experimental observation.

- The central head-on collisions are characterized by an almost complete destruction of both the projectile and target nucleus, leading to a multiplicity of high mass fragments and secondary products, such as low mass charged particles, electrons or  $\gamma$ -rays. However, for geometrical reasons, this kind of events is statistically less frequent.
- The most frequent nuclear collisions are the peripheral ones, characterized instead by a relatively small momentum and energy transfer, since only part of the nucleons effectively interact. They can however produce nuclear fragmentation.

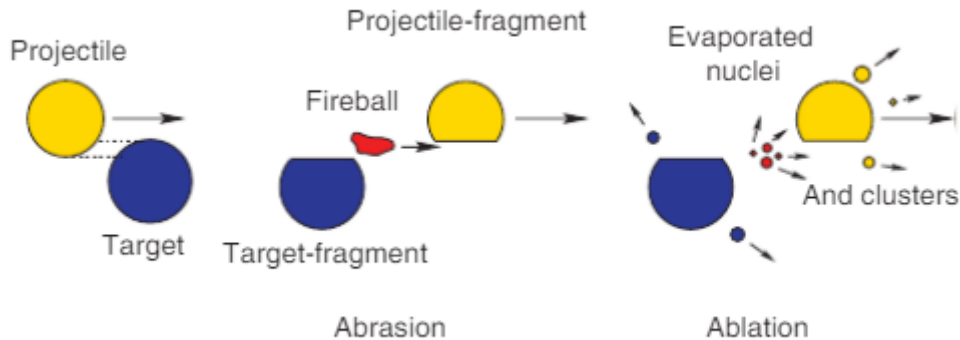


Figure 1.6: Illustration of the abrasion-ablation process.

The *abrasion-ablation* model [4] (Figure 1.6) is a simplification of the interactions between nuclei, from which the majority of Monte Carlo simulation codes are derived [5]. In this phenomenological model the fragmentation process is divided in two stages with different time scales. In the first one, the nuclei interact with each other in the overlapping zone, resulting in the "abrasion" of parts of the projectile and target nucleus. Therefore a cluster of excited fragments (fireball) are produced in the flying direction of the projectile, while the outer nucleons (spectators) are only slightly affected by the collision. The *abrasion* process has a time scale characteristic of the strong interaction,  $\sim 10^{-23}$ s. In the second step, the *ablation*, all the fragments de-excite by evaporation of neutrons, protons and light nuclei, fission and gamma rays emission. The characteristic time for particles emission varies in a range between  $10^{-16}$ s to  $10^{-21}$ s for an excitation energy of the fragments of 10 MeV and 200 MeV, respectively [6].

The major effects of the nuclear interactions of heavy ions are given by the fragmentation of the incident particles; projectile fragments are mostly produced in the forward direction close to the primary track. They have lower mass than the initial nucleus, which leads to a longer range.

Differently from heavy ions, protons cannot break up at low energies, so the nuclear interactions result in the fragmentation of the target only.

## 1.4 Radiobiology: Physical and Biological Aspects

Radiobiology is a branch of science which evaluates radiation effects on a living organism and studies its consequences. In fact, when a radiation crosses an organic tissue the principal effect is the damage to the cell molecules due to ionization. An ejected electron can cause further ionisations as it collides with other molecules in its path. Ionised molecules undergo a rapid cascade of chemical interactions, which may break the chemical

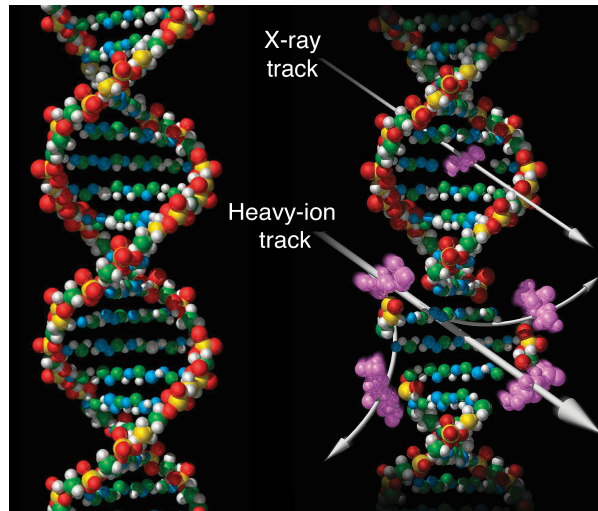


Figure 1.7: Schematic image of the DNA damages (violet) caused by X-rays and heavy ions.

bonds, leading to major functional and/or structural damage to vital macromolecules such as deoxyribonucleic acid, DNA. On the other hand, when incident radiation is constituted of heavy particles (hadrons) the damage can be both direct and due to secondary ionization.

### 1.4.1 Radiation Effect on Cells

After the discovery of DNA and the genetic code in 1953, it became clear that the most susceptible target of radiation was the DNA inside cellular nuclei. Breakage of chemical bonds doesn't usually cause the death of the cell directly, as most molecules undergo either a continuous rapid turnover or a repair process in order to fix the damaged bonds.

Every fundamental information for the cell is inscribed in the chromosomes, complex combinations of DNA molecules and proteins. They are located inside the cellular nucleus and are approximately  $20\mu\text{m}$  long. The characteristic diameter of the DNA double helix is  $2 - 3$  nm. The criticality of DNA damage is largely due to the fact that if the DNA in the chromosome of a cell is damaged, so are the instructions that control the cell function and replication.

Radiations can cause damage in two different ways: directly or indirectly. If the DNA is directly ionised by the incoming radiation the damage is taken by the double helix; about the 80% of the total damage is caused by strand break. While SSB (Single Strand Breaks) can be restored by the efficient repair system of the cell, DSB (Double Strand Breaks), which are more likely to happen in the heavy ion beam interactions with matter, cause permanent damage to the DNA. The ionization electrons produced in the heavy

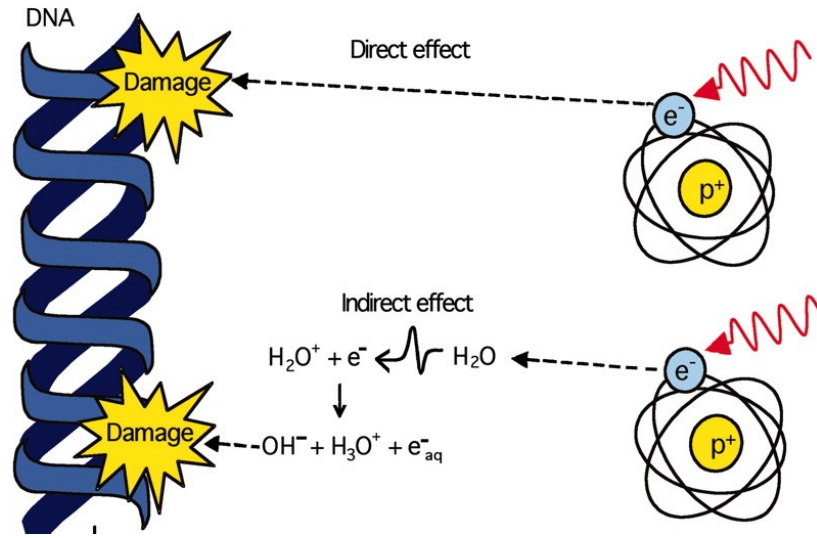


Figure 1.8: Direct and indirect radiation induced damage to the DNA

ion beam interactions with matter have a mean free path of the order of few nanometers, providing a high probability for double ionizations on the DNA opposite strands, whose separation is of about 2 nm (Figure 1.7). The so called Double Strand Break is more difficult to repair by the cell itself, resulting in a higher damage capability for heavy ions with respect to photons.

The indirect effect of radiation on molecules is given by the formation of *free radicals*, highly reactive molecules with a free orbital electron. These free radicals interact with nearby molecules causing spread damage that can reach the DNA. Over 70% of the human body is made of water, thus the development of free radicals from water is highly probable. Electrons breaking the chemical bonds of water thus produce free radicals, leaving molecules with an odd unpaired electron.



### 1.4.2 Absorbed Dose

One of the most important physical quantities in radiobiology is the dose deposited in a tissue. It is defined in the equation below as the mean energy deposited by ionizing radiation (E) per mass unit (m) [7].

$$D = \frac{dE}{dm} \quad (1.8)$$

In the International System of Unit (SI) the dose unit of measurement is the *gray*

and 1 Gy corresponds to 1 J of radiation energy deposited in 1 kg of mass (1 Gy = 1 J/kg).

The depth-dose profile is strictly related to the stopping power (definition in section 1.3.1), but in case of organic tissues, it is not directly linked to the effective biological damage.

### 1.4.3 Linear Energy Transfer

The *Linear Energy Transfer* (LET) is the energy deposition by a ionizing radiation along its path in a tissue. The unit of measurement for the LET is the keV/ $\mu\text{m}$ . The definition of LET is very similar to the one of the stopping power, given in section (1.3.1), however while the latter is the energy loss of the incident particle, LET is considered as the energy transferred to the absorber.

The LET is furthermore only related to the energy loss of the primary charged particle due to electronic collisions. The higher is the LET value, the higher is the energy transferred by the radiation in a small path. The LET is hence directly coupled to the DNA damages, so biological effects strictly depend on it.

Heavy charged particles have high LET and produce clustered lesions because of their higher energy deposition density along their track. Photons are considered as low LET radiations due to their sparse ionisation, leading to a minor biological effect.

Radiation	Energy	LET (keV/ $\mu\text{m}$ )
X-ray	250 keV	3
X-ray	3 MeV	0.3
$\gamma$ s from Cobalt 60	1.33 MeV	0.3
Beta	10 keV	2.3
Beta	1 MeV	0.25
Neutrons	2.5 MeV	20
Neutrons	19 MeV	7
Protons	2 MeV	16
Helium	5 MeV	100

Table 1.2: Typical LET values of different radiations

### 1.4.4 Relative Biological Effectiveness

The linear energy transfer is not sufficient to fully describe the biological effects of radiations, indeed different radiations have different local dose densities, depending also on the target cells or tissue type. The RBE (Relative Biological Effectiveness) is defined in the equation below as the ratio of a reference absorbed dose of a standard radiation

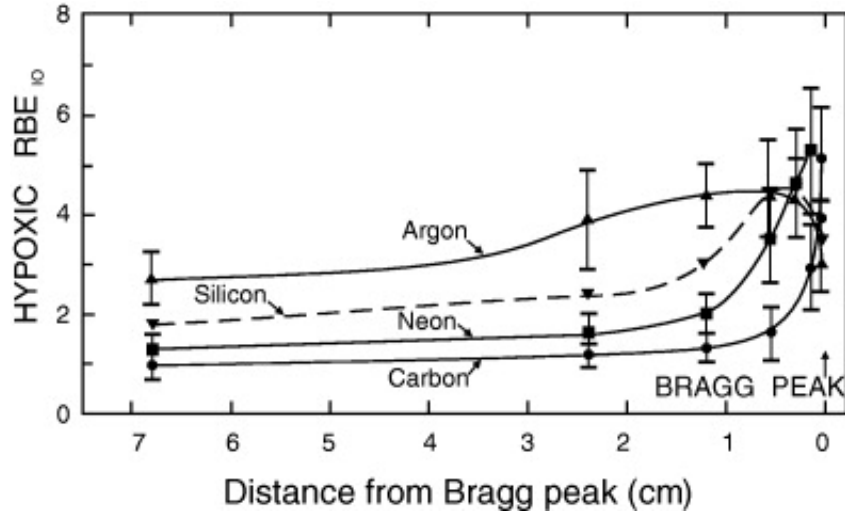


Figure 1.9: RBE for various ions as a function of the penetration depth inside a hypoxic tissue.

( $D_{ref}$ ), typically monochromatic  $\gamma$  rays from  $^{60}\text{Co}$  to the absorbed dose of the radiation under study ( $D_{test}$ ) that produces the same biological effect (isoeffect):

$$RBE = \frac{D_{ref}}{D_{test}} \quad (1.9)$$

Consequently the RBE is a very powerful tool which describes the radiation capability of inducing cellular death. As previously assessed, the RBE of a given type of radiation varies with the radiation parameters and the radiosensitivity of the biological tissue. RBE does also depend from LET, increasing up to a maximum value and then decreasing for higher LET values regardless of the particle type (Figure 1.10).

As shown in Figure (1.9), carbon ions are more effective than photons in killing human cells, having  $RBE > 1$  close to the Bragg peak and  $RBE \sim 1$  in the entrance region; this is one of the reasons why at the beginning of 1990s carbon ions were chosen as the most suitable particles for hadrontherapy. Further and more complete considerations on this topic will be given in the next chapter.

### 1.4.5 Oxygen Enhancement Ratio

The presence of oxygen in a cellular tissue is able to maximize the secondary damage of radiations by creation of free radicals; thus a very important parameter to estimate the biological effect of radiation interaction with organic matter is the *Oxygen Enhancement Ratio* (OER). OER is defined as the ratio of a dose for hypoxic (oxygen deficient) tissue

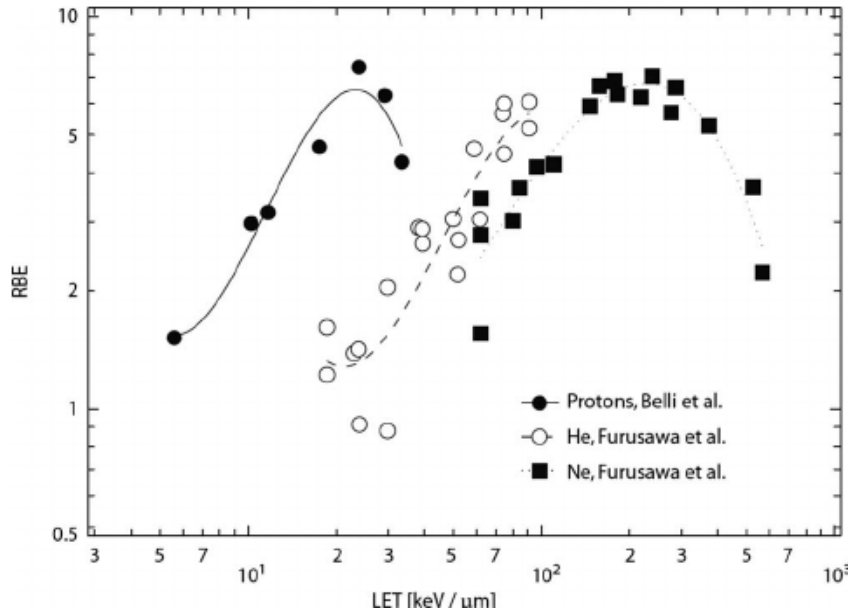


Figure 1.10: Dependence of  $RBE_{\alpha}$  on LET and particle type [8].

and a biologically iso-effective dose for well oxygenated tissue,

$$OER = \frac{D_{hypox}}{D} \quad (1.10)$$

Typical values of OER variate between 1 to 3 (1 for damage independent from oxygen presence - 3 for damage highly dependent from oxygen presence). Radiations with high LET, for instance charged heavy ions, usually have a lower OER, which means that they don't resent of the presence of oxygen. This is a consequence of the fact that radiation damage is caused by direct ion collisions, less sensitive to the presence of oxygen compared to indirect hits induced by free-radicals, typical of X-rays.

# Chapter 2

## Applications in Modern Science

Scientific progress has historically brought improvement in society helping to solve problems in a variety of different fields. For what particle and nuclear interactions physics is concerned, research has brought improvement both in the biomedical field and in radiation protection methods.

### 2.1 Cancer Treatment

Cancer is one of the major widespread health problems and a leading cause of death worldwide, accounting for 8.8 million deaths in 2015, according to World Health Organization (WHO) [9]. Cancer is a disease that involves a relentless cellular evolution and growth from a neoplastic clone, a cell which shows a functionality variation that brings to an abnormal differentiation. The loss of functionality brings an uncontrolled insurgence of new mutations in the cells; the neoplastic cells invade the healthy tissues locally and can create metastasis, an extent from the primary site of development to a secondary site within the human body.

Nowadays there are different techniques to treat neoplastic diseases. When possible, surgery is a standard treatment approach to remove or reduce the solid tumor. Other standard methods for the reduction of fast replicating cells as support treatment to surgical removal are chemotherapy, immunotherapy and radiation therapy. Radiation therapy can be used alone as therapeutic treatment or in combination with surgery, both before and after, as adjuvant therapy; statistically it contributes to the cure of approximately 23% of all cancer patients [10].

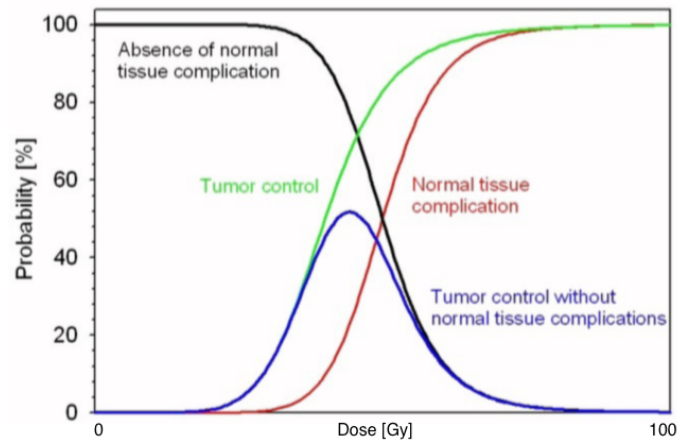


Figure 2.1: The dose-response curve for Tumor Control Probability TCP and NTCP, Normal Tissue Complications Probability

The fundamental tasks of oncological radiation therapy is to kill the cancer cells minimizing the healthy tissues complications, preventing the spreading of the primary mass and the formation of secondary tumors. Generally, cells either are able to repair DNA strand damage or alternatively they die or kill themselves through a process known as apoptosis. Tumor cells, being mutated units, have inhibited instructions that control cell growth and apoptosis. Moreover, they undergo continuous reproduction causing the mutation to be spread on through cell division.

As explained in the previous chapter (see Section 1.4.1), radiation therapy works by taking advantage of the damaging effect of radiation on biological tissues, killing the cancerous cells by wrecking their DNA molecular bonds. Radiation therapy can adopt two kinds of radiation: high energy photons (or electrons) or charged particles. The two types of treatments and the difference between hadrons and photons in releasing energy in tissues will be fully described and compared in the sections below.

### 2.1.1 Radiotherapy

Since the discovery of X rays by Wilhelm Röntgen, they were actively used for tumor treatments; at present day, radiotherapy is widely spread all over the world and plays a central role both in curative and palliative purpose. Radiotherapy is an effective treatment that can nevertheless damage healthy tissues and bring risk of insurgence of secondary tumors, frequently fatal for pediatric patients.

In the last decades many studies have been made to improve the deposition of radiation energy and to preserve the patient's healthy tissues. The energy of the incident photons may be increased to reach deeper tissues and X rays can be substituted with the more energetic  $\gamma$  rays. The development of new technologies and the discovery of imaging

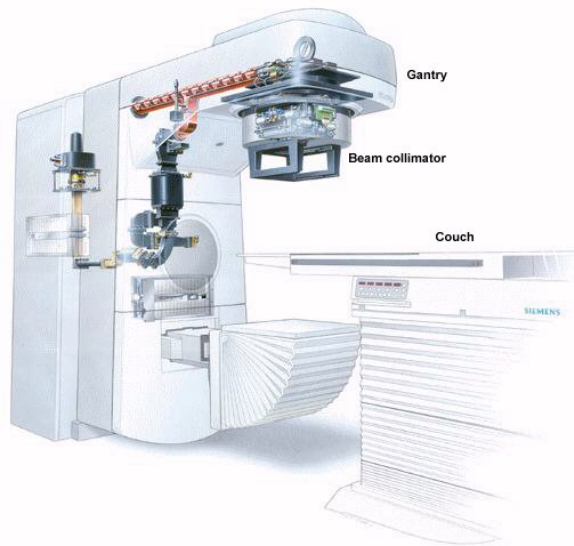


Figure 2.2: Main components of a medical linac.

techniques have brought to the use of compact linear accelerators (LINAC) that supply beams of high energy photons (4 - 25 MeV), and advanced radiotherapeutic treatments like IMRT (*Intensity Modulated Radiation Therapy*).

The linear accelerator is a device that uses high-frequency electromagnetic waves to accelerate charged particles such as electrons to high energies through a linear tube. The high-energy electron beam itself can be used for treating superficial tumors, or it can be made to strike a target to produce X rays for treating deep seated tumors. The main mechanism for X-ray production in medical linac is the Bremsstrahlung process (Section 1.2). The energetic electrons that have been accelerated are shot at a target (typically tungsten) and then are slowed down very quickly. This deceleration (or breaking) of the electrons generate electromagnetic radiation and for relativistic electrons this will produce X rays. Medical linacs are installed on a rotating structure, called *gantry*, which allows to select the best beam direction for treatment planning (2.2).

In 1950 the first electron linac was built for research purposes at the Stanford University by W. Hansen and his collaborators. Today there are almost 10,000 linacs installed and operational in hospitals all over the world and more than about 20,000 patients tumor affected per year are treated with radiation therapy [11]. This huge expansion in the use of radiotherapy has been possible also thanks to the progress on computation and imaging techniques, such as Computed Tomography (CT), Magnetic Resonance Imaging (MRI) and Positron Emission Tomography (PET) scans.

In this section, some general aspects and parameters that characterize radiation therapy and its current applications are outlined.

**Dose** The amount of radiation used in photon radiation therapy varies depending on the type and stage of cancer being treated. For curative cases, the typical dose for a solid epithelial tumor ranges from 60 to 80 gray. The standard energy of photon beams used goes from 6 to 25 MeV.

The dose release profile follows a decreasing exponential law, according to the theory explained in section 1.1. The characteristic profile (see Figure 2.3) shows a maximum dose release at few centimetres from the entering surface, then an exponential decrease which becomes less steep with increasing depth. The main problem of radiotherapy is the presence of a dose peak at short distance from the patient's derma, while tumors are frequently found in deeper tissues. This means that the maximum dose release does not coincide with the cancer position, therefore implying an increased risk for healthy tissues in front and behind the cancerous volume, with consequent threat for organs at risk (such as prostate, brain, optic nerves, etc.).

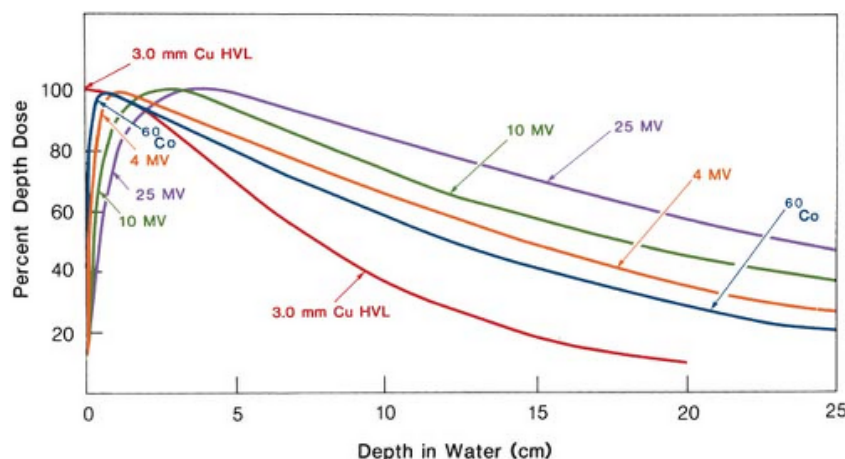


Figure 2.3: Central axis depth dose distribution for different-quality photon beams.

**Biological parameters** Photons are low LET radiations; being biological effects directly linked to LET, this means that photons are low ionizing radiations. The eventual damages induced in the DNA are stochastic and randomly distributed in the target volume. In figure (2.4) it is shown how human epithelial cells are damaged by different types of radiation: the DSBs in DNA caused by  $\gamma$  rays are equally distributed in the whole volume, while those caused by heavy particles like silicon and iron show a well defined linear pattern.

In photon therapy, the DNA damage is mostly induced by free radicals formed by indirect atom ionizations, as explained in Section 1.4.1. Moreover, one of the major limitations of this radiation technique is that solid tumor cells become deficient in oxygen, as their rapid growth in mass is not balanced by an equally fast vascularization of the new tissues. Cancer cells in a hypoxic environment may be 2 to 3 times more resistant

to radiation damage than those in a normal oxygen environment, as the formation of free radicals is strongly opposed (see OER in Section 1.4.5).

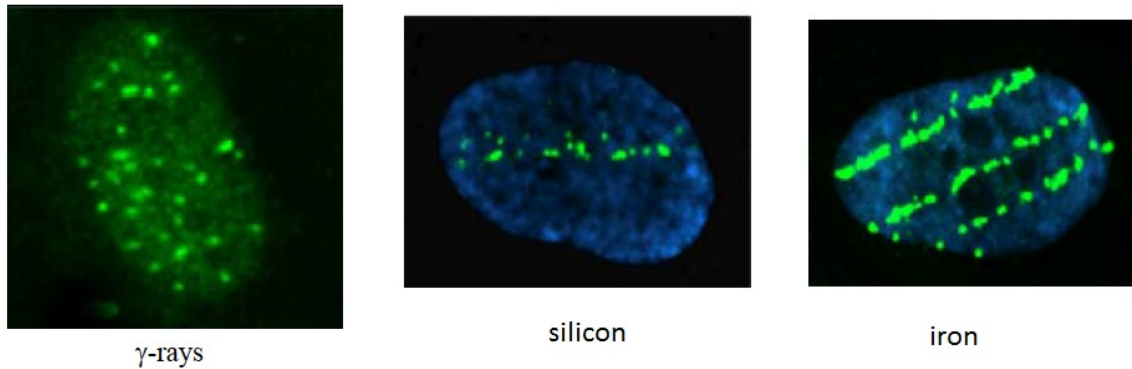


Figure 2.4: DNA double strand break by immunofluorescence in human skin fibroblast exposed to 2 Gy of ionizing radiation [12].

**IMRT** The Intensity Modulated Radiation Therapy is, at present, a pioneering technology in traditional radiotherapy. It uses multiple (from 6 up to 9) radiation beams of non-uniform intensities coming from different directions, thanks to rotating gantries.

The treatment is carefully planned by using 3-D computed tomography (CT) imaging or magnetic resonance (MRI) to determine the dose intensity pattern that will best conform to the tumor shape while minimizing the dose to adjacent normal tissues and organs at risk. With respect to the 3-D conformal radiation therapy, IMRT is a more advanced technique and allows the radiation dose to conform more precisely to the tumor, granting the release of a higher dose to the target volume with a minimum release in healthy cells (see comparison in Figure 2.5).

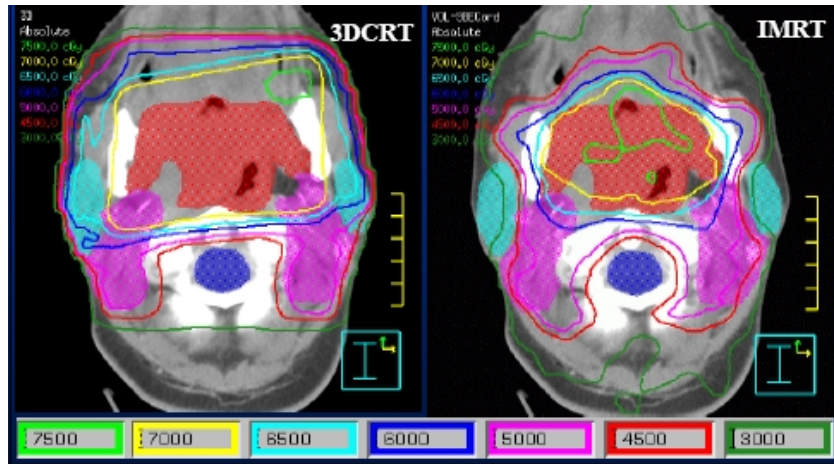


Figure 2.5: Comparing dose distribution for 3-dimensional conformal radiation therapy (3DCRT) and IMRT. IMRT allows for the radiation dose to conform more precisely to the shape of the tumor by modulating the intensity of the radiation beam in multiple small volumes.

### 2.1.2 Hadrontherapy

From the second half of the 19th century proton and heavy ion beams therapy (Particle Therapy) has developed and spread all over the world. Also named Hadrontherapy (greek  $\alpha\delta\rho\acute{o}\varsigma$ , *hadrós*, "stout, thick"), this technique uses beams of hadrons, particles compounded by quarks held together by the strong interaction.

The first attempts to use high energy beams of charged particles for medical application were made in 1946 by Robert R. Wilson, who proposed to use accelerated protons for localized cancer therapy [13]. Years later the physical and radiobiological properties of proton beams were thoroughly investigated by Cornelius A. Tobias, who continued the work started by Wilson at Lawrence Berkeley Laboratory. The results showed that hadrons were ideal candidates for tumor therapy [14], and in 1954 the first proton treatment was performed.

Different charged particles like He, Ar, Si, Ne were tested to improve the effectiveness of ion beam therapy; only in the early 90s carbon ions were recognized as the optimal choice.

The fundamental characteristic of hadrontherapy lies in its specific dose release profile which outlines a low dose at the beginning of the path, a maximum release in the Bragg peak at the end of its path (see Section 1.3.2) and almost no dose beyond the peak. Nowadays charged particles are used to treat deep sited tumors, due to the high localization of their dose release which reflects on a high efficiency in killing cancer cells, sparing healthy tissues and organs at risk surrounding the tumor volume.

In this section, some general aspects and parameters that characterize particle ther-

apy are summarized. Furthermore, the current status will be underlined in order to give a deeper view of the issues and of the future prospects and challenges for hadrontherapy treatment improvement.

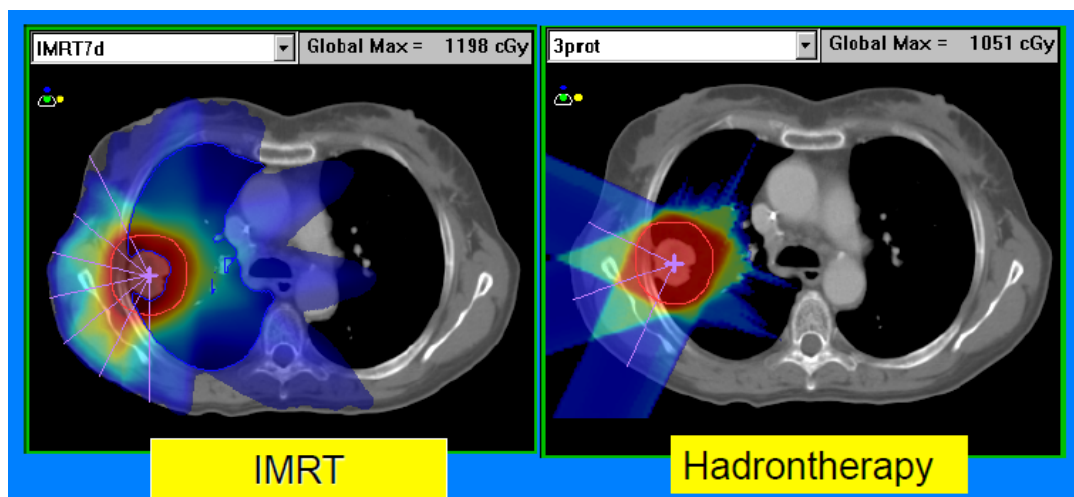


Figure 2.6: Treatment plans comparison for a target volume sited in a lung irradiated with 3 fields with protons (right) and 7 fields with IMRT (left). A comparable dose conformation over the tumor volume can be achieved with both techniques, but the use of protons would reduce dramatically the integral dose to the surrounding healthy tissues, sparing OAR in proximities.

**Facilities** In 1990 the first hospital-based proton centre was built at the Loma Linda University in California; in 1994 the Heavy Ion Medical Accelerator (HIMAC) started treatments with carbon ions at the National Institute of Radiological Science (NIRS) in Chiba, Japan. At the same time new technical solutions were developed at the Gesellschaft für SchwerIonenforschung (GSI) in Darmstadt, Germany, where the Heidelberg Ion Therapy center (HIT) was subsequently built. In Catania, CATANA the first hadrontherapy center in Italy at Laboratori Nazionali del Sud (LNS) is functional since 2002 and it deals with choroidal and iris melanomas. The first hospital centre in Italy and fourth in importance after USA, Germany and Japan, is the Centro Nazionale di Adroterapia Oncologica (CNAO) in Pavia [15], which treated its first patient with protons in 2011. Together with the HIT centre in Heidelberg, CNAO is the only facility in Europe that allows both for protons and carbon ions therapy.

At present time, there are about 70 clinical facilities operating with photons or heavy ions worldwide, and more under construction even in new countries [16].

In November 2016, the Particle Therapy Co-Operative Group (PTCOG), an international institution that monitors the hadrontherapy facilities all around the world, published a statistic [17] of Particle Therapy patients (2015) which counts that 154,203

COUNTRY	WHERE SITE	PARTICLE	FIRST (-LAST) PATIENT	PATIENT TOTAL	DATE OF TOTAL		
Belgium	Louvain-la-Neuve	p	1991 (-1993)	21	1993		
Canada	Vancouver (TRIUMF)	$\pi^-$	1979 (-1994)	367	1994		
Canada	Vancouver (TRIUMF)	p	1995	195	Dec-15		
Czech Rep.	Prag (PTCCZ)	p	2012	780	Dec-15		
China	Wanjie (WPTC)	p	2004	1078	Dec-15		
China	Lanzhou	C-ion	2006	213	Dec-15		
China	Shanghai (SPHIC)	p	2014	76	Dec-15		
China	Shanghai (SPHIC)	C-ion	2014	149	Dec-15		
England	Clatterbridge	p	1989	2813	Dec-15		
France	Nice (CAL)	p	1991	5478	Dec-15		
France	Orsay (CFO)	p	1991	7580	Dec-15		
Germany	Darmstadt (GSI)	C-ion	1997 (-2009)	440	2009		
Germany	Berlin (HMI)	p	1998	2750	Dec-15		
Germany	Munich (RPTC)	p	2009	2725	Dec-15		
Germany	HIT, Heidelberg	p	2009	1187	Dec-15		
Germany	HIT, Heidelberg	C-ion	2009	2086	Dec-15		
Germany	WPE, Essen	p	2013	366	Dec-15		
Germany	UPTD, Dresden	p	2014	106	Dec-15		
Italy	Catania (INFN-LNS)	p	2002	350	Dec-15		
Italy	Pavia (CNAO)	p	2011	195	Dec-15		
Italy	Pavia (CNAO)	C ion	2012	561	Dec-15		
Italy	Trento (APSS)	p	2014	92	Dec-15		
Japan	Chiba	p	1979 (-2002)	145	2002		
Japan	Tsukuba (PMRC, 1)	p	1993 (-2000)	700	2000		
Japan	Chiba (HIMAC)	p	1994	138	Dec-15		
Japan	Chiba (HIMAC)	C ion	1994	10488	Dec-15		
Japan	Kashiwa (NCC)	p	1998	1580	Dec-14		
Japan	Hyogo (HIBMC)	p	2001	5024	Dec-15		
Japan	Hyogo (HIBMC)	C ion	2002	2386	Dec-15		
Japan	WERC	p	2002 (-2009)	62	2009		
Japan	Tsukuba (PMRC, 2)	p	2001	4502	Dec-15		
Japan	Shizuoka (PTCC)	p	2003	1873	Dec-15		
Japan	Koriyama-City (STPTC)	p	2008	2797	Dec-14		
Japan	Gunma (GHMC)	C ion	2010	1909	Dec-15		
Japan	Ibusuki (MMRI)	p	2011	1854	Dec-15		
Japan	Fukui City (Prefectural Hospital)	p	2011	846	Mar-15		
Japan	Nagoya (Nagoya PTC)	p	2013	1095	Dec-15		
Japan	Tosu (Saga-HIMAT)	C ion	2013	1136	Dec-15		
Japan	Nagano (Aizawa PTC)	p	2014	1	Oct-14		
Poland	Krakow (IFJ PAN)	p	2011	128	Dec-15		
Russia	Dubna (1)	p	1997 (-1996)	124	1996		
Russia	Moscow (ITEP)	p	1989	4368	Dec-15		
Russia	St. Petersburg	p	1975	1386	Dec-12		
Russia	Dubna (JINR, 2)	p	1999	1122	Dec-15		
South Africa	Capetown (Themba LABS)	p	1993	624	Dec-15		
South Korea	Ilsan, Seoul (KNCC)	p	2007	1781	Dec-15		
South Korea	Seoul (Samsung PTC)	p	2015	4	Dec-15		
Sweden	Uppsala (1)	p	1957 (-1978)	73	1978		
Sweden	Uppsala (2)	p	1989 (-2014)	1431	2014		
Sweden	Uppsala (The Skandion Clinic)	p	2015	32	Dec-15		
Switzerland	Villigen PSI (Piontron)	$\pi^-$	1980 (-1993)	503	1993		
Switzerland	Villigen PSI (OPTIS 1)	p	1984 (-2010)	5458	2010		
Switzerland	Villigen-PSI, incl OPTIS2	p	1996	2242	Dec-15		
USA, CA.	Berkeley 184	p	1954 (-1957)	30	1957		
USA, CA.	Berkeley	He	1957 (-1992)	2054	1992		
USA, NM.	Los Alamos	$\pi^-$	1974 (-1982)	230	1982		
USA, CA.	Berkeley	ions	1975 (-1992)	433	1992		
USA, MA.	Harvard (HCL)	p	1961 (-2002)	9116	2002		
USA, CA.	Loma Linda (LLUMC)	p	1990	18362	Dec-14		
USA, IN.	Bloomington (MPRI, 1)	p	1993 (-1999)	34	1999		
USA, CA.	UCSF - CNL	p	1994	1839	Dec-15		
USA, MA.	Boston (NPTC)	p	2001	8358	Dec-15		
USA, IN.	Bloomington (IU Health PTC)	p	2004 (-2014)	2200	2014		
USA, TX.	Houston (MD Anderson)	p	2006	6631	Dec-15		
USA, FL.	Jacksonville (UFPTI)	p	2006	6107	Dec-15		
USA, OK.	Oklahoma City (ProCure PTC)	p	2009	2079	Dec-15		
USA, PA.	Philadelphia (UPenn)	p	2010	3376	Dec-15		
USA, IL.	CDH Warrenville	p	2010	2316	Dec-15		
USA, VA.	Hampton (HUPTI)	p	2010	1369	Dec-15		
USA, NY.	New Jersey (ProCure PTC)	p	2012	1862	Dec-15		
USA, WA.	Seattle (SCCA ProCure PTC)	p	2013	844	Dec-15		
USA, MO.	St. Louis (S. Lee King PTC)	p	2013	270	Dec-15		
USA, TN.	Knowville (Provision Center)	p	2014	856	Dec-15		
USA, CA.	San Diego (Scripps PTC)	p	2014	400	Dec-15		
USA, LA.	Shreveport (Willis Knighton)	p	2014	151	Dec-15		
USA, FL.	Jacksonville (Ackerman CC)	p	2015	140	Dec-15		
USA, MN.	Rochester (Mayo PBTC)	p	2015	186	Mar-16		
USA, NJ.	Brunswick (Laurie PC)	p	2015	50	Dec-15		
USA, TX.	Irving (Texas Center for PT)	p	2015	1	Dec-15		
USA, TN.	Memphis (St. Jude PTC)	p	2015	1	Dec-15		
Total of all facilities (in and out of operation):					He	2054	1957-1992
					Pions	1100	1974-1994
					C-ions	19376	1994-2015
					Other ions	433	1975-1992
					Protons	131240	1954-2015
					Grand Total	154203	1954-2015

Figure 2.7: PTCOG statistics of patients treated in particle therapy facilities worldwide. [17]

patients have been treated with hadrontherapy, 131,240 of which with protons and 19,376 with carbon ions (Figure 2.7).

**Dose** While photons energy release decreases exponentially with the penetration depth (see Figure 2.3), showing a maximum between 1 - 3 cm, heavy ions have a completely different depth-dose profile. Charged particles lose their energy per unit length following the Bethe-Bloch formula defined in Section 1.3.1. The equation shows that in the initial part of its path through the tissue, the particle loses a relatively small amount of energy, being its velocity high and hence the interaction time with the electrons of the media low. In the final part of its path, when the kinetic energy is lowered down, the smaller velocities of the particles allow for a longer interaction time between the projectile and the electrons of the media. This results in a higher energy transfer and a higher energy loss of the projectile. The energy loss is thus maximum in a narrow region called "Bragg Peak" (BP), just before the hadron stops.

The particle range inside a target, described in Section (1.3.2), strongly depends

on the beam initial energy, so the Bragg Peak depth can be varied changing the beam parameters (see Figure 2.8).

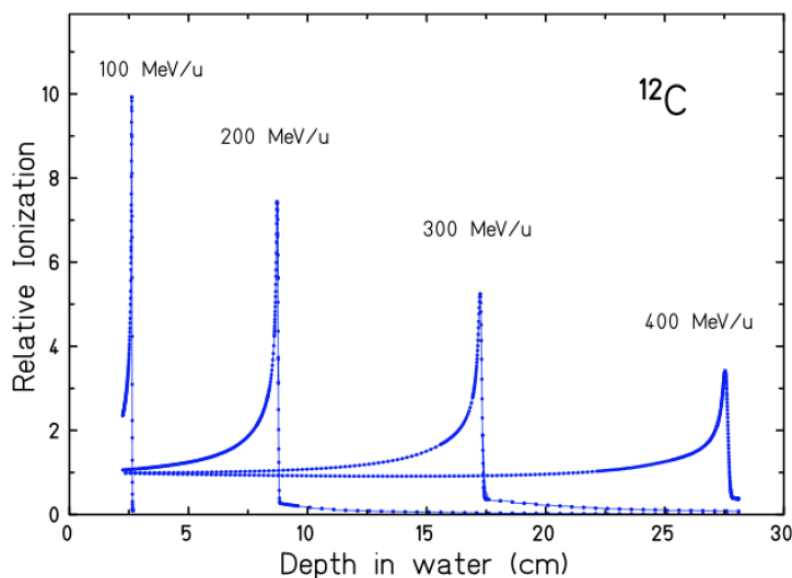


Figure 2.8: Measured depth-dose curves in water for carbon ions with different beam energies.

The peculiar energy loss in matter and the range dependence by the primary beam energy make hadron particles the best choice for oncological research and therapeutical purposes. The very precise and localized dose deposition leads to a dose release more conformal to the tumor volume than in traditional radiotherapy.

However the width of a single Bragg Peak is of few millimetres, while usually tumoral volumes amount to some centimetres. In the clinical practice, it is then necessary to superimpose several Bragg peaks obtained by multiple beams of slightly different energies, to realize a broader irradiation profile. The final result of this superimposition covers the cancerous area in the most uniform way and is called Spread Out Bragg Peak (SOBP).

**Biological Parameters** Ions with high energies have high velocities, so their LET is low ( $dE/dx \sim 1/v^2$ ) and their ionisation density is small; when the initial energy decreases, the LET increases, thus at the end of heavy ions path in tissues, around the BP position, the LET is very high and so is the RBE (Section 1.4.4). Furthermore the ionization electrons produced in the heavy ion beam interactions with matter have a mean free path of the order of few nanometres, providing a high probability for double ionizations on the DNA opposite strands, especially in the Bragg peak region (DSB, see section 1.4.1). Radiations with high-LET usually have a lower OER, as damage is caused

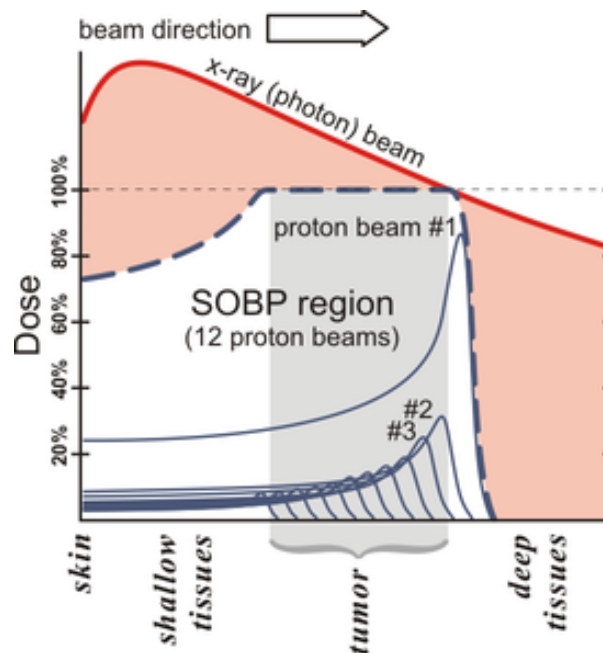


Figure 2.9: Superimposition of Bragg peaks in a cancer treatment. Comparison between radiation therapy with photons and protons

by ion direct collisions, less sensitive to the presence of oxygen compared to indirect hits induced by free-radicals, typical of X-rays. All these parameters differ between photons and hadrons, making the latter both a more suitable tool for cancer treatment (especially when sensitive organs like nerves, eyes, brain or intestine are located in the immediate proximity of the tumor) and a more effective weapon against particularly radioresistant tumors.

For these reasons, hadrontherapy, when compared to conventional radiotherapy, shows less short and long term side effects, improving the quality of life of the patients (adults and children) during and after the treatment. Furthermore, it reduces the likelihood of secondary malignancies caused by treatments, their insurgence being a percentage of risk of 16% for all cancer surviving patients.

Figure(2.11) shows the results of a retrospective study of 558 patients treated with proton radiation from 1973 to 2001 at the Harvard Cyclotron in Cambridge, MA. Second malignancies occurred in 29 proton patients (5.2%) and 42 photon patients (7.5%).

Secondary effects of diffused dose are especially relevant for pediatric patients, for whom the expected life span is longer.

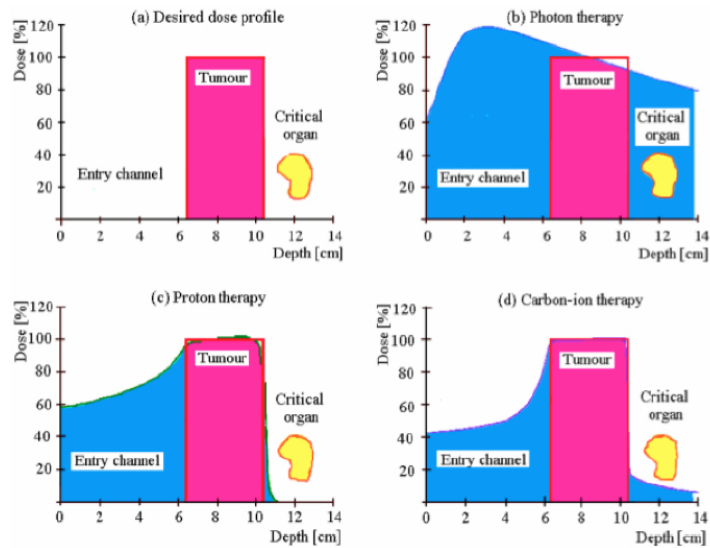


Figure 2.10: Comparison between desired dose profile and therapies with photons, protons and carbon ions for a given tumor volume (pink) in proximity to an OAR (yellow).

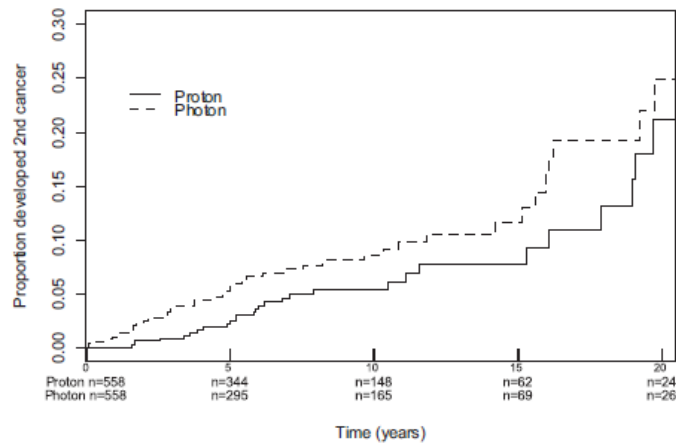


Figure 2.11: Cumulative incidence curves, measuring the disease frequency during 20 years for second cancer after radiation therapy for proton patients (solid line) and photon patients (dotted line). [18]

**Status and Prospects** The major drawback of hadrontherapy lies in the higher cost of an ions accelerator with respect to a standard radiotherapy equipment, in capital, in maintenance and servicing costs. In fact, considering protons, the high magnetic rigidity of the beam implies a bending radius of the order of 1 m; for heavy ions the situation is even worse: carbon ion facilities need large accelerators to bend and redirect ion

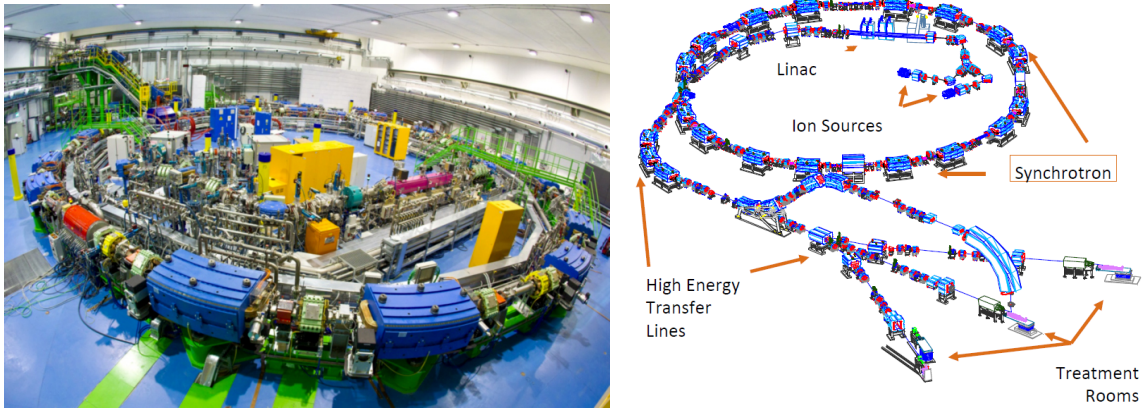


Figure 2.12: The accelerator in CNAO, Pavia located in the underfloor of the building, with scheme of the treatment rooms

beams. Therefore, to reach typical hadron therapy treatment energies ( $\sim 200\text{--}400\text{MeV}$ ), expensive synchrotrons with diameter of tens of meters (fig 2.12) are needed, a solution way different from compact LINACs for X-rays.

Another important aspect to be considered, is the fragmentation process (described in Section 1.3.3). In proton therapy, the nuclear inelastic interactions of the incident beam with the target tissues may lead to the fragmentation of the target nuclei, producing a non negligible amount of fragments outside the planned treatment volume. At present, in treatment planning, the proton RBE is assumed to have a constant value of 1.1 along all the range, as there is a lack of experimental measurements regarding target fragmentation [19]. Medical physics researches have underlined how a variable RBE can lead to a significant variation in local dose deposition, as studies show that the heavy particles produced by fragmentation have small ranges.

In Figure 2.13, green dots represent cells damaged directly by the ionization effect of radiation, while red dots represent the fragmentation contribute to cell killing. In the entry channel the ratio between cell damage by fragmentation and ionization is  $1/8$ , while the ratio reduces to  $1/40$  in correspondence of the Bragg peak. These data, estimated through the LEM model, a code adopted in the heavy ion treatment centres to estimate the carbon ions dose deposition, support the hypothesis that fragmentation of target is mainly relevant in spreading collateral damage to the healthy tissues crossed by the protons [20].

For what heavy ions fragmentation concerns, the effect of nuclear inelastic collisions result in the break up of the incident particle. The projectile fragments are produced mostly in the forward direction causing the collateral effect of an overdose that is delivered to tissues beyond the tumor volume, reflecting in a shifting of the distal end of the Bragg peak (see Figure 2.14).

The production of fragments with higher range and different directions than the pri-

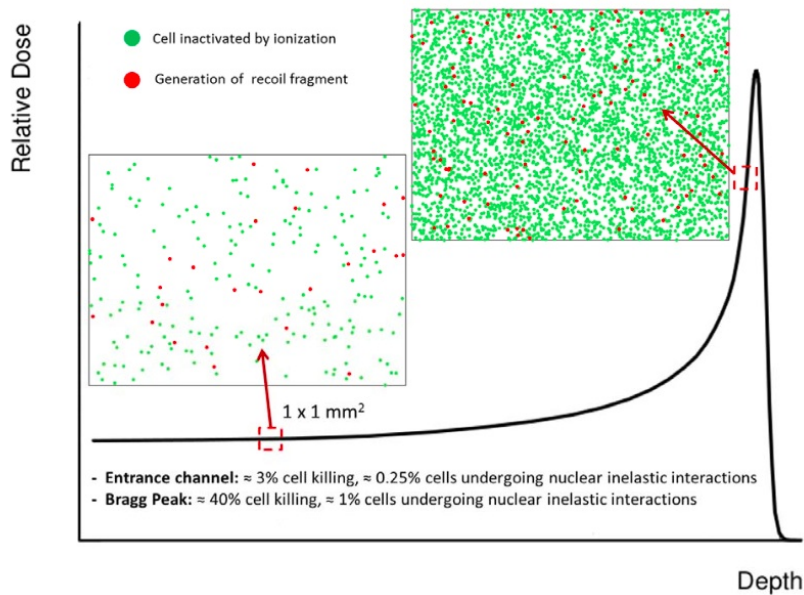


Figure 2.13: The graphic shows the effect of fragmentation of the target in sections of tissue of  $1\text{mm}^2$  for a beam of 250 MeV protons in water. The red dots represent fragmentation contribute.

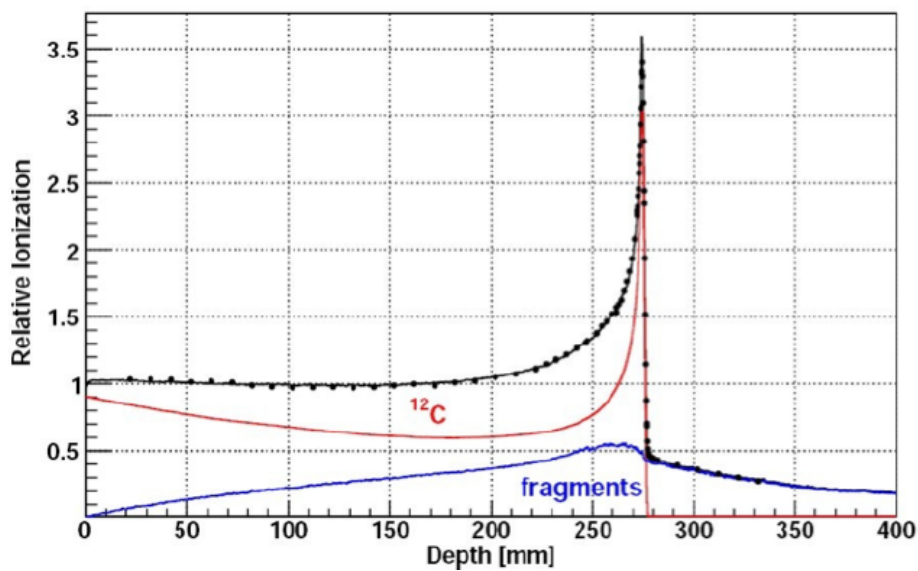


Figure 2.14: Bragg curve as a function of depth in water for a 400 MeV/u carbon ion beam; dose contribution from primary  $^{12}\text{C}$  ions (red line) and from secondary fragments (blue line)

mary ions cannot be neglected in treatment planning; therefore it is extremely important to improve knowledge on nuclear fragmentation in the hadrontherapy energy range. The FOOT (FragmentatiOn Of Target) experiment is born in this exact framework, in order to provide detailed measurements on nuclear fragmentation cross section for both proton and ion therapy. Details of the experiment will be explained in the next Chapter [3].

Currently, the particles used as projectile in hadrontherapy treatments are 50-250 MeV protons and 60-400 MeV  $^{12}\text{C}$  ions. Future options under consideration for hadrontherapy improvement are  $^4\text{He}$  and  $^{16}\text{O}$ . Since OER decreases with LET, the main reason for using oxygen ions as projectiles is its high radiobiologic effectiveness, especially on hypoxic tissues. However, the larger fragmentation of  $^{16}\text{O}$  beams as compared to lower Z ions, makes their use recommended only when high LET is needed [21]. In most cases, oxygen is suggested as a boost treatment in combination with lower LET particles; anyway, the correct assessment of the potential uses of this new particle is strictly related to a better knowledge of its fragmentation process. The advantage of helium ions lies in their negligible fragmentation, of main importance in treatments of highly risky areas or pediatric tumors;  $^4\text{He}$  has higher RBE than protons, but more limited lateral scattering.

The interaction between charged particles and matter does not permit a direct dose monitoring, as particle beams don't leave the patient, because they stop at Bragg peak, differently from X-rays. A monitor device can only rely on secondary particles produced during the treatment, that can be used for an on-line dose monitoring, as well as fragmentation products. Protons and carbon beams generate a huge amount of secondaries: prompt  $\gamma$ s, neutrons and charged particles and other fragments. At present, new techniques for dose monitoring in hadrontherapy are under study. Recently, the INSIDE (Innovative Solution for Dosimetry in Hadrontherapy) project [22] has been developed, aiming for a combined multi-mode on-line dose release monitor, compact and manageable, that will be integrated in one of the treatment rooms at the CNAO center in Pavia (Italy).

## 2.2 Radio-protection in Space

The 20th century will be remembered as the time in history when mankind left planet Earth for the first time; the 21st century may be the age of space exploration. The final goal of space programs is enabling life in space through a safe exploration and colonization of the Solar System and beyond. NASA and other space agencies have started since several years the study of health risk assessment for astronauts during long lasting space exploration journeys. Space is in fact an unsafe environment for humans and enabling life in space requires managing several health problems.

The high uncertainty on precise risk estimates and the lack of effective counter-measures make cosmic radiation one of the main health concerns for space exploration, possibly preventing these missions due to safety problems or increasing their costs to amounts beyond what would be acceptable.

The risks can be summarized into three categories [23]:

- *physiological problems caused by microgravity or reduced gravity*

The physiological changes in weightlessness have been largely studied, especially during long-term missions on space stations (ISS and Mir). The main effects are bone loss, kidney stone formation, muscle mass reduction, cardiovascular alterations, impaired sensory and motor capabilities, and immune system dysfunctions.

- *psychological and medical problems caused by isolation*

Isolation may lead to serious neurobehavioral problems caused by poor psychosocial adaptation. It also brings the problem of autonomous medical care, i.e. the capability to handle sickness or accidents in complete isolation.

- *acute and late damages caused by exposure to radiation*

The radiation environment in the Solar System is a complex mixture of particles of solar and galactic origin with a broad range of energies. The main known sources of energetic particles are Solar Particle Events (SPE), Galactic Cosmic Rays (GCR) and geomagnetically trapped particles (Figure 2.15). SPEs are characterized by a high and sporadic radiation emission, thus leading to acute and deterministic effects. GCR imply a chronic exposure associated with late stochastic effects. Trapped radiation is effective only inside Earth's magnetic field and occurs when charged particles are confined into the Van Allen belts; it is composed by  $\sim 10$  MeV electrons and  $\sim 100$  MeV protons.

At present time, various researches have been promoted by NASA [24] and other space agencies, in order to study the best methods to protect astronauts and electronics from radiation. Radio-protection is a difficult challenge in space: the high energy of the cosmic rays and the severe mass constraints in spaceflight represent a serious hindrance

to effective shielding. Passive and active shielding approaches are both areas of ongoing research. Passive protection relies on shielding materials to be used in spacecraft, habitats, vehicles, and space suits. Passive shielding can be effective for solar particle events, however, it is limited for galactic cosmic rays (GCR). Active protection involves the generation of electromagnetic or electrostatic fields to deflect space radiation and act as a shield. Other strategies include the choice of an appropriate mission planning and ability to predict solar particle events, administration of drugs or dietary supplements to reduce the radiation effects and crew selection based on genetic screening.

Another crucial field of research for the protection of crew personnel is hibernation. Hibernation is a state of reduced metabolic activity used by some animals to survive in harsh environmental conditions. The idea of exploiting hibernation for space exploration has been firstly proposed in mid 20th century and has become more and more realistic in recent years, thanks to the introduction of specific methods to induce hibernation-like conditions (synthetic torpor) in non-hibernating animals [25]. In addition to the expected advantages in terms of resource consumptions, ageing, and psychology, data in animal models suggest that radiation effects are reduced during hibernation.

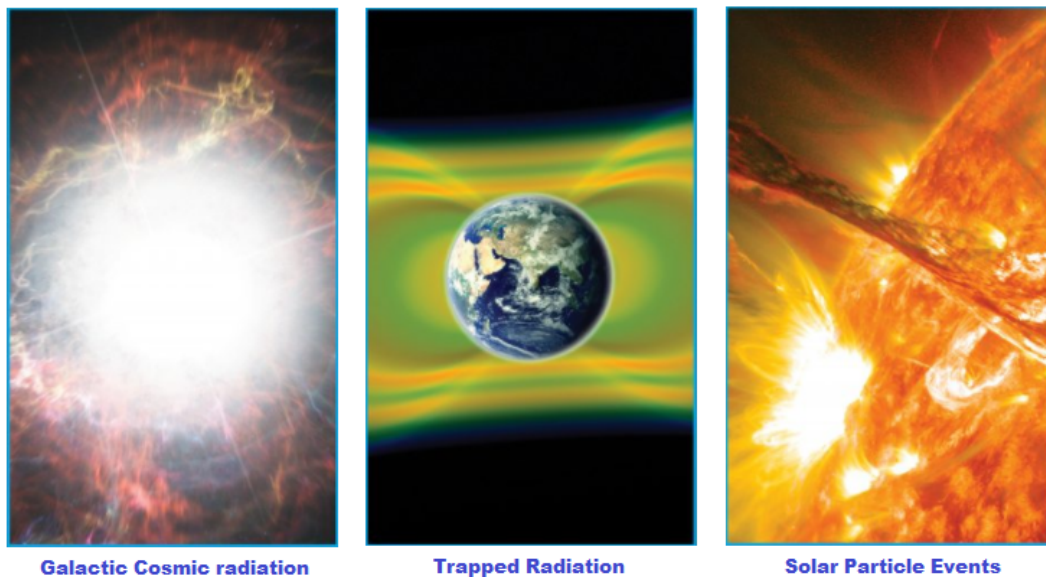


Figure 2.15: Sources of energetic particles

## 2.2.1 Galactic Cosmic Radiation

Galactic cosmic radiation is originated outside the Solar System and arrives isotropically on Earth. Because of their high energies (up to  $10^{14}$  MeV), they most probably originate from supernova explosions, neutron stars, pulsars, or other sources where high energetic phenomena are involved. The radiation consists of protons, helium, electrons and heavier nuclei.

A late radiation morbidity is associated with the chronic exposure to galactic cosmic radiation (GCR), including cancer and other diseases of old age. The uncertainty in radiation risk estimates is very high, especially for carcinogenesis, central nervous system and late cardiovascular damage.

For what radiation protection concerns, shielding remains the only feasible countermeasure, but it cannot be a full solution for the GCR problem, even though it can significantly contribute to risk reduction. The very high energy of the cosmic rays represents a serious hindrance to effective shielding. Current uncertainties on biological effects are too high for long term exploratory missions, like a voyage to Mars.

There is a common ground between protecting astronauts from radiation exposure in space and providing therapy to cancer patients using heavy ions. In fact, the pull of particle species currently available (photons and Carbon) and those considered as promising alternative candidates (Helium, Lithium and Oxygen) are some of the most abundant in space. The shared interest in ion species and energy range between hadrontherapy and radioprotection in space allows the interchange of cross sections data, opening a new area of common research.

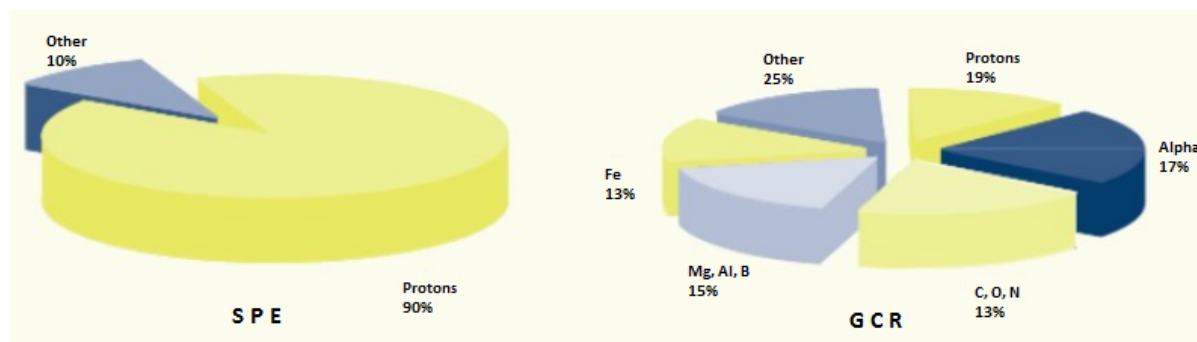


Figure 2.16: Relative contribution of different components of space radiation to dose equivalent for Solar Particle Events (SPE) on the left and for Galactic Cosmic Rays (GCR) on the right.

### 2.2.2 Solar Particle Events

Besides electromagnetic radiation, the Sun continuously emits particle radiation, consisting mainly of protons and electrons, the so called "solar wind". However, occasionally the surface of the Sun releases large amounts of energy in sudden local outbursts; in these SPE large currents and moving magnetic fields in the solar corona accelerate solar matter. Coronal particles, mostly protons ( $\sim 90\%$ ) and about 10% of heavier nuclei, with energies up to several GeV escape into the interplanetary space [26].

SPE show an enormous variability in particle flux and energy spectra, but the most intense events have the potential to expose unshielded space crews to life threatening doses. For radiation protection purposes, it is important to predict intensity, energy, and duration of a SPE. In general, energies of SPE are lower than GCR, and shielding is therefore a possible solution. Storm shelters, small areas with thick shields, are included in spacecrafts and can be built in planetary stations. Maximum risk will be during extra-vehicular activities with minimal shielding, especially planetary exploration.

Since, unlike GCR, intense SPE can be life threatening or induce acute radiation syndromes (including nausea and vomiting), they represent not only a health problem, but an operational issue of great concern.

## Chapter 3

# The FOOT (FragmentatiOn Of Target) experiment

The FOOT experiment is a collaboration project, funded by INFN with contribution of Centro Fermi institute. Besides Italian institutions like CNAO in Pavia, further international collaborators of Nagoya University and GSI support the project. The FOOT experiment is designed to measure target and projectile fragmentation cross sections in order to improve the accuracy of treatment plans for hadrontherapy. The results can bring a more accurate knowledge of the biological effects of fragmentation on organic tissues, allowing the application of variable RBE models for ions thanks to the obtained data. The measurements performed with the FOOT experiment could also be interesting for other applications, like radioprotection in space, as a detailed knowledge of fragmentation cross section is required for the design and optimization of spacecraft shielding.

In case of proton beams, only target fragmentation occurs, generating a spectrum of low energy heavy recoils that depends on beam energy and on target materials. These secondary charged particles have short range (e.g. order of 10-100  $\mu\text{m}$ ), very high LET and RBE. For heavier ion beams, projectile fragmentation also takes place and is responsible for the dose tail observed after the BP. The projectile fragmentation has been partly examined for carbon ions, only in a small energy range [27], [28]. Furthermore, the study of the target fragmentation for both proton and heavy ions lacks of available experimental data. The purpose of FOOT experiment is to measure target fragmentation both in proton and carbon therapy and the projectile fragmentation in carbon therapy. Moreover, the project will provide data of cross sections for new, high LET ions, like Oxygen.

The FOOT data taking will be held at CNAO's experimental room; the proton beam of TIFPA (Trento Institute for Fundamentals Physics Applications) and LNS ion beams will be fundamental for calibration purpose. Data taking is foreseen to take place in late 2019 - 2020.

## 3.1 Measurements of target fragmentation

In order to perform measurements regarding target fragmentation when hit by a photons beam, the main challenge is the detection of short range (see Table 3.1) and low kinetic energy (few MeV) fragments.

Fragment	E (MeV)	LET (keV/ $\mu\text{m}$ )	Range ( $\mu\text{m}$ )
$^{15}\text{O}$	1.0	983	2.3
$^{15}\text{N}$	1.0	925	2.5
$^{14}\text{N}$	2.0	1137	3.6
$^{13}\text{C}$	3.0	951	5.4
$^{12}\text{C}$	3.8	912	6.2
$^{11}\text{C}$	4.6	878	7.0
$^{10}\text{B}$	5.4	643	9.9
$^8\text{Be}$	6.4	400	15.7
$^6\text{Li}$	6.8	215	26.7
$^4\text{He}$	6.0	77	48.5
$^3\text{He}$	4.7	89	38.8
$^2\text{H}$	2.5	14	68.9

Figure 3.1: Expected average physical parameters for target fragments produced in water by a 180 MeV proton beam. [20]

Thus, a fragment produced by a proton projectile impinging a target material deposits all of its energy locally, not being able to escape from the surface of the medium and so not allowing any possibility of detection. Therefore a thick target cannot be the right choice for a fragmentation experiment. On the other hand, a very thin target can provide technical difficulties, both in its production and in the handling of such a thin item ( $\sim \mu\text{m}$ ). Moreover a significant lowering of fragmentation rate will occur, making it hard to achieve the desired amount of data.

### 3.1.1 Inverse kinematic

In order to overcome the issues related to the target fragments, an inverse kinematic approach is used, which means that, instead of studying the fragmentation of proton beams on organic matter, the role is switched and the beams are respectively composed of different ions (mainly  $^{12}\text{C}$ , and  $^{16}\text{O}$  which are the principal components of the human body) addressing a proton target. The secondary fragments in the inverse kinematic approach are from the projectile and have boosted energy and a much longer range with respect to the standard approach. This allows to perform the measurements with a thicker target, providing thus an acceptable fragmentation rate.

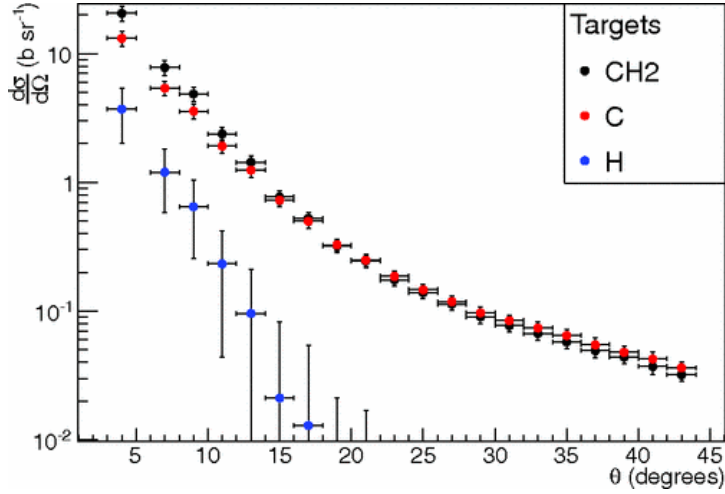


Figure 3.2: Combination of carbon and CH<sub>2</sub> targets angular distribution to determine the hydrogen angular distribution for  $\alpha$  fragments. The angular distribution for the hydrogen target is the difference between both, divided by two [27].

### 3.1.2 Target Material

The inverse kinematic approach implies the use of an hydrogen enriched target. With a target of polyethylene (C<sub>2</sub>H<sub>4</sub>), the cross section of H can be extracted by subtraction from the coupled data obtained using both C<sub>2</sub>H<sub>4</sub> and pure C target, according to the equation (3.1) below

$$\frac{d\sigma}{dE_{kin}}(\text{H}) = \frac{1}{4} \left( \frac{d\sigma}{dE_{kin}}(\text{C}_2\text{H}_4) - 2 \frac{d\sigma}{dE_{kin}}(\text{C}) \right) \quad (3.1)$$

In the FOOT experiment it has been decided to use polyethylene C<sub>2</sub>H<sub>4</sub> and graphite C targets 2 mm thick, as these are easy to produce and manage.

The FOOT performances in terms of cross section measurement were evaluated using simulated data of <sup>12</sup>C at 200 MeV/u. To check the validity of the combinational method both the cross section on hydrogen target and the cross section obtained from the difference method were evaluated. The comparison of the results shows that the two estimation are in good agreement, thus validating the combination method (figure 3.3, 3.4).

A target of methylene (CH<sub>2</sub>) has already been tested at the experimental center GANIL (Grand Accélérateur National d'Ions Lourds), France [27], proving that the subtracting cross section method can be effectively used (results are shown in Figure 3.2).

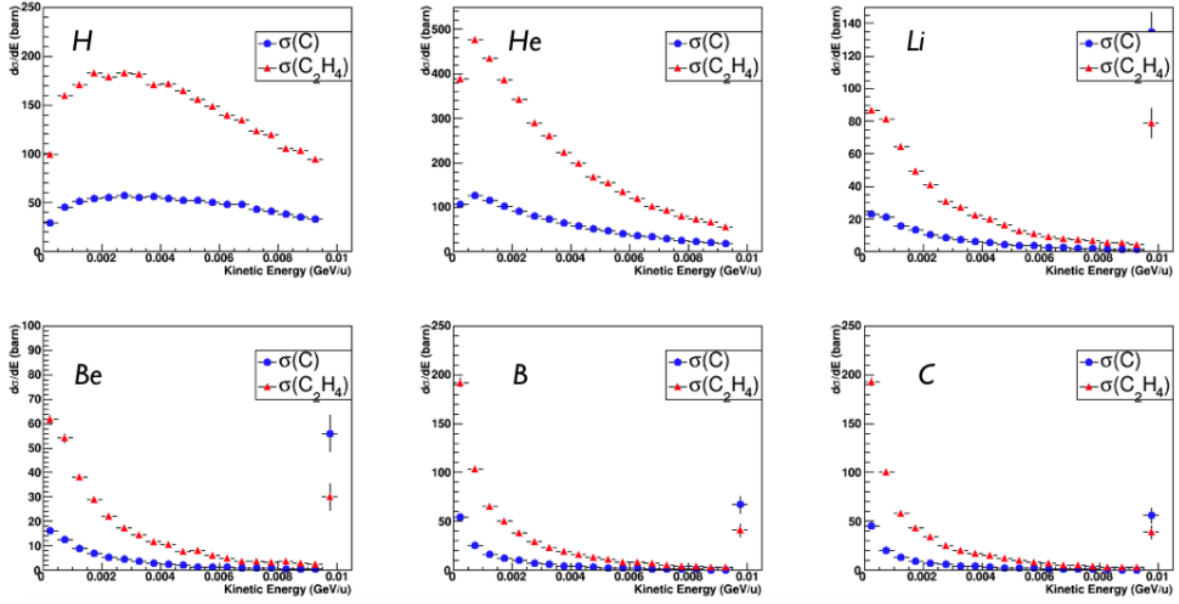


Figure 3.3: Energy differential cross-sections of different fragments in inverse kinematics. Results obtained for C and  $C_2H_4$  targets are reported as blue dots and red triangles, respectively.

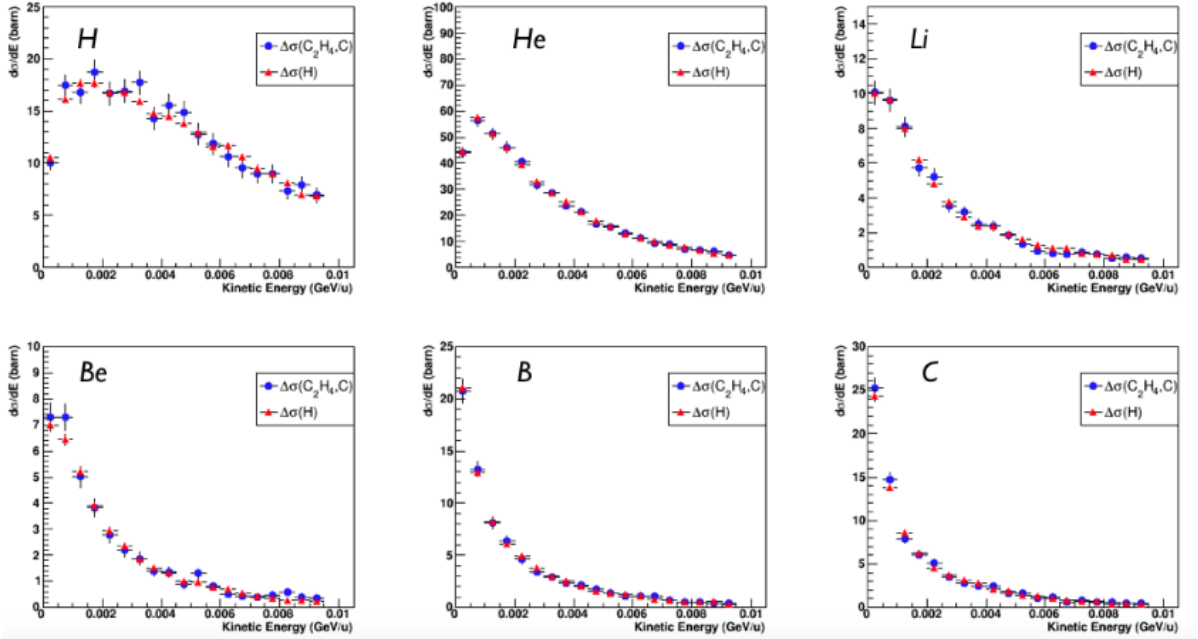


Figure 3.4: Energy differential cross-section of a 200 MeV/u  $^{12}C$  beam on hydrogen target in inverse kinematics. The estimations performed with the  $\Delta\sigma(C_2H_4)$  and  $\sigma(H)$  methods are reported as blue dots and red triangles respectively.

## 3.2 The FOOT apparatus design criteria

The general idea of FOOT is to design a portable experimental setup, able to detect those fragments of interest which could release a relevant dose outside the planned target region. The apparatus should be easily transportable allowing data taking in various treatment and research centers. Moreover the experimental rooms of hadrontherapy facilities are usually of limited dimension.

In order to measure the fragment production due to protons and heavier ions, we need to study the impact of beams of carbon and oxygen ions ( $\sim 100 - 300$  MeV/u) on a  $C_2H_4$  target. As previously explained in Chapter (2.1.2), lower mass fragments (protons, deuterons, etc.) can be emitted within a wider angular aperture with respect to heavier nuclei. Figure (3.5) shows a Monte Carlo simulation of the angular distribution of the fragments produced by an incident oxygen beam of 200 MeV/u. A similar distribution is obtained with a carbon incident beam of the same energy. All the particles with  $Z > 2$  are produced in the forward direction with  $\theta \leq 10^\circ$ , while helium and protons have wider scatter angles,  $\theta \gg 10^\circ$ .

Due to the difficulty to combine the fact that the apparatus should be of limited size and the need to achieve the desired acceptance for both heavy ( $Z > 2$ ) and light ( $Z \leq 2$ ) particles, it has been decided to implement two different experimental setups:

- **Heavy Ions**

a setup based on electronic detectors and a magnetic spectrometer, covering an angular acceptance of  $10 - 20^\circ$  with respect to the beam axis, for the identification and measurements of fragments heavier than  $^4He$ .

- **Light Ions**

a setup with an emulsion spectrometer for the detection of fragments at large angles ( $\sim 70^\circ$ ); a specific emulsion chamber is needed to measure the production of light charged fragments as protons, deuterons, tritons and helium nuclei.

### 3.2.1 Heavy Ions Setup

The heavy ions experimental setup, is focussed on providing cross section data of fragments with  $Z > 2$ , which are currently missing in scientific literature in hadrontherapy energy range. The detector design has been chosen to be as compact as possible, and its size should measure within 1.5 and 3 meters, making it easily transportable and capable of exploiting different particles beams at various therapeutic centres, like CNAO, HIT and GSI. The design of the experiment was driven by the contribution of previous experiments as the FIRST one [28], performed in 2011 at GSI facility (Darmstadt, Germany), in combination with FLUKA simulation of the fragmentation (see example of data taken in the FIRST experiment in Figure 3.5).

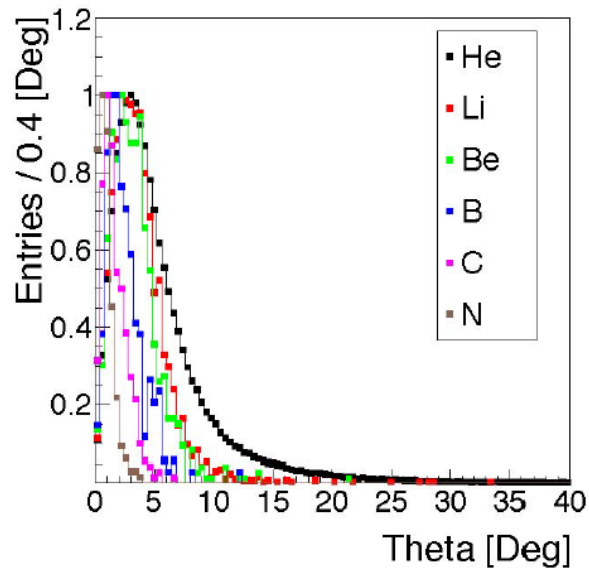


Figure 3.5: Polar angle distribution for fragmnets produced by a  $^{16}\text{O}$  beam with 200MeV/u smashing on a polyethylene target; data from FLUKA simulation.

The detector can be divided downstream in three different regions, as shown in the schematic representation in Fig. (3.6) below:

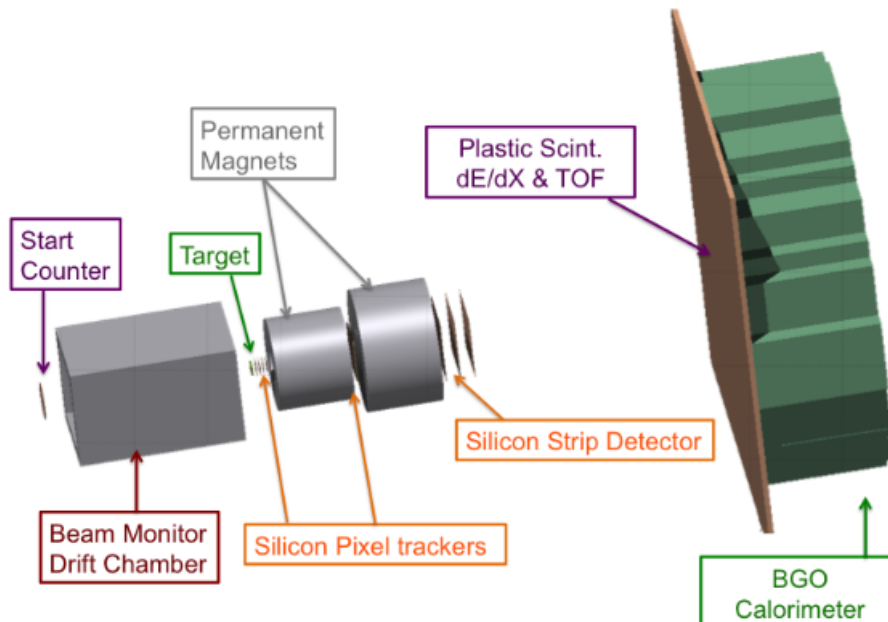


Figure 3.6: Schematic view of the FOOT apparatus as electronic detector setup.

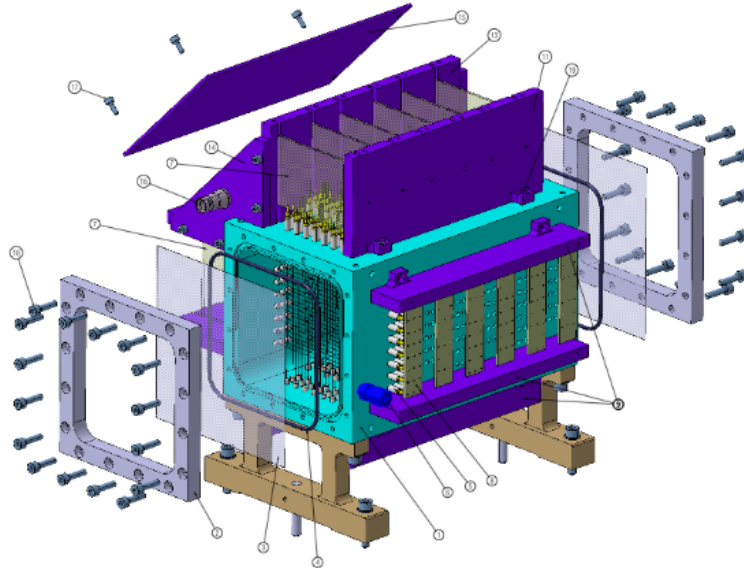


Figure 3.7: Technical drawing of the BM drift chamber.

- **Upstream Region:** it is the entrance and target region of the apparatus and provides a counter for the rate of the ion beam and a beam monitor which tracks the beam position and direction.
  - Start Counter (SC): a plastic scintillator detector used to measure the incoming rate of the ion beam and to provide a trigger signal for the start time of the Time Of Flight (TOF) apparatus. It has been proposed to reuse the SC of the FIRST experiment, a  $250\mu\text{m}$  thick device with 4 channels read out by fast PMT; the thickness was minimized to reduce the pre-target probability of interaction.
  - Beam Monitor (BM): a drift chamber consisting of 12 alternated horizontal and vertical layers of wire (planes), with 3 drift cells per layer (rectangular,  $16\text{mm} \times 10\text{mm}$ ). Planes are alternatively oriented along the X and Y axes, in order to better reconstruct the beam profile, while the 3 cells provide the measurements of the coordinates. The geometrical layout has been optimized in order to minimize ions interactions with the wires. It has been proposed to use the drift chamber already constructed and adopted in the FIRST experiment. A technical drawing of the drift chamber is shown in Fig. (3.7).
  - Target: both polyethylene  $\text{C}_2\text{H}_4$  and graphite C targets are needed in order to perform the subtraction of cross section method (see section 3.1.2). The thickness of the target is chosen to be around 2mm, avoiding both the fragment trapping effect and the excessive drop of the interaction rate.

- **Magnetic Spectrometer:** the overall FOOT tracking system is arranged in three tracking elements in order to better measure the fragments momentum. A telescope of pixel trackers provides the vertex reconstruction and the initial tracking of the produced fragments. Then, the fragments enter a magnetic region, given by two permanent magnets; between the two magnets, an additional silicon pixel tracker detector measures 2 points on the fragments trajectories. After the two magnets, a microstrip silicon detector is placed, composed of two layers; it is fundamental not only for a better spatial measurement but also to match the reconstructed tracks with the hits in the next elements (scintillator and calorimeter) which provides the first measurement of fragments  $\frac{dE}{dx}$ .
  - Vertex Tracker (VTX): four layers of silicon pixel detector, placed right after the target, to be used as vertex detector. The four layers will use as a sensing element the M28 chip (see fig 3.9),  $50\mu\text{m}$  thick, with  $207\mu\text{m}$  pitch. The stack of sensor is schematically shown in Figure (3.8).
  - Permanent Magnets: two permanent magnets with Halbach geometry supply the necessary magnetic field in order to perform the momentum measurement of the charged fragments. The characteristic Halbach cylindrical geometry provides a maximum transversal field of 0.8 T at the centre. (Fig. 3.10)
  - Inner Tracker (IT): two planes of pixel sensors to measure both the position of the particle in the plane orthogonal to the beam axis and the direction of the track. The area covered between the two magnets will be of  $8\text{cm} \times 8\text{cm}$ , made of two planes of 16 M28 sensors, the same technology of the VTX, simplifying in this way the DAQ. A 2 mm thick plate made of a particular low density foam of SiC will work as a spacer to define the distance between the two planes. (Figure 3.11)
  - Outer Tracker (OT): it has been decided to use a 3 layers microstrip silicon detector in order to have better resolution on the momentum measurement, and to reduce the impact of multiple scattering and secondary fragmentation. Due to its small thickness the detector will be placed as close as possible to the last magnet and will also provide precise  $dE/dx$  measurements for fragments. The total surface that ought to be covered is  $9\text{cm} \times 9\text{cm}$  to cover the expected angular acceptance of  $10^\circ$ .
- **Calorimeter region:** it is the last part of the experimental setup for heavy ions. Downstream the magnetic spectrometer region, the fragments travel around 1 meter to reach a 2 layer scintillator, which main purpose is the measurement of the  $dE/dx$  and the TOF. Finally, the kinetic energy of the fragments is determined by a BGO crystal calorimeter.
  - Scintillator (SCI): the detector is made of two layers of 20 plastic scintillator

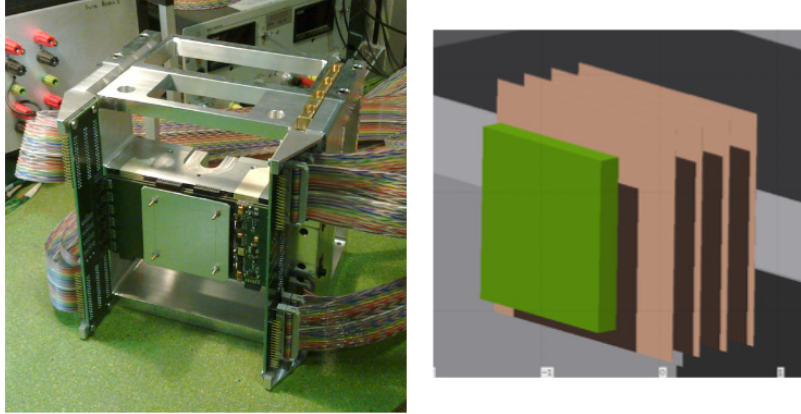


Figure 3.8: Target and vertex tracker geometrical scheme.

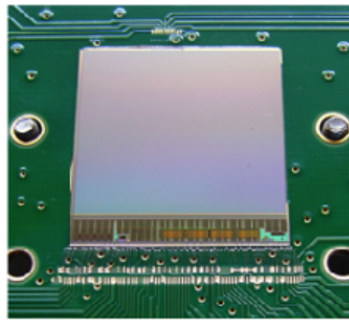


Figure 3.9: M28 pixel sensor picture.

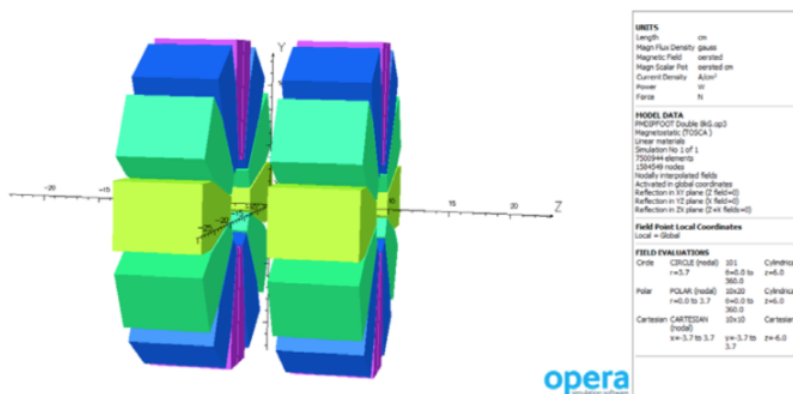


Figure 3.10: Double magnet design.

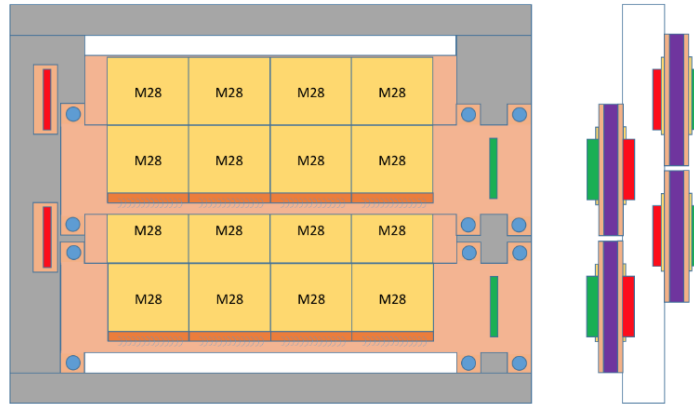


Figure 3.11: Inner tracker scheme.

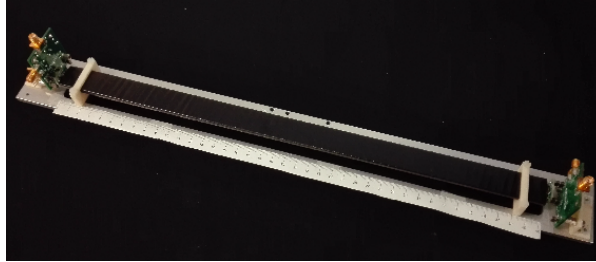


Figure 3.12: Picture of a single scintillator bar.

bars (Figure 3.12), arranged orthogonally one another in order to obtain a direct XY position identification. Each bar is 440 mm long and 20 mm large; the best thickness value is being investigated as, when the bar thickness increases, the time resolution improves, but the fragmentation probability inside the detector grows (currently  $\sim 3$  mm). The  $40 \times 40$  cm<sup>2</sup> size of the scintillator is dictated by the emission angle of the heavy fragments at 1 m distance.

- Calorimeter (CAL): it is the last element of the detector, designed to measure the energy of the particles produced by fragmentation in the target. The calorimeter will be a cylindrical detector composed of about 360 BGO (Bi<sub>4</sub>Ge<sub>3</sub>O<sub>12</sub>) crystals, covering a circular surface of about 20 cm radius. This corresponds to a transverse size of the crystals of  $2 \times 2$  cm<sup>2</sup>, granularity requested to keep the probability for multiple fragments to hit the same crystal under the % level.

### 3.2.2 Light Charged Particles Setup

The experimental setup designed to detect and study light ( $Z \leq 2$ ) products of fragmentation, is an Emulsion Spectrometer (ES), with angular acceptance of  $\sim 80^\circ$ .

The Start Counter and the Beam Monitor will be the same as for the heavy ions experimental setup, as they provide informations about the incident beam. All the other detectors will be replaced by the ES, as shown in Figure (3.13) below.

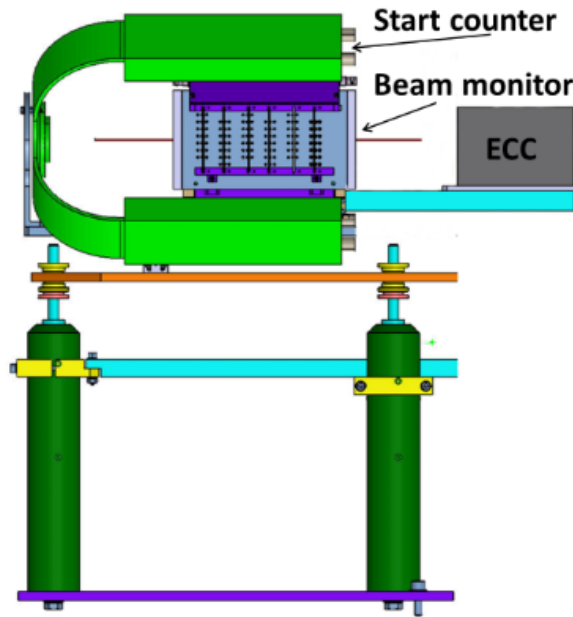


Figure 3.13: Emulsion Spectrometer setup inside the FOOT detector; light ions framework.

The Emulsion Spectrometer of the FOOT experiment is based on the Emulsion Cloud Chamber (ECC) concept [29], that consists in a compact integration of target and detector: a sequence of nuclear emulsion films (detector) are alternated to layers of passive materials, Pb, C or  $\text{CH}_2$  (target). The emulsion films work both as high resolution tracking devices and ionizing detectors; they are currently the unsurpassed best choice among tracking devices for what spacial resolution concerns ( $\sim 0.06\mu\text{m}$ ).

The nuclear emulsion films consist of two  $50\mu\text{m}$  thick sensitive regions of AgBr crystals in a gelatine binder, attached on both sides of a  $200\mu\text{m}$  plastic base. When particles cross the films, a chemical process known as "development" induces the growth of silver clusters called *grains*, with a diameter of  $0.6\mu\text{m}$  which can be seen with an optical microscope. After the data taking, the emulsion will be scanned by an automated microscopy system for emulsion readout which has a dedicated software for track reconstruction.

The structure of ECC proposed for the FOOT experiment has great portability, as

it measures less than 10 cm and is composed of three different sections, as illustrated in the figure (3.14) below:

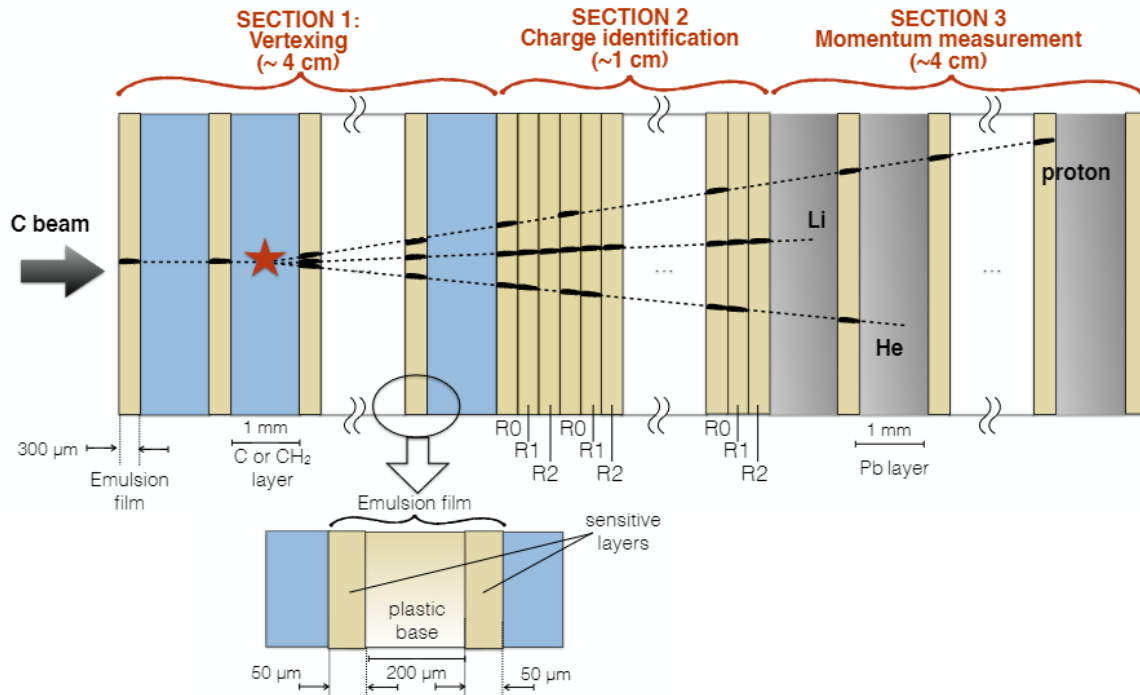


Figure 3.14: Detailed scheme of the ECC structure for the FOOT experiment.

- **SECTION 1, Vertexing** ( $\sim 4$ cm): the first section is composed by 60 alternated layers of emulsion films ( $300\mu\text{m}$ ) and target layers of Carbon or  $\text{CH}_2$  (1 mm); the  $^{12}\text{C}$  beam interacts with the target and originates secondary fragments. The thickness of the layers is optimized to achieve a statistically significant number of interactions.
- **SECTION 2, Charge identification** ( $\sim 1$  cm): the second section is composed of emulsion films only and is used to identify the atomic numbers of low charged fragments. The specific ionization along the particle track is proportional to the grain density, as well as the particle charge. The sum of the grain pixels belonging to the same track, normalized to a given track length is a variable called "track volume", which is sensitive to the particle charge (see graphics in Fig. 3.15 [30])
- **SECTION 3, Momentum measurement** ( $\sim 4$  cm): the third and last section is made of  $300\mu\text{m}$  thick emulsion layers alternated with 1 mm thick lead plates. The number of layers varies (from 10 to 50) according to the energy of the incident beam. There are two independent methods to calculate the momentum of the

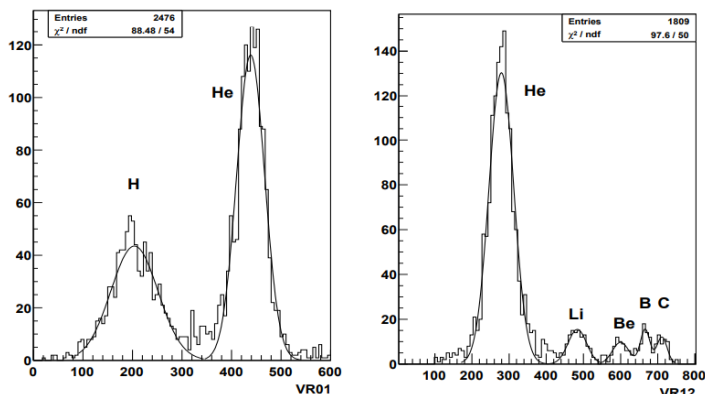


Figure 3.15: Track volume distributions providing the charge separation between Hydrogen and Helium (H-He) and Helium, Lithium, Beryllium, Boron, Carbon (He-Li-Be-B-C).

fragment. The first is estimating it by its correlation with the range, measuring the total length of the particle track and then using data supplied by NIST [31]. The second one, is the Multiple Coulomb Scattering (MCS) method [32], which estimates the momentum according to the following formula:

$$p(\text{MeV}/c) = \frac{13.6}{\beta \cdot \delta(\text{mrad})} \sqrt{\frac{x}{X_0}} \quad (3.2)$$

where  $p$  is the momentum,  $\beta$  the particle velocity,  $x$  the traversed distance,  $X_0$  the radiation length in the material and  $\delta\vartheta$  the deviation of the track slope along its path.

### 3.3 Expected Performances

The FOOT experiment has to satisfy various requirements in order to allow a precise identification of the particles produced by fragmentation. The experimental setup measures the following quantities: momentum, kinetic energy,  $\Delta E$  and Time Of Flight (TOF). The performances of the detector that need to be achieved are:

- momentum resolution  $\frac{\sigma(p)}{p}$  at the level of 5%;
- time of flight TOF resolution at the level of 100 ps;
- kinetic energy resolution  $\frac{\sigma(E_k)}{E_k}$  at the level of 2%;
- energy loss  $\frac{\sigma(\Delta E)}{\Delta E}$  at the level of 2%

### 3.3.1 Momentum measurement

The main goal of the FOOT experiment is to evaluate the differential nuclear fragmentation cross section for particles used for hadrotherapy or radioprotection purpose with an uncertainty of less than 5%. In order to reach this goal, a momentum resolution of at least 5% is required.

The momentum measurement is performed by the three tracking detectors placed beyond the target, in combination with the magnetic field ( $B \text{ max} \simeq 0.8 \text{ T}$ ); the silicon trackers are placed exactly before (VTX), in the middle (IT), and right after (OT) the permanent magnets. Using the measurements obtained from the detectors, it is possible to reconstruct and fit the track of the fragment and successively extrapolate the momentum. The global tracking fit is performed using the GENFIT framework [33], an open source fitting toolkit suitable for a wide variety of experiments. GENFIT, besides a variety of different track-fitting algorithms, implements a Kalman filter based tracking algorithm, which gives one of the best possible performances. Details of the algorithm will be explained in next chapter.

### 3.3.2 Particle identification

The first step for the cross section measurement is the correct identification of the fragments produced, through the determination of their atomic ( $Z$ ) and mass ( $A$ ) numbers. A fragment is indeed univocally defined by  $Z$  and  $A$ ; the quantities measured thanks to the FOOT experimental setup ( $p, E_{kin}, \Delta E, TOF$ ) suffice for a good particle identification. The strategy used for the determination of  $Z$  and  $A$  follows:

**Charge ( $Z$ )** The fragment charge identification is given by the scintillator by measurement of the particle energy loss  $\frac{dE}{dx}$ , expressed by the Bethe Bloch formula 1.6, recalled below:

$$-\frac{dE}{dx} = \frac{\rho \cdot Z}{A} \frac{4\pi N_A m_e c^2}{M_U} \left( \frac{e^2}{4\pi\epsilon_0 m_e c^2} \right)^2 \frac{z^2}{\beta^2} \left[ \ln \left( \frac{2m_e c^2 \beta^2}{I \cdot (1 - \beta^2)} \right) - \beta^2 \right] \quad (3.3)$$

The scintillator detector provides the measurement of a particle energy release  $\Delta E$  in a path length  $\Delta x$ . Moreover the TOF is computed from the time measurement of the scintillator read in coincidence with the trigger-time supplied by the start counter: thus, through the TOF, the  $\beta$  can be determined. Knowing both  $\frac{dE}{dx}$  and  $\beta$  provided by the scintillator, it is possible to estimate the fragment charge  $Z$  from the Bethe-Block itself.

The graphics in Figure (3.16) shows the determination of the charge number  $Z$  for all the fragments studied in the experiment; it is evident how well distinguished the peaks are, allowing a clear charge identification.

The final results for all the fragments are summarized in Table (3.3.2). The uncertainty associated to the values is the  $\sigma$  of the gaussian fit; the resolution of Z improves with increasing fragment charge, passing from  $\sim 6\%$  for  ${}^1\text{H}$  to  $2\%$  for  ${}^{16}\text{O}$ .

Fragment	${}^1\text{H}$	${}^4\text{He}$	${}^7\text{Li}$	${}^9\text{Be}$	${}^{11}\text{B}$
Z	1	2	3	4	5
Reconstructed Z	$1.01 \pm 0.06$	$2.01 \pm 0.07$	$3.02 \pm 0.08$	$4.05 \pm 0.10$	$5.06 \pm 0.12$

${}^{12}\text{C}$	${}^{14}\text{N}$	${}^{16}\text{O}$
6	7	8
$6.08 \pm 0.14$	$7.11 \pm 0.16$	$8.15 \pm 0.18$

Table 3.1: Reconstructed Z for the studied fragments; the uncertainty associated to the mean value is the  $\sigma$  of the gaussian fit. The Z resolution runs from 2 to 5%.

**Mass (A)** The fragment mass number A can be evaluated through different methods, thanks to the redundancy of detectors measurements. The different approaches are listed below:

- through the combination of the **p** and the **TOF** measurements:

The determination of  $\beta$ , the particle velocity, is obtained by  $\beta = \frac{L}{TOF}$  where L is the distance covered by the fragment.

$\gamma = 1/\sqrt{1 - \beta^2}$  is the Lorentz factor related to  $\beta$ .

Thus we have:  $p = m\beta\gamma \Rightarrow m = \frac{p}{\beta\gamma}$

$$A_1 = \frac{m}{U} = \frac{p}{U\beta\gamma} = \frac{pTOF}{UL\gamma} \quad (3.4)$$

where the momentum  $p$  is the fitting result of the tracker detectors and  $U$  is the Unified Atomic Mass ( $\approx 931.5$  MeV)

- through **E<sub>kin</sub>** and **TOF**:

$\beta$ , the particle velocity, is obtained by  $\beta = \frac{L}{TOF}$  where L is the distance covered by the fragment.

$$A_2 = \frac{m}{U} = \frac{E_{kin}}{U(\gamma - 1)} = \frac{E_{kin} \sqrt{1 - \beta^2}}{U(1 - \sqrt{1 - \beta^2})} \quad (3.5)$$

where  $E_{kin}$  is the kinetic energy measured by the calorimeter.

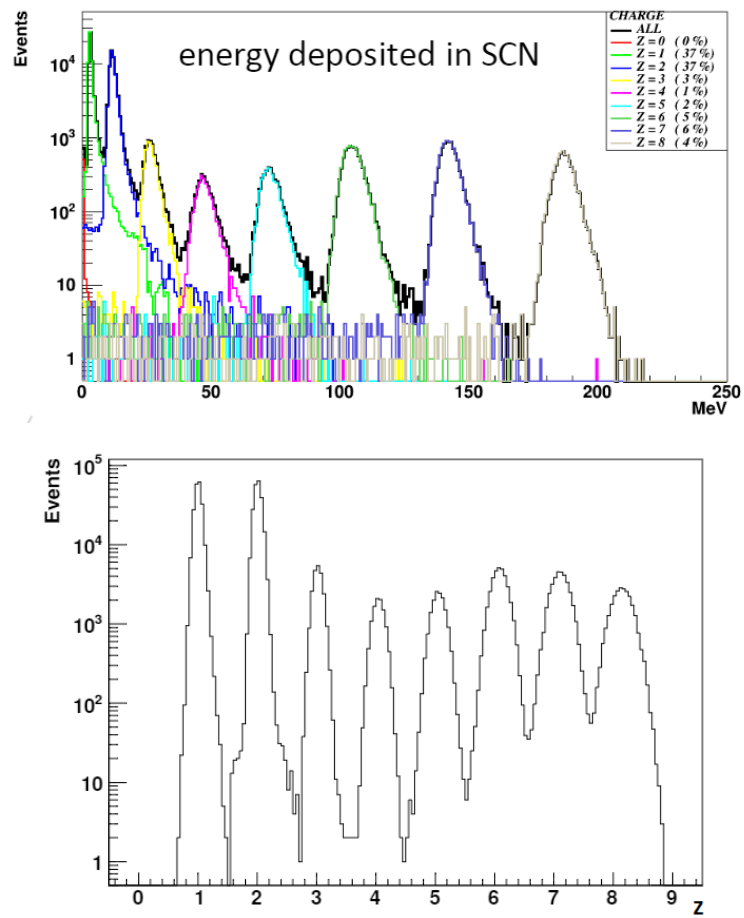


Figure 3.16: Charge number Z reconstruction for the studied fragments

- through  $\mathbf{p}$  and  $\mathbf{E}_{kin}$ :

$$E_{tot}^2 = p^2 + m^2 \Rightarrow (E_{kin} + m)^2 = p^2 + m^2$$

$$A_3 = \frac{m}{U} = \frac{p^2 - E_{kin}^2}{2UE_{kin}} \quad (3.6)$$

where the momentum  $p$  is the fitting result of the tracking system and  $E_{kin}$  is the kinetic energy measured by the calorimeter.

The three different methods for the determination of  $A$  exhibit an obvious correlation, because they use common detector measurements. In figure (3.17) it is shown, as an example, the distribution of the reconstruction of mass number  $A$  in the three models for Helium fragments. Table (3.2) summarizes the peak values and the resolution of the three models.

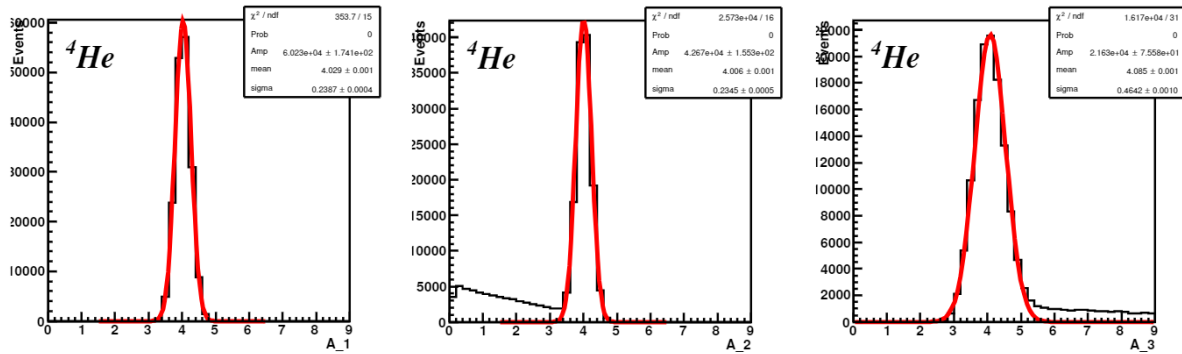


Figure 3.17: Determination of mass number  $A$  by three methods: TOF and tracking system (left), TOF and calorimeter (center), tracking system and calorimeter (right).

The other fragments distributions show similar behaviours. As can be seen from the graphics, some general remarks can be pointed out:

- the peak position is centred around the expected values and the possible shift is included in the resolution;
- $A_1$  and  $A_2$  reconstruction models show a  $\approx 5\%$  resolution, while  $A_3$  has a slight worse resolution  $\approx 10\%$ ;
- the calorimeter measurements suffer a significant tail of badly reconstructed mass number  $A$ , mainly due to the energy leakage of escaping neutrons; this can be seen in  $A_2$  and  $A_3$  distributions.

The approach for the determination of the mass number  $A$  follows two different fit methods:

- a **standard  $\chi^2$  minimization** approach;
- an **Augmented Lagrangian Method (ALM)** approach

The two fit methods bring similar results; the events which lead to a badly reconstructed  $A$  can be identified and excluded with a  $\chi^2$  cut (Figure 3.18 shows a  $\chi^2 < 5$  cut in both approaches), providing more precise results.

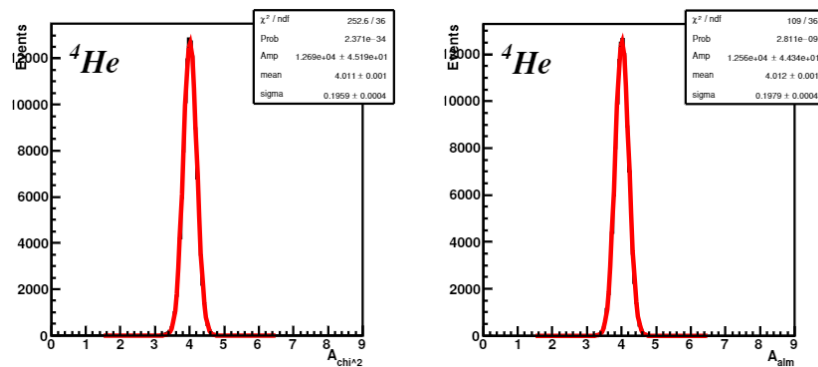


Figure 3.18: Determination of  $A$  with the standard  $\chi^2$  method (left) and augmented lagrangian method (right) applying a  $\chi^2 < 5$  cut.

Fragment	${}^4\text{He}$
$A_1$	$4.03 \pm 0.24$
$A_2$	$4.01 \pm 0.23$
$A_3$	$4.1 \pm 0.5$
$A_{\chi^2}$	$4.01 \pm 0.20$
$A_{ALM}$	$4.01 \pm 0.20$

Table 3.2: Peak value and resolution of the mass number  $A$  for Helium fragments; comparison between the values obtained with the three methods and the two fit with  $\chi^2$  cut applied.

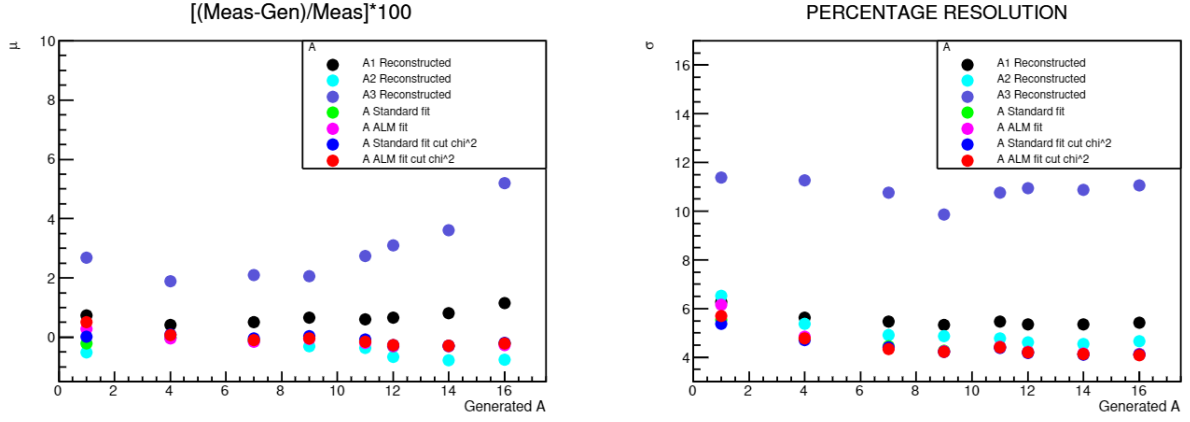


Figure 3.19: Percentage deviation on the left and resolution of A for each fragment with respect to the generated A on the right picture. Black, light blue and violet colours are respectively used for the  $A_1$ ,  $A_2$  and  $A_3$  reconstruction methods. The other colours are related to the two fit procedures, in particular: green and magenta represent respectively the standard  $\chi^2$  and ALM fit methods without any cuts, while dark blue and red are respectively used for the standard  $\chi^2$  and ALM methods adding the request  $\chi^2 < 5$ . The dark blue, red, green and magenta points frequently overlap.

In order to schematically visualize the performances of the different methods for A reconstruction, both the percentage of the resolution and the distribution of the variable  $(A_{meas} - A_{gen})/A_{meas} * 100$  (relative deviation of the measured quantity with respect to the reconstructed one) have been plotted in Figure (3.19).

The two fit methods including the  $\chi^2 < 5$  cut have the best resolution and comparable performance (overlapped in Fig. 3.19, right), with a resolution of  $\sim 5\%$  for lighter ions and  $\sim 4\%$  for heavier ions.

# Chapter 4

## Tracking

The fields of high energy physics accelerators, detectors and computing technologies have undergone a great development during the last decades. The desire to understand in more detail the basic behaviour of the fundamental constituents of nature and the interactions between these constituents has led to experimental studies carried out at ever increasing energies, with a rising number of particles created during the interactions. As a consequence, event patterns have become much more complex and data rates have highly increased in the course of time. The task of analyzing data from high-energy physics experiments has therefore, over the years, been performed in a continuously changing environment and analysis methods have evolved accordingly to adapt to these changes.

One of the crucial parts of the data-analysis chain in a particle physics experiment are the track reconstruction and vertex reconstruction. These tasks aim to determine the position, direction and momentum of the particles, and the location of their production points. In order to estimate as accurately as possible these kinetic parameters, a set of detecting devices providing high-precision and high granularity position measurements are located close to the beam collision target area.

Various species of particle detectors are generally used in combination with each other, in order to maximize the informations received. They can be classified in:

- Strip detectors deliver the position of particle passage along a well defined axis in the detector plane. Examples are silicon strip detectors or wire chambers.
- Pixel detectors deliver two dimensional information, that is the penetration point of a track through the detector plane. Examples are silicon detectors with a pixelized readout structure.
- Wire-based drift detectors deliver their wire position and a drift time.
- Time projection chambers measure three-dimensional space points along the particle trajectories.

Track reconstruction consists of two steps: track finding, which is the classification of hits in a track detector and track fitting, which fits the selected hits to a track model and determines its track parameters and the interaction point.

- Track finding is a pattern recognition or classification problem and aims at dividing the set of measurements in a tracking detector into subsets, each subset containing hits believed to originate from the same particle. These subsets are called *track candidates*.
- The track fit takes the set of measurements of a *track candidate* as a starting point; the aim of fitting is to compute both the best estimate of the track parameters and its covariance matrix (which provides a measure of the uncertainty of these values), checking whether the candidate is a valid hypothesis using a  $\chi^2$  test.

In a uniform magnetic field, a charged particle follows a helical trajectory; the most simple way to extract the track parameters is to perform a  $\chi^2$  fit assuming that the particle follows a perfect helix, ignoring multiple scattering and energy loss. When dealing with events where energy loss must be considered significant, a more powerful reconstruction algorithm is needed in order to have a better trajectory fit.

The goal of a track reconstruction algorithm is to estimate as accurately as possible a set of parameters describing the state of the particle at a reference surface in the tracking detector. The estimation is generally based on least-squares methods. The value of the  $\chi^2$  is the sum of the squared standardized differences between the measured positions in the track candidate and the estimated positions of the track at the points of intersection of the detector devices.

A recursive formulation of the least squares method, the Kalman filter, is a numerically stable and computationally fast algorithm, as it requires the inversion of only small matrices [34], [35]. Further details will be explained in the next paragraph.

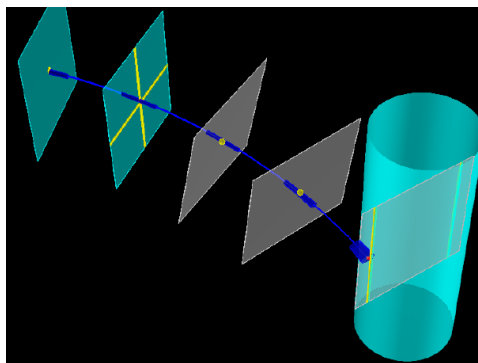


Figure 4.1: An example of Kalman filter track reconstruction. The measurements are yellow and the smoothed track is blue.

## 4.1 Kalman Filter

The extended Kalman filter is an efficient recursive algorithm that finds the best estimate for the state of dynamic systems from a series of noisy measurements.

The filter is named after Rudolf E. Kálmán (Fig. 4.2), one of the primary developers of this theory [36].



Figure 4.2: For its scientific work, U.S. President Barack Obama rewarded Kálmán with the National Medal of Science on October 7, 2009.

Since its development, Kalman filter algorithm has had numerous application in technology: a common application is for guidance, navigation, and control of vehicles, particularly aircraft and spacecraft. Kalman filters also are one of the main topics in the field of robotic motion planning and work for the modelling of the central nervous system movement control. Moreover Kalman filter algorithms have been applied to track fitting in high energy physics by many experiments [37].

The algorithm works in a two-step process: the *prediction step* and the *update step*. The state vector (or track parameter) of a charged particle in a magnetic field tied to a surface (detector layer) is described by a 5-dimensional column vector and so fully specified five parameters. The symbol  $\tilde{q}_k$  denotes the (of course always unknown) true value of the state vector in the plane of hit  $k$ . One step of the algorithm is defined as the inclusion of the measurement information of one more hit  $k$  into a state vector that already contains the information of all the hits up to  $k-1$ . Before the filter step, the state vector is given at the place of measurement of hit  $k-1$ . The predicted and filtered state vectors are denoted by  $q_{k|k-1}$  and  $q_{k|k}$ .

In the *prediction step*, the Kalman filter produces estimates of the current state variables, along with their uncertainties (Covariance Matrix). The prediction step propagates

the estimated track parameter  $q_{k-1|k-1}$  vector from detector layer ( $k-1$ ) to the next layer containing a measurement:

$$q_{k|k-1} = f_{k|k-1}(q_{k-1|k-1}) \quad (4.1)$$

where  $f_{k|k-1}$  is the track propagator from surface ( $k-1$ ) to surface  $k$  as well as the associated Covariance Matrix

$$C_{k|k-1} = F_{k|k-1}C_{k-1|k-1}F_{k|k-1}^T + Q_k \quad (4.2)$$

where  $F_{k|k-1}$  is the Jacobian matrix of the propagation from layer ( $k-1$ ) to  $k$ ,

$$F_{k|k-1} = \frac{\partial q_k}{\partial q_{k-1}} \quad (4.3)$$

and  $Q_k$  is a noise matrix which takes into account effects like multiple scattering and energy loss straggling.

Then, in the *update step*, these estimates are updated using a weighted average, via  $\chi^2$  minimization, between prediction and measurement, with more weight being given to estimates with higher certainty. The most crucial difference from the simple  $\chi^2$  fitting is that the track parameters are updated as new measurement points are added. Because of this we can take into account a step-by-step the evolution of the track parameters, yet accounting for multiple Coulomb scattering and energy loss through matter. Doing so, the algorithm updates the state vector and the covariance matrix such that the track comes closer to the actual hit than the predicted one did (Figure 4.3).

The updated state is

$$q_{k|k} = q_{k|k-1} + K_k[m_k - h_k(q_{k|k-1})], \quad (4.4)$$

where the measurement model  $h_k$  describes the functional dependence of the measured quantities in layer  $k$ ,  $m_k$  (vector of measurements), on the state vector at the same layer,  $m_k = h_k(q_k)$  and the gain matrix  $K_k$  is given by:

$$K_k = C_{k|k-1}H_k^T(V_k + H_kC_{k|k-1}H_k^T)^{-1} \quad (4.5)$$

where  $H_k$  is the Jacobian of the transformation,

$$H_k = \frac{\partial m_k}{\partial q_k} \quad (4.6)$$

and  $V_k$  is the covariance matrix of  $m_k$ .

The covariance matrix is updated by:

$$C_{k|k} = (I - K_kH_k)C_{k|k-1} \quad (4.7)$$

with  $I$  the identity matrix. The update step shrinks the covariance matrix because of the information contained in the measurement:

$$C_{k|k} < C_{k|k-1} \quad (4.8)$$

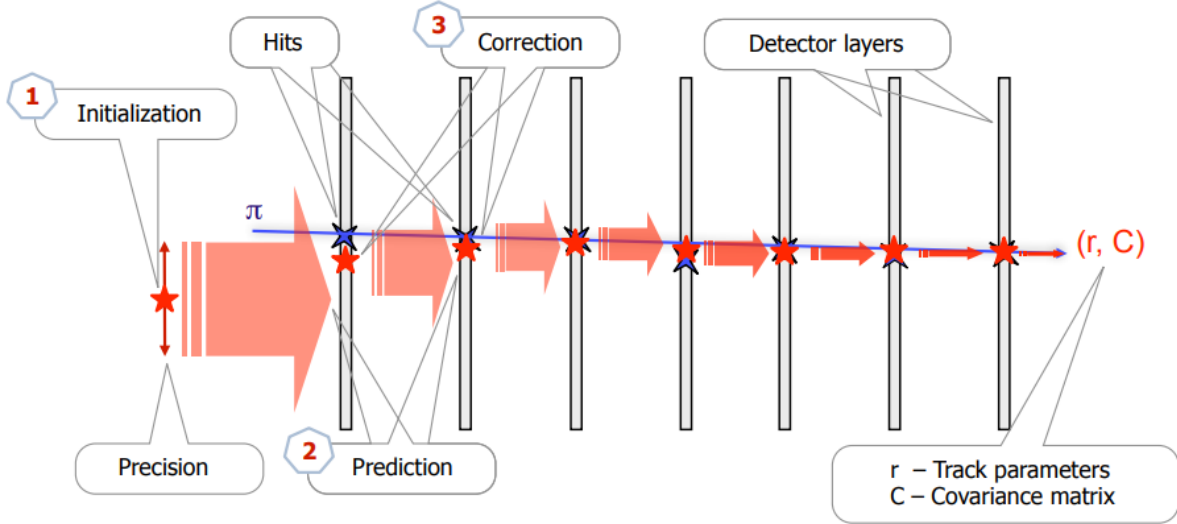


Figure 4.3: Graphic visualization of Kalman filter estimation of the track parameters at one or more hits along the track.

Accumulation of the measurement vectors improves the estimate of the state of the system: that's why a recurrence formula is needed. The algorithm is recursive and is iterate over all the selected measurements in each layer. After the Kalman filter has been performed on all hits of the track, the reconstruction can still be biased due to wrong starting values, named "seed". This error can be reduced by repeating the procedure backwards, with the iterative algorithm running in the opposite direction of the initial filter, using the previous fit results as starting values. The final "smoothed states" are the weighted mean of the previous predicted states and the updated states of the backwards filter.

The main goal of the FOOT experiment is to calculate the differential nuclear fragmentation cross section at precision level of 5%. The use of kalman filter based tracking algorithm gives the best possible tracking performances, as it allows a momentum resolution  $\frac{\sigma(p)}{p}$  at the level of 5%, enough to improve the isotope separation through the  $A$  measurement, fulfilling in this way the FOOT experiment physics goals.

## 4.2 GENFIT

GENFIT is an extensible, open source, track fitting toolkit that combines fitting algorithms, track representations, and hit geometries into a modular framework. It is suitable for a wide variety of experiments, as it works independently of the specific event topology, detector setup or magnetic field arrangement.

It is completely written in C++ and makes extensive use of object oriented design. It uses the C++ standard template library and the ROOT data analysis framework.

GENFIT has been developed in the framework of the PANDA experiment [38] in FAIR - Facility for Antiproton and Ion Research (Darmstadt, Germany), by J. Rauch and T. Schlüter, but it is now distributed as a stand-alone package [39] and has been adopted by different experiments (e.g. BELLE II, FOPI).

This software package has also been designed to handle various track models with different propagation mechanisms and track parametrizations. This flexibility is especially useful in the early phase of an experiment when different track reconstruction methods could be compared with each other, in order to sort out the best approach.

### 4.2.1 GENFIT Modular Design

The basic functionalities which are required for any procedure of track fitting are the extrapolation of tracks to the sensible layers of the detectors, and the calculation of the distances between hits and tracks, i.e. the residuals.

Track fitting in GENFIT is based on three pillars: measurements, track representations, and fitting algorithms [40].

**Reconstruction Hits** The object that represents a measurement from a detector used in a track fit is called a *reconstruction hit*. It contains the vector of the raw measurement coordinates and its corresponding covariance matrix.

Since particle tracking generally needs a combination of different kind of detectors, GENFIT comes with predefined measurement classes for various detector types, including planar detectors, drift chambers, and time projection chambers.

In order to better apply the fitting algorithm, all the measurement coordinates and covariance must be located on a specific plane; for this reason the toolkit provides functions to construct virtual detector planes. These are detector planes which are calculated dynamically for every extrapolation of a track to a hit, for measurements that do not belong to physical detector planes. They convert the hit information into a position measurement in a plane perpendicular to the track. This leads to a fit which minimizes the perpendicular distances of the track to the detector measurements, i.e. a  $\chi^2$  minimization.

As an example, for planar detectors, the detector plane is given by the detector geometry, whereas for wire and space-point measurements, virtual detector planes are

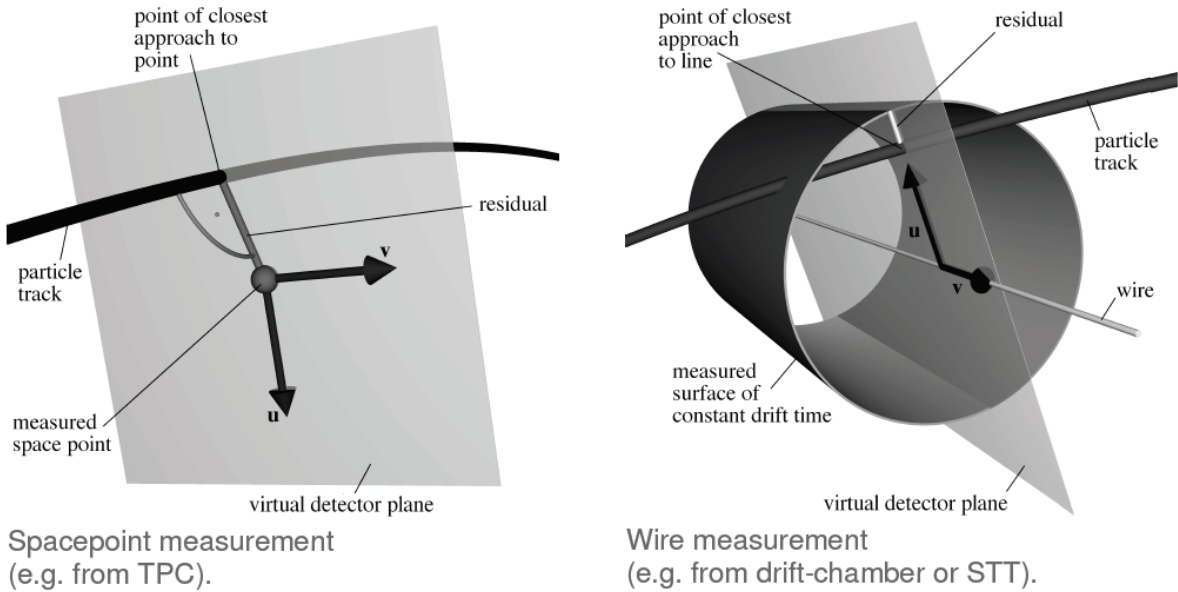


Figure 4.4: Virtual detector plane (spanning vectors  $\vec{u}$  and  $\vec{v}$ ) for a space-point hit (left) and a wire based drift detector hit (right).

constructed. For space-point detectors, the track fit has to minimize the perpendicular distances of the track to the hits. Therefore, the virtual detector plane for each hit must contain the hit position and the point of closest approach of the track to the hit point. Then the residual vector which points from the hit point to the point of closest approach will be perpendicular to the track. This geometry is illustrated in Figure (4.4); the orientation of the spanning vectors  $\vec{u}$  and  $\vec{v}$  is chosen arbitrarily in the plane.

**Track Representation** A particle track is described by a set of track parameters and a corresponding covariance matrix; a track representation contains also the data about the reference plane at which the parameters are defined.

The track of a charged particle in a magnetic field can be parametrized in many different ways. Parameters can be global (e.g. distance of closest approach to the z-axis, or azimuthal location of this point) or local (e.g. direction of the particle in a certain plane, or point of entry into a certain volume). In GENFIT, both global and local parametrizations can be used.

Track representations combine track parametrization and track extrapolation code; GENFIT implements a track representation based on a Runge-Kutta extrapolator.

All track representations in GENFIT must inherit from the abstract base class *GFAbsTrackRep*. A C++ class is called abstract if it contains at least one method which is declared as pure virtual and can not be instantiated. Derived classes must override

all pure virtual methods; this mechanism is called polymorphism and allows the algorithms to be independent from the specific nature and structure of the hits and track representations [41].

The GENFIT software package contains different track extrapolation functions which are needed for each track representation, some of which are: extrapolation to a plane, extrapolation to the point of closest approach (POCA) to a point, and extrapolation to the point of closest approach to a line.

The generic design of the track representation interface enables the user to use any external tracking code with GENFIT. The framework allows simultaneous fits of the same particle track with different track representations.

**Track Fitting Algorithms** GENFIT implements a variety of track-fitting algorithms, among which, two Kalman filters (one which linearizes the transport around the state predictions and one which linearizes around a reference track) and a deterministic annealing filter (DAF).

The extended Kalman filter is an iterative algorithm that produces an optimal estimate of a system state (with covariance) from a series of noisy measurements (extended dissertation in Section 4.1); nevertheless this particular algorithm can bring some problems due to the linearization around predictions. Especially for the first few hits, state predictions may stray very far from the actual trajectory; moreover outlier points can significantly bend the prediction away from the actual trajectory. The worst consequence can be the failure of the fit.

A possible solution is to take estimated track parameters from pattern recognition or previous fit as expansion point for linear approximation, which means linearize around reference track instead of state predictions. This procedure is carried out by the Kalman filter with reference track (Figure 4.5)

However, in case of outliers, the track fitting can be strongly biased. A robust algorithm that can be used in this case is the DAF (Deterministic Annealing Filter) which is able to reject outliers or to resolve left/right ambiguities of wire-measurement. The DAF is an iterative Kalman filter that assigns probabilities to each measurements (weights). By weighting and annealing, the DAF can reject outlying measurement and, doing so, it can find the best fit. An example is shown in Figure (4.6).

At present, the specific implementation in FOOT experiment uses the standard Kalman filter algorithm (Chapter 4.1); different studies are ongoing on the possible use of the DAF, which should be more powerful and appropriate in the presence of multiple background hits.

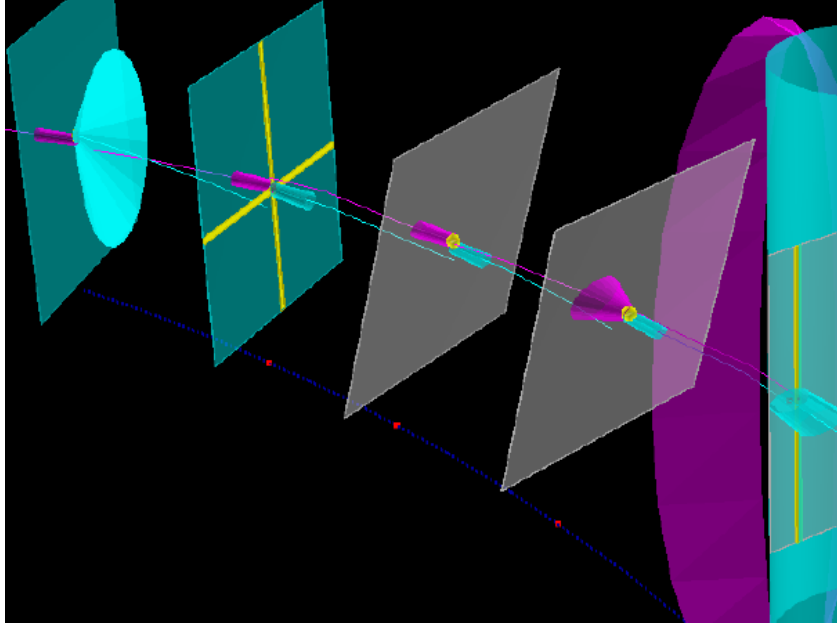


Figure 4.5: First iteration of Kalman filter tracking algorithm with reference track.

## 4.3 Software, SHOE

The software of FOOT plays a key role in the experiment by performing the reconstruction of the whole event from the raw data of the Monte Carlo simulations. In the first phase it has been used for the study of the best experimental setup by examining the simulation of different detector configurations and, in a second phase, it will perform the reconstruction on the real data, followed by the final cross section measurement. The FOOT software has been named SHOE, *Software for Hadrontherapy Optimization Experiment*, and is composed of two main units, the simulation framework and the reconstruction tool. The emulsion spectrometer setup, on the other hand, uses another reconstruction software that has been described elsewhere in literature [42], [43].

### 4.3.1 Simulation

The FOOT simulation is performed using the FLUKA software [44]. FLUKA is an advanced Monte Carlo simulation tool for the calculation of particle transport and interactions with matter, developed from the collaboration between INFN and CERN.

The FLUKA code has a wide range of applications, spanning from high energy experimental physics to cosmic rays study and medical physics, thanks to its ability to simulate with high accuracy the interaction and propagation through matter of about 60 different particles, with an energy range from keV to TeV. In particular, many later

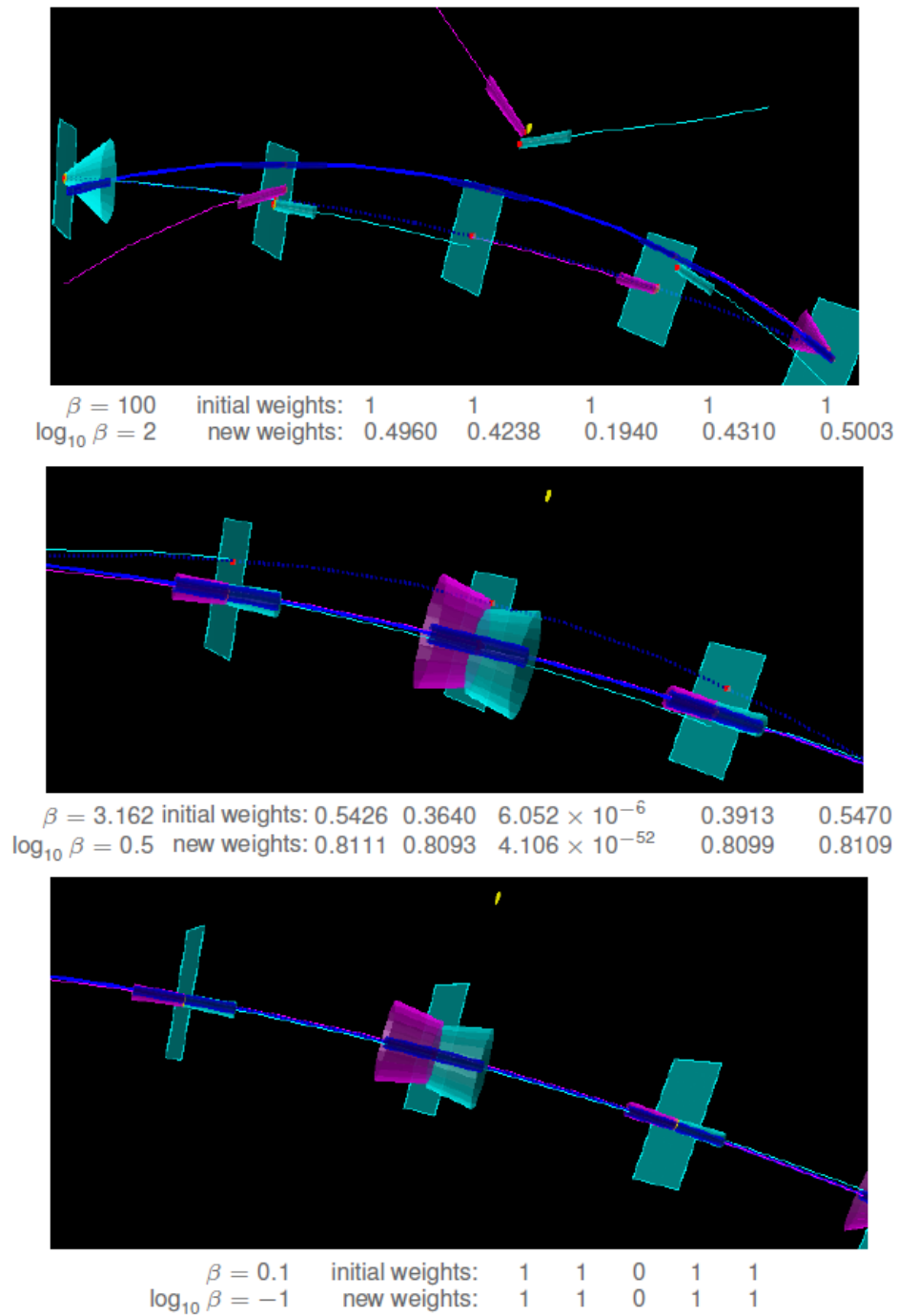


Figure 4.6: The figure shows three steps of the weighting procedure of the DAF. The proper weights are determined by the measurement of the residuals at every iteration. The final step shows the reject of the outlier point.

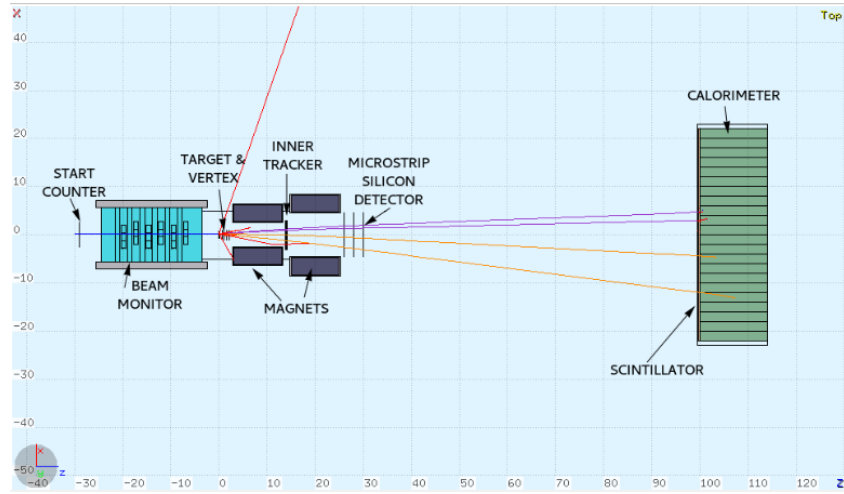


Figure 4.7: Schematic 2D event display of a primary  $^{16}\text{O}$  (blue) ion interacting with a polyethylene target. The colored lines represent the fragments produced.

FLUKA developments concerning both physics models and user interface, have been specifically adopted for its application in the context of hadrontherapy (FLUKA is used also at CNAO and HIT) [45]. Furthermore, FLUKA has recently been used for the simulation of experiments dedicated to fragmentation and to the study of secondary particles production with therapeutic beams [46].

This multipurpose code relies on the implementation and improvement of consolidated and modern physical models, which are fully integrated in the code and not modifiable.

An example of a simulated interaction of a primary beam of  $^{16}\text{O}$  ion with a polyethylene target is pictured in Figure (4.7), where a 2D scheme of the event displays the entire setup geometry and materials, which have been accurately implemented in the code.

In order to run the simulation, the starting point is to define all the informations necessary to the software for the processing of the data, thus the description of the setup and some physical specification, including them in the input and geometry files:

- **Physics Options:** predefined physics settings (for example production thresholds and transport energy cutoffs);
- **Beam characteristics:** source position, beam particle type, energy, spatial and/or momentum spread;
- **Geometry:** dimension and distances between the geometry regions (targets and detectors);
- **Materials:** materials and compounds compositions and properties and their assignment to different regions;

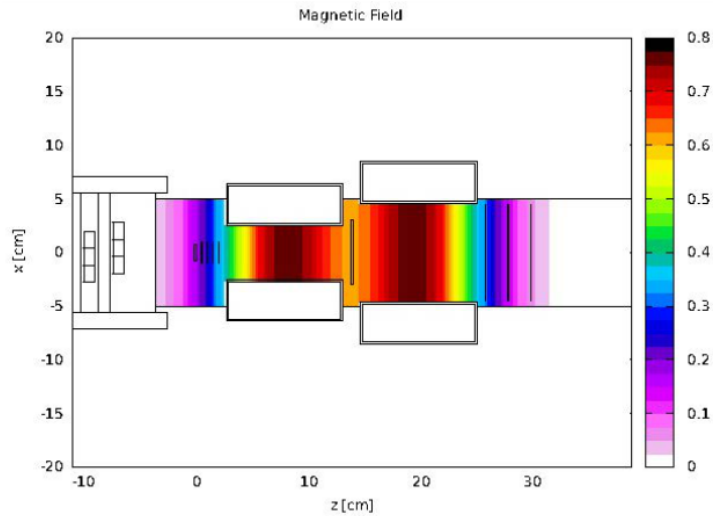


Figure 4.8: Representation of the magnetic field intensity read from a magnetic field map and integrated in the FOOT setup. The picture has been created from FLAIR, the FLUKA geoviewer.

- **Magnetic Field Description:** a 3D magnetic field map has been integrated in the simulation (Figure 4.8).

The output of the FOOT simulations is an ASCII file which stores event by event all the informations about the generated particles and their interaction with the detectors. In order to make the handling of the FLUKA output easier, the ASCII file is converted into a ROOT file and the data are stored in Tree Branches which can be easily interpreted by the reconstruction algorithm.

For a better management of the simulation software, the FLuka Advanced InteRface (FLAIR), a user friendly graphical interface, can be used [47].

### 4.3.2 Reconstruction

The event reconstruction involves the handling of the input and output data from the different detectors in order to obtain the identification of the fragments produced. In the FOOT experiment, the full reconstruction chain for both data and simulated events is performed by a ROOT based framework, developed in the GSI laboratory within the FIRST collaboration. The code uses a hierarchical structure to obtain a solid and simple object-oriented architecture.

In order to perform a full event reconstruction and analysis, the SHOE software performs two steps: the first step of the reconstruction code consists in reading, interpreting and converting in a single format both the data and the simulation events provided in

different input formats. Data are given in raw format by the DAQ system, like digitized signals, ascii and dat files; the simulation files are in ROOT n-tuple format. In the second step, events are processed in order to identify the track and extrapolate the needed information for the fragmentation studies and results. The reconstruction is performed by the GENFIT (Section 4.2) tracking tool and its Kalman algorithm. The structure of the SHOE reconstruction code is shown in Fig. (4.9) [48].

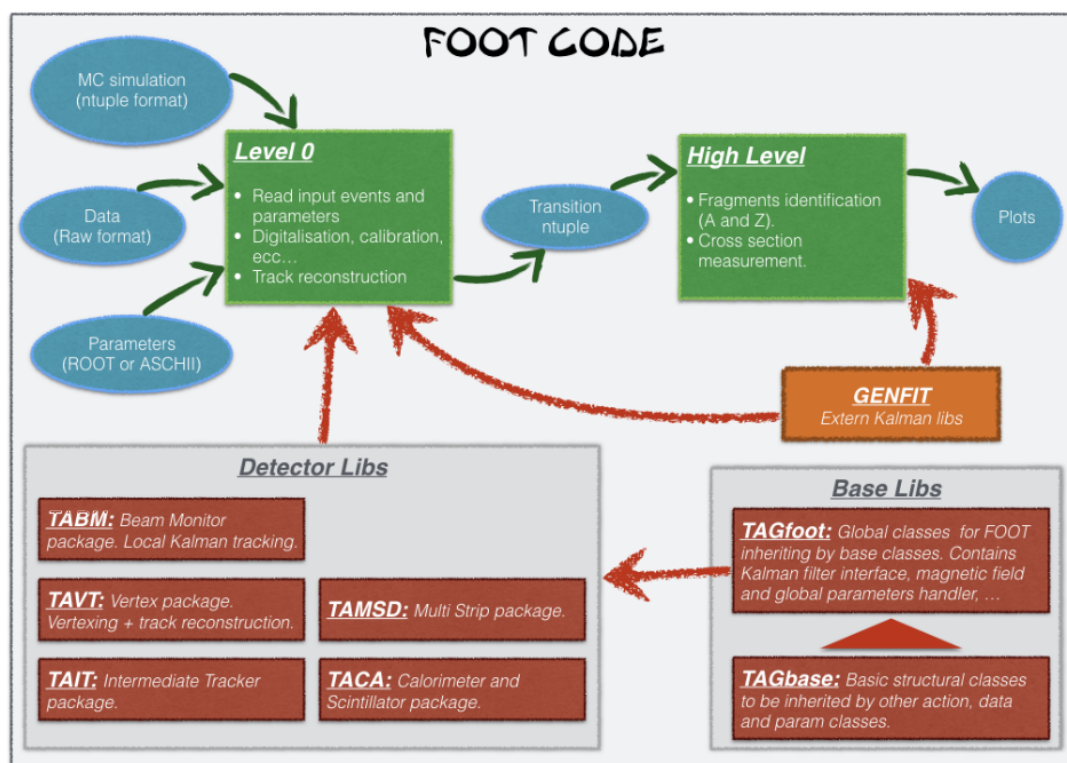


Figure 4.9: Diagram of the SHOE reconstruction code.

The framework is divided in three parts:

- **Libraries**

Libraries of general interest, containing the main classes used by the reconstruction code to generate the detector geometry. The GENFIT external libraries are also here.

- **Level 0**

Reconstruction code that is in charge of the interpretation of both Monte Carlo and acquired data, digitization, alignment and clustering of the events. In this part the track reconstruction with the Kalman Filter is performed. The signals

collected during the data acquisition runs are decoded, the detector dependent calibration constants are applied and the output of each detector is organized in "Hit", "Cluster" and "Track" objects.

- **High Level**

Reconstruction code deputed to the fragment identification and the cross sections measurement. The data obtained from the different sub-detector units (e.g. the Beam Monitor, the Tracking System, the Scintillator and the Calorimeter) are combined, achieving the final FOOT measurement: the different fragments are identified and their cross section estimated.

By structuring the reconstruction software in more layers, the computing resources are handled in a more efficient way. The track reconstruction provides two different tracks: one for the projectile, performed by the Beam Monitor hits, and one for the fragments, done combining hits from the Vertex, Inner Tracker and Micro Strip detectors.

## 4.4 Current Status of the Momentum Reconstruction

The reconstruction algorithm implemented in the SHOE software uses the standard Kalman filter. It presents a pattern recognition efficiency greater than 99% for all the fragments of interest. The comparison between generated (green) and standard Kalman Filter reconstructed (red) fragments momentum, using a 220, 350 and 700 MeV/u  $^{16}\text{O}$  projectile hitting a  $\text{C}_2\text{H}_4$  target is shown in Figure (4.10).

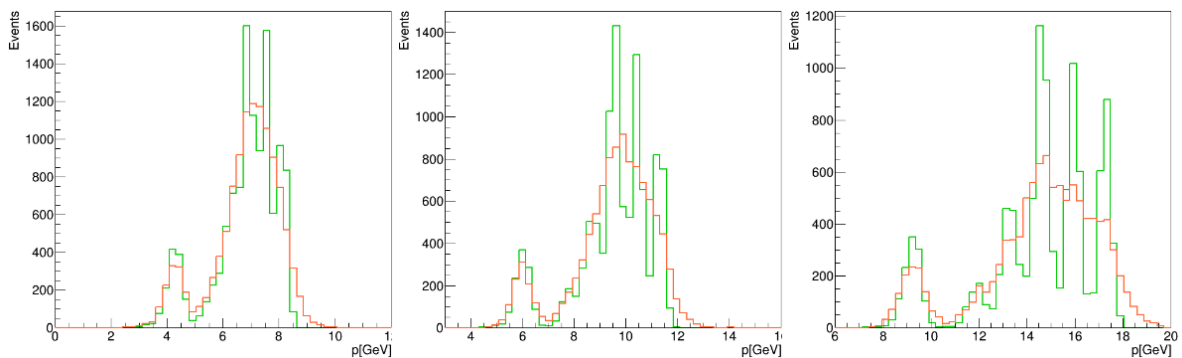


Figure 4.10: Generated (green) and reconstructed (red) momentum distribution of the considered fragments in each event for an Oxygen projectile of 200 MeV/nucleon (left), of 350 MeV/nucleon (center) and of 700 MeV/nucleon (right).

In the three samples the momentum distribution varies, broadening for higher energy values. All the distributions are characterised by several peaks, which correspond to the different produced fragments. Even though the reconstructed and generated results are quite in agreement and the distributions compatible, it can be clearly seen that the peaks are not perfectly reproduced by the reconstruction, in fact the red distributions present less distinguished peaks. The current resolution allows to disentangle only light fragments but not the heavier ones. The situation slightly improves in the case of sample with the  $^{16}\text{O}$  projectile at 700 MeV/nucleon.

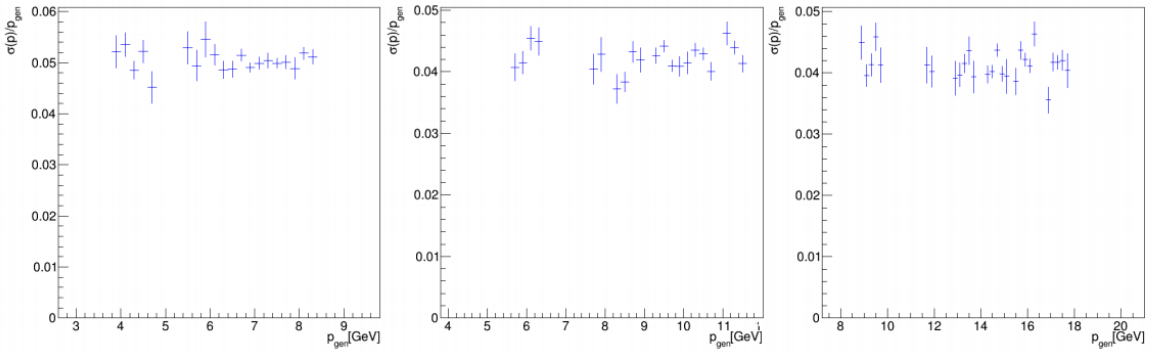


Figure 4.11: Differential momentum resolution as a function of the generated momentum for an Oxygen projectile of 200MeV/nucleon (left), of 350Mev/nucleon (center) and 700MeV/nucleon (right).

In order to estimate the relative momentum resolution  $\sigma(p)/p$ , the quantity  $(p_{gen}-p_{reco})/p_{gen}$  is plotted in 200 MeV wide bins of the fragment generated momentum and fitted using a Gaussian function (no background is expected). When, in a given bin, the statistics collected is not sufficient to measure the relative momentum resolution with an accuracy better than 10%, the bin is rejected. In Figure (4.11) it is presented the momentum resolution as a function of the Monte Carlo generated momentum, for 200, 350 and 700 MeV/nucleon Oxygen projectile. These preliminary data, show that the actual momentum resolution ranges from 4.5% to 5.5%, already not far from the goal of the experiment. At present, an optimization work is ongoing to further improve the obtained results. This work of thesis is born in this framework and it will focus on a more general study of the Kalman filter and its performances, testing its work by comparison with the Deterministic Annealing Filter.

## Chapter 5

# Kalman Filter Performance in FOOT

The main goal of the thesis is to study and test the performances of the Kalman Filter track reconstruction algorithms for what the requirements of the FOOT experiment concern. The final purpose is to obtain a momentum resolution of at least 5%, in order to perform a correct fragment identification. The current state of the art, presented in Section 4.4, estimates a momentum resolution that ranges from 4.5% to 5%. The results are preliminary data, to be further studied with better conformal testing.

As part of this upgrade study, this thesis presents a tracking reconstruction, which has been performed in a stand alone code by the GENFIT reconstruction toolkit. The events were randomly generated with the standard methods implemented in GENFIT.

The code works by generating hits (events), locating them on detector planes of previously assumed type and eventually performing a Kalman Filter reconstruction.

A minimal fitting example was implemented in order to better recreate the FOOT experiment configuration.

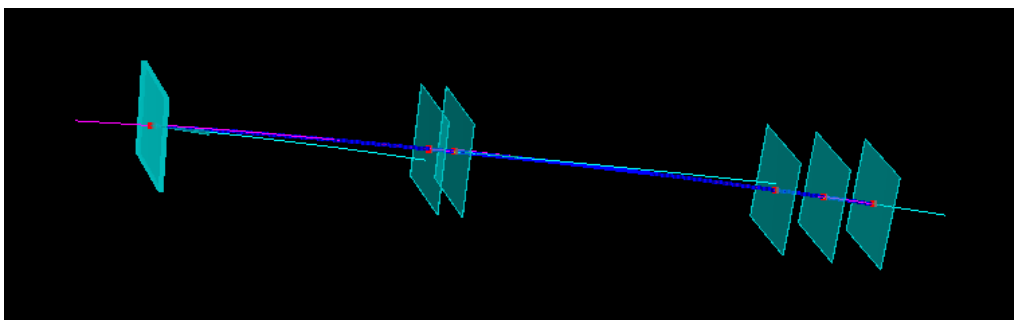


Figure 5.1: Event display of the simulation. The blue line represents the track reconstruction of the muon across the 9 planes of detectors. The first 4 layers represent the Vertex Tracker, which have a minimal spacing among them.

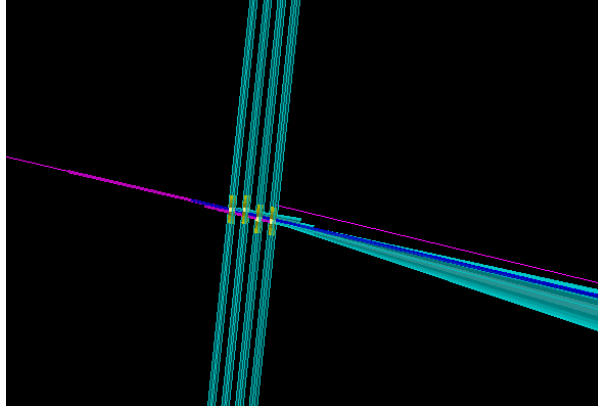


Figure 5.2: Zoom of the simulated Vertex Tracker. The four different layers can be better distinguished.

## 5.1 The Code

The code on which the reconstruction data were acquired is a stand alone example of track fitting, included in GENFIT toolkit. The program works by simulating a loop of 1000 events of a muon ( $\mu^-$ ) passing through various detectors. Even though muons are not particle of interest in the FOOT experiment, they can exemplify accurately the results. Unfortunately GENFIT does not contain the implementation of ions yet.

The generated tracks start from the origin (0,0,0) and have a simulated momentum module ranging from 0.2 to 1 GeV. The reason of this choice, is that a muon with a momentum of  $\sim 1$  GeV has a trajectory similar to the one of a  $\sim 10$  GeV proton. In one of the trials the energy range was changed for comparison in the two ranges 70-90 MeV / 0.7-1.3 GeV. The  $\varphi$  angle ranges from 0 to  $2\pi$ , while the  $\theta$  angle ranges from 0 to  $1/5\pi$ . The program then applies a gaussian smearing of the parameters, mimicking the case of a detector simulating the passage through a material. A detector resolution hypothesis, close to the actual FOOT one, is set to  $20 \mu\text{m}$  in  $x, y, z$ . The smeared position, momentum and the approximate covariance matrix are calculated. Then 9 hits per event are generated, one in each detector plane, all considered as pixel detector layers. The particle trajectory is helical, considered it crosses a magnetic field  $\vec{B}$ . Afterwards, the code creates a track reconstruction via Kalman filter.

Various parameters were modified in order to better recreate a setup similar to the one of the FOOT experiment. The magnetic field along  $z$  was set to 0.8 T. The distances between the detector planes in the magnet region were originally set to 5 cm, then changed to better recreate the actual distances between the active planes of the tracker in the magnetic region in FOOT (Figures 5.1, 5.2).

With this setup, a comparison between two different tracking algorithms, the standard Kalman Filter and the Deterministic Annealing Filter (DAF), was made.

## 5.2 Tests and Results

Different tries were made to compare the final results:

- **muKFDAF:** Track reconstruction for muons performed with the two reconstruction filters: the standard Kalman and the DAF.

As seen in Figure (5.3), the two  $\chi^2$  distributions are appreciably identical: the reconstruction has been performed excellently in both cases.

In Figure (5.4), the histograms of the three space components are well peaked. The worst resolution is along the  $z$  axis.

Even though the  $z$  component of the position is less peaked, it is visible in Figure (5.5) how the resolution along all the three components is uniform.

Figure (5.6) shows how the reconstructed momentum is in agreement with the generated momentum, which values were created with a smearing in polar coordinates. As expected, the histograms of the difference between the generated and reconstructed momentum is peaked in 0, so no global bias is present. The standard deviation is  $\sim 6\%$ . The two methods are compatible both in their mean value and in their standard deviation.

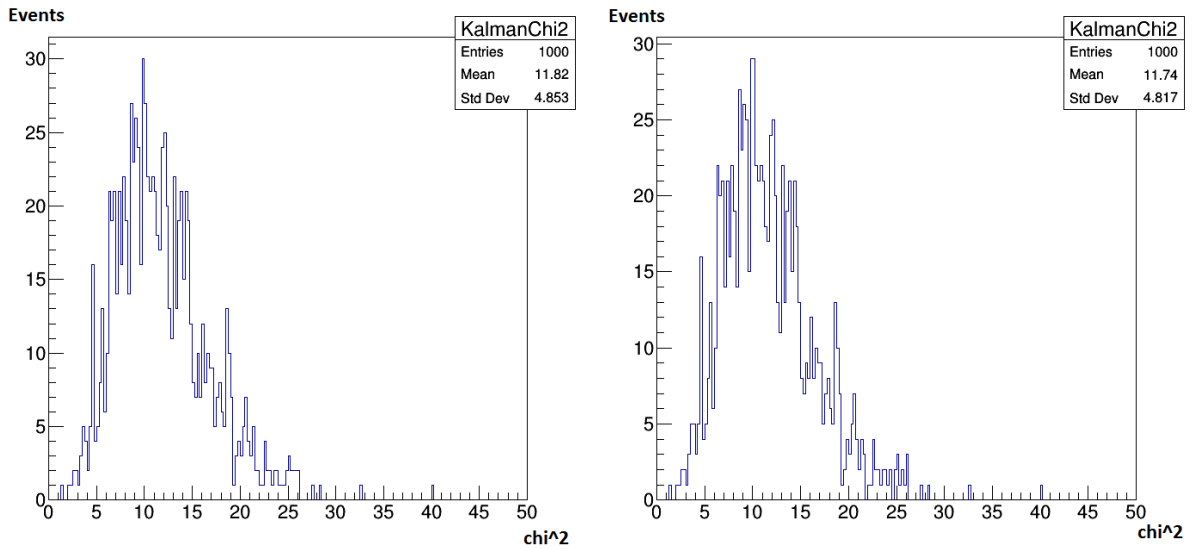


Figure 5.3:  $\chi^2$  histogram distributions of the track reconstruction for muons performed on the right with the Kalman filter and on the left with the DAF. The degrees of freedom are 13.

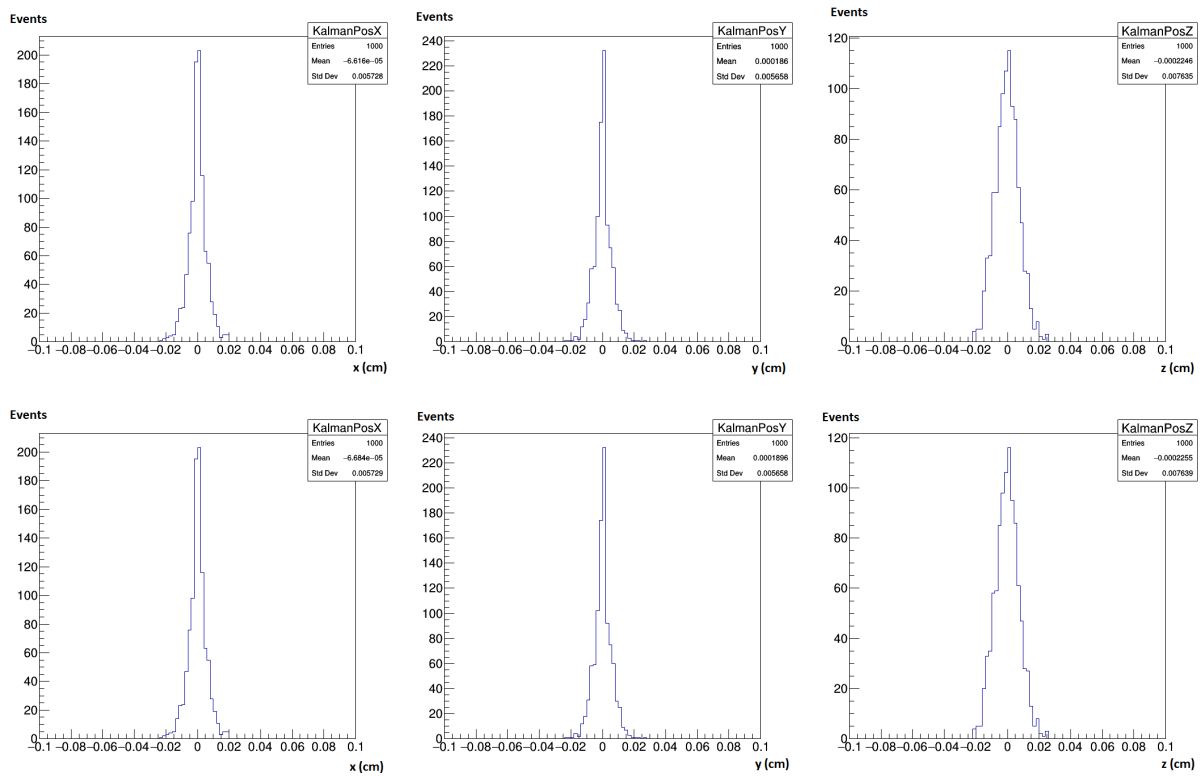


Figure 5.4: Histograms of the three position components for the muons; the track reconstruction is performed with the Kalman filter (top) and with the Deterministic Annealing Filter (bottom).

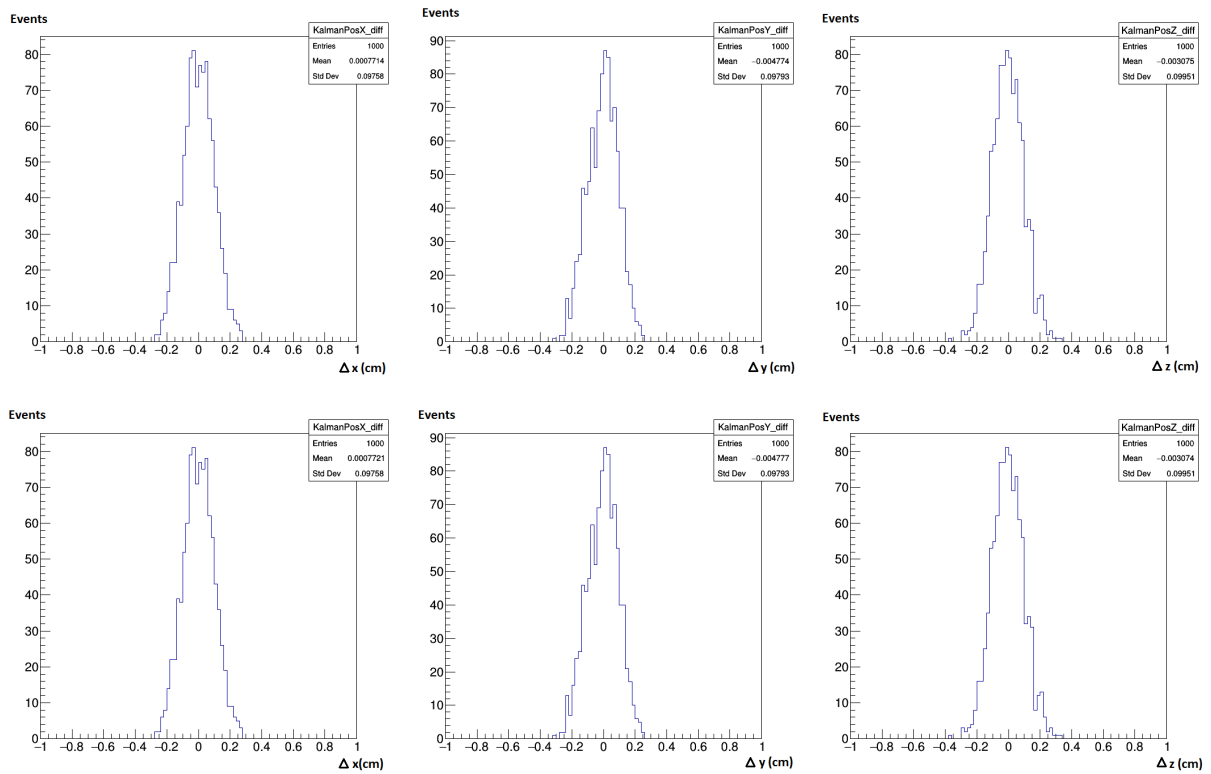


Figure 5.5: Histograms of the differences between the stated and estimated position components for the muons; the track reconstruction is performed with the Kalman filter (top) and the DAF (bottom).

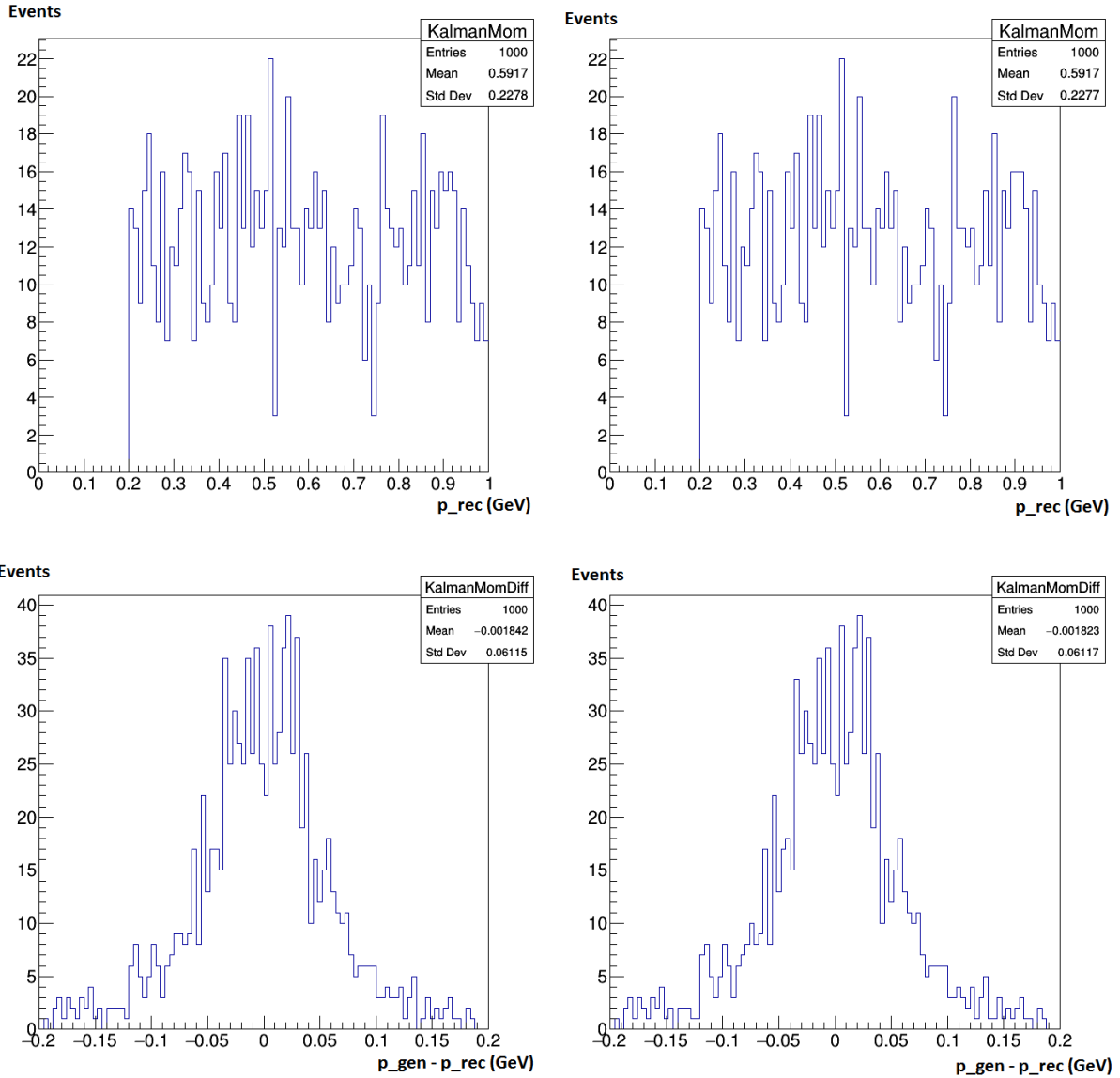


Figure 5.6: Histogram distributions of the momentum (top) and its uncertainty (bottom) for the KF (left) and the DAF (right). The momentum was uniformly generated in the range 0.2-1 GeV.

- **KFDAFdist:** track reconstruction for muons performed using detector layers with distances like in the FOOT experiment; comparison between the two reconstruction filters: the standard Kalman and the DAF.

Even in the case which considers the true distances between the tracker layers of the magnetic spectrometer in FOOT, the two  $\chi^2$  distributions are appreciably identical (Figure 5.7).

In Figure (5.8), the reconstructed momentum is in agreement with the generated momentum, which values were created with a smearing in polar coordinates and range from 200 MeV to 1 GeV. As expected, the histograms of the difference between the generated and reconstructed momentum is peaked in 0, so no global bias is present. The standard deviation is  $\sim 6\%$ . The two methods are compatible.

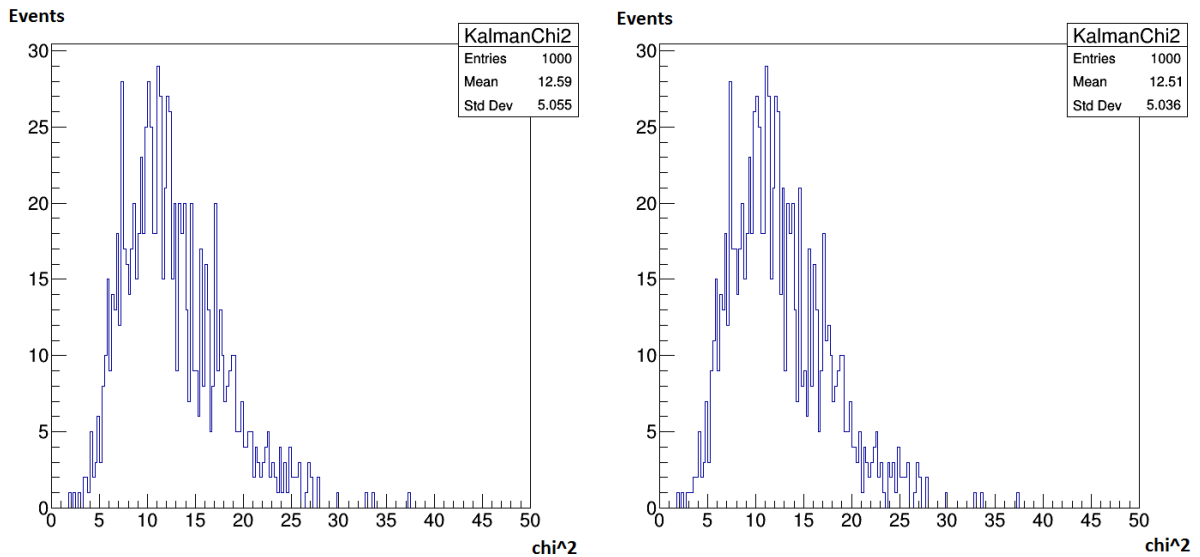


Figure 5.7:  $\chi^2$  histogram distributions of the track reconstruction performed with the KF and the DAF. The distances between layers are set like those in the FOOT experiment.

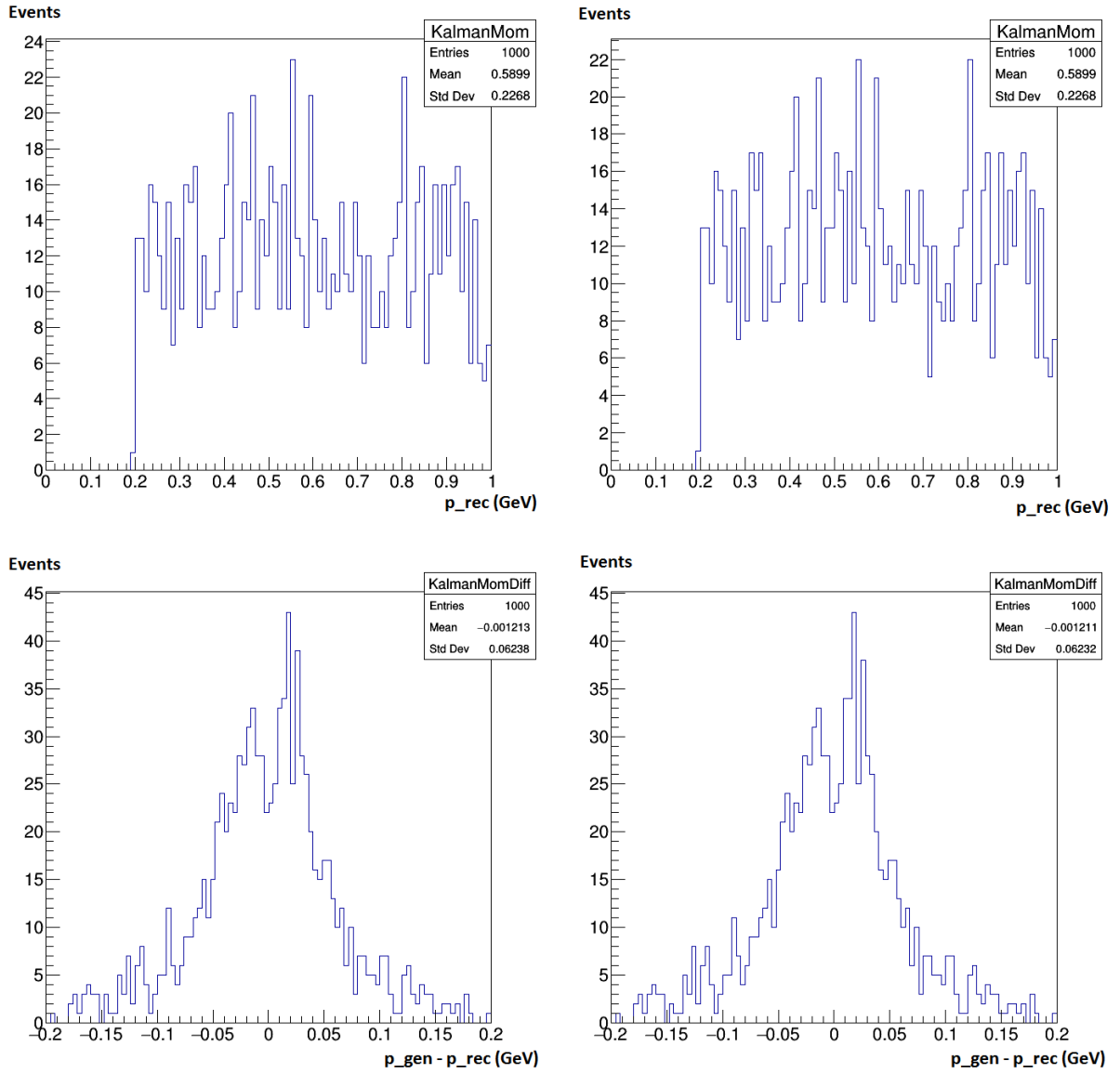


Figure 5.8: Histogram distributions of the momentum (top) and its uncertainty (bottom) for the KF (left) and the DAF (right) in the simulation with true distances.

- **KFDAFrangle:** comparison between the Kalman filter and the DAF for muons ( $\mu$ ). This time the track reconstruction is performed in two energies range: one goes from 70 MeV to 90 MeV, the other from 700 MeV to 1.3 GeV. The reason of this choice is to investigate if there is some change in the function implemented in GENFIT for the energy loss simulation through a medium, for particles with energy values before and after the MIP point.

As seen in Figure (5.9), the two  $\chi^2$  distributions for the first range of energies and those for the second range are appreciably similar. The reason of the difference between the peak values in the two energy ranges is that the  $\chi^2$  distribution for 700 MeV - 1.3 GeV broadens, as the bend radius for particles at higher energies is smaller and so the reconstruction is worse. Modifying the parameters, the  $\chi^2$  varies, but it remains similar for the two reconstruction filters.

For what the momentum reconstruction concerns, the two filters show similar results. In the 70 MeV - 90 MeV range case, the reconstructed momentum is in good agreement with the generated one: the histograms of the difference are peaked in 0 and present no bias (Figure 5.10).

In the 700 MeV - 1.3 GeV range case, the histograms are clearly broadened. The two reconstruction filters (Kalman filter and DAF) are in good agreement (Figure 5.11).

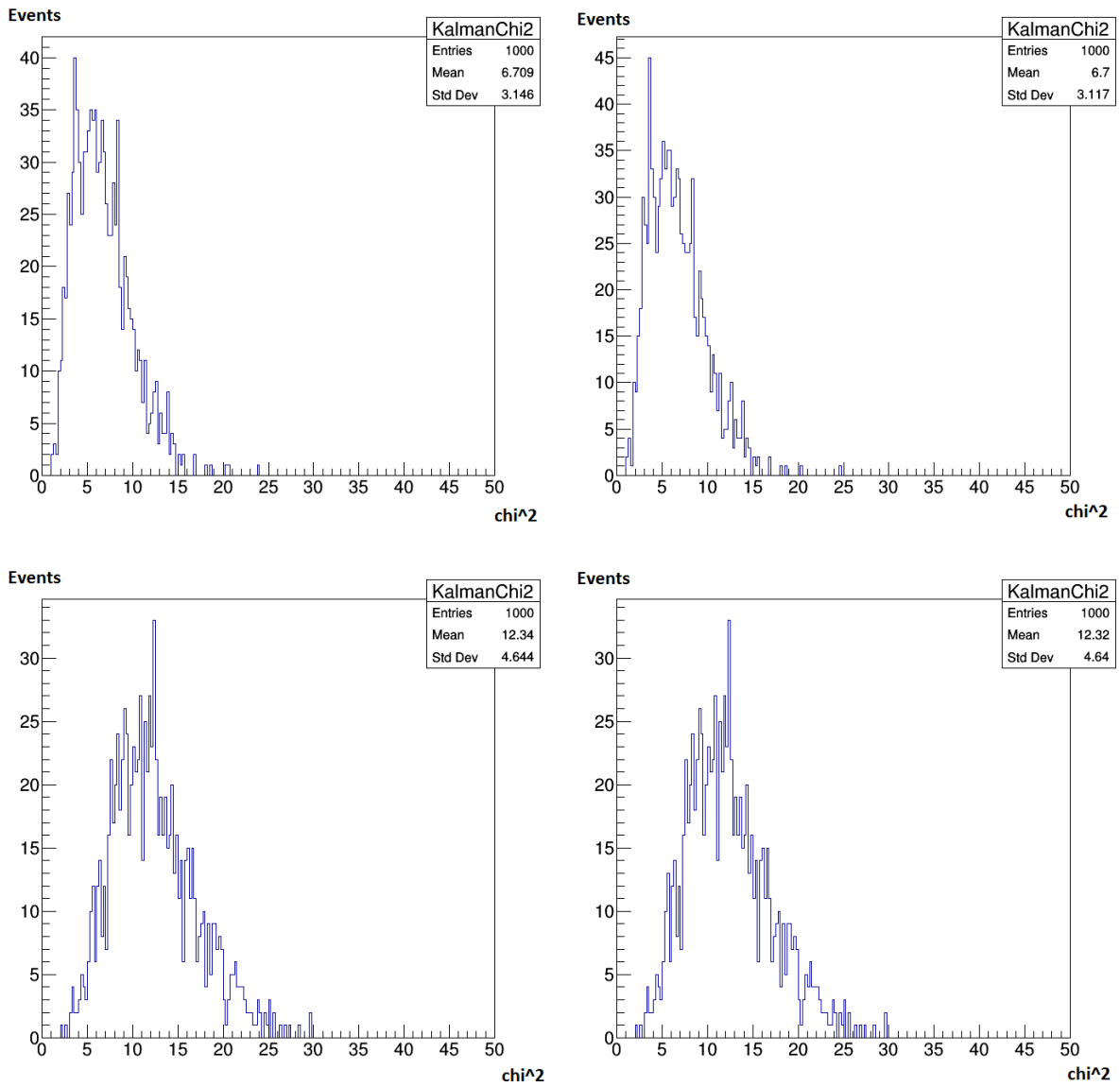


Figure 5.9:  $\chi^2$  histogram distributions of the track reconstruction performed with the KF (left) and the DAF (right). The range 70 MeV - 90 MeV is the top row, the range 700 MeV - 1.3 GeV is bottom.

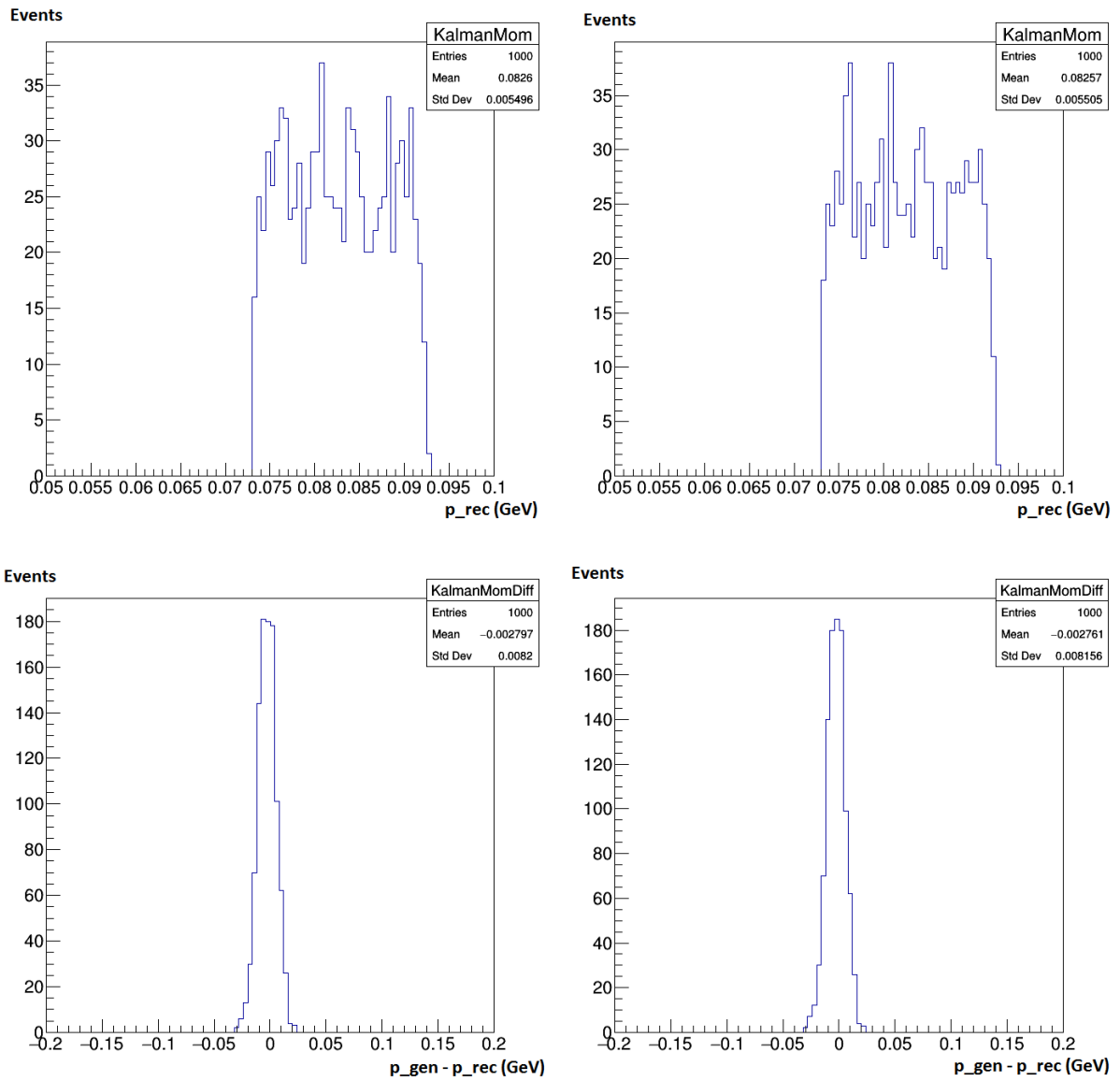


Figure 5.10: Histogram distributions of the momentum (top) and its uncertainty (bottom) for the KF (left) and the DAF (right) in the simulation with energy range from 70 MeV to 90 MeV.

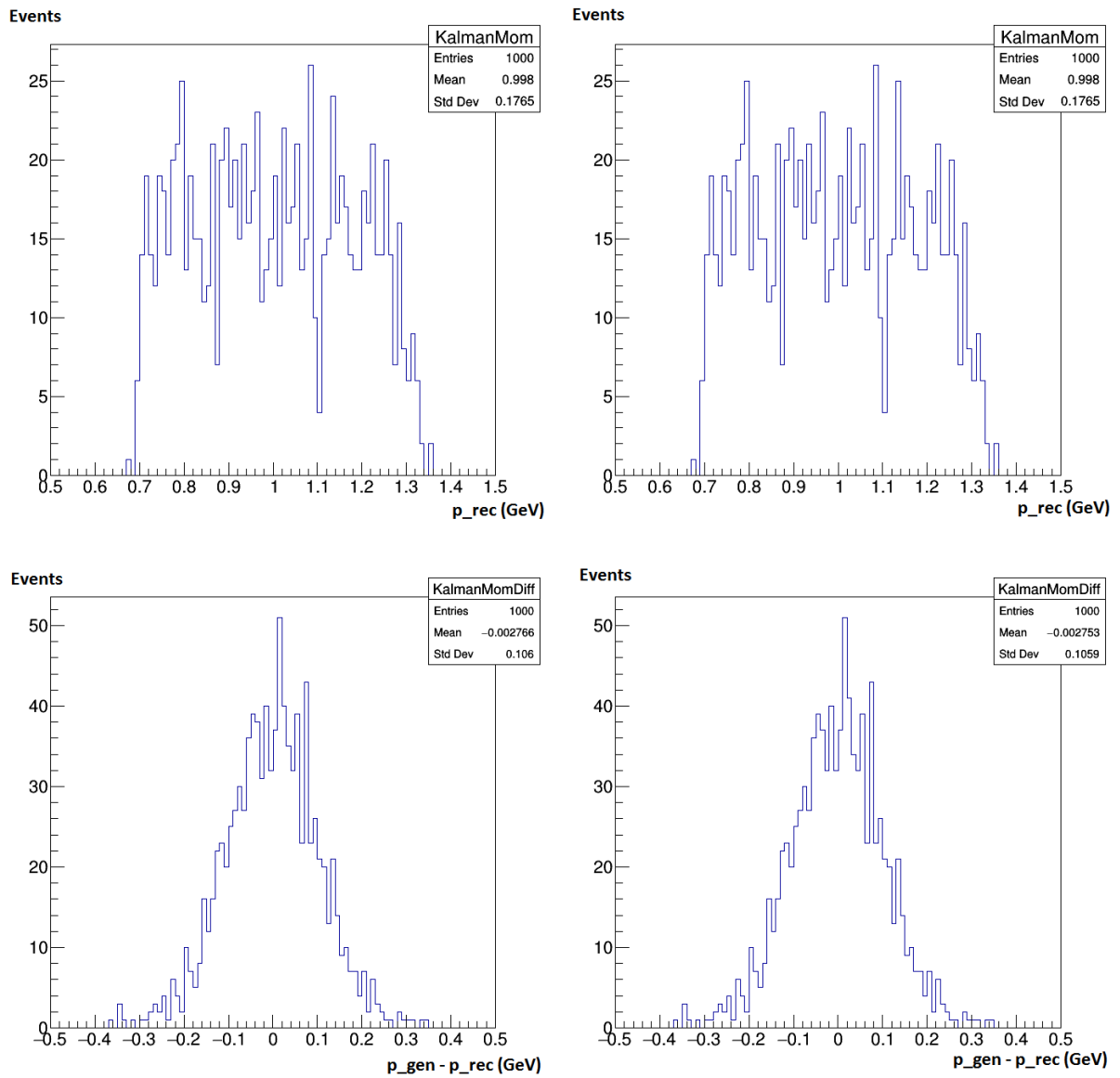


Figure 5.11: Histogram distributions of the momentum (top) and its uncertainty (bottom) for the KF (left) and the DAF (right) in the simulation with energy range from 700 MeV to 1.3 GeV.

The three tests were made to verify the effectiveness of the two filters in standard conditions, with well known data. It can be seen from the results presented that both the Kalman filter and the Deterministic Annealing Filter (DAF) have similar efficiency. Considering that the DAF is a filter that works best in rejecting outliers and background, it is clear that the results must be compatible with those of the Kalman filter, as the background is not simulated in the GENFIT code used.

The mean values of the  $\chi^2$  are compatible, as in the "KFDAFrage" test the two values (12.34 - 12.32) differ only of  $\sim 2\%$ . For what the momentum reconstruction concerns, the gaussian distributions of the  $\Delta p$  are centred in 0 with no bias and have a standard deviation of  $\sim 0.06$  for the "KFDAFdist" trial, for both reconstruction filters. Modifying the parameters (distances, energies), the  $\chi^2$  distributions vary, but remain coherent comparing the Kalman Filter and the DAF. This, ultimately verifies the stability of both methods.

### 5.3 Perspectives

The results achieved in the present work have shown that both the Kalman Filter and the Deterministic Annealing Filter are stable and valid methods of track reconstruction.

The future steps for enhancing the code in order to perform a tracking reconstruction which better mimics the FOOT experiment framework will be:

- adding an implementation in GENFIT for the recognition of heavy ions, currently missing;
- implementing the DAF in the official reconstruction code, to test it in a more realistic environment;
- adding the background events in order to estimate the Kalman Filter efficiency in a noise condition.

# Conclusions

This thesis has presented the principles behind the hadrontherapy, using protons and ion beams, the FOOT experiment and the techniques used in track reconstruction.

Nowadays charged particles are used to treat deep sited tumors, due to both the high localization of their dose release and the sparing of organs at risk surrounding the tumor volume. Therapies with ion beams still suffer from the uncertainties related to the probability of nuclear fragmentation processes. The study of the related nuclear cross sections is the main subject of the FOOT experiment, developed in particular to investigate the Carbon and Oxygen fragmentation when they are used as ion beams in the 200-700 MeV/u kinetic energy range.

NASA and other space agencies have started since several years the study of health risk assessment for astronauts during long lasting space exploration journeys. The measurement performed by the FOOT experiment could be crucial for the design and optimization of spacecraft shielding and for a better understanding of radiation induced damage.

To measure the cross section, an accurate reconstruction of the signals acquired by the FOOT detector has been developed. One of its fundamental elements is the tracking algorithm which has the role to identify the tracks in the detector and provide the best measurement of their impulse (modulus and direction) at the production point. The chosen algorithm is the implementation of a Kalman tracking, called GENFIT, for its generality and effectiveness. By using the three tracking stations foreseen in the FOOT experiment, one near the target, one in the magnetic field region and one behind it, it has been possible to identify fragment tracks, tracing them on all the detectors and extracting the main track parameters. Studies have shown that the experiment allows a momentum resolution  $\frac{\sigma(p)}{p}$  at the level of 5%, enough to evaluate the differential nuclear fragmentation cross section with an uncertainty of less than 5%. In particular, the preliminary momentum resolution ranges from 4.5% to 5% for beams of Oxygen ions for energies of 200, 350 and 700 MeV/u. In this way, the resolutions are already not far from the goal values of the FOOT experiment, permitting the correct fragments identification.

The results achieved in the present work of thesis have shown that both the Kalman Filter and the Deterministic Annealing Filter are stable and valid methods of track reconstruction. The next steps will be implementing the DAF in the SHOE software and, in order to test the reconstruction in a more realistic environment, a code for the recognition of heavy ions will be included, as well as a code that simulates background noise events.

For what the timescale of the experiment is concerned, it is foreseen to have a complete detector in 2019 and the first data taking will take place in late 2019 or early 2020. By that time an optimized reconstruction program will be available. For the study of fragmentation in particle therapy, the beam types for the FOOT data taking are  $^{12}\text{C}$  and  $^{16}\text{O}$ . Additional research programs may be pursued with  $^4\text{He}$ ,  $^{12}\text{C}$  and  $^{16}\text{O}$  with energies up to 800 MeV/u for radioprotection in space. The measurements performed by the FOOT experiment will be crucial in contributing to a better radiobiological characterization of protons and heavy ions used in hadrotherapeutic treatments and in driving forward the study for the design and optimization of spacecraft and space crew shielding.



# Bibliography

- [1] W. R. Leo, *Techniques for Nuclear and Particle Physics Experiments*, Berlin: Springer, 1987.
- [2] H. Bethe and J. Ashkin, *Passage of radiations through matter*, Experimental Nuclear Physics, vol. 1, 1953.
- [3] G. Knoll, *Radiation Detection and Measurement*, John Wiley and Sons Inc., 1999.
- [4] J. D. Bowman, W. J. Swiatecki, and C. F. Tsang, *Abrasion and Ablation of Heavy Ions* (unpublished), LBL Report No LBL-2908 University of California, 1973.
- [5] M. Durante and H. Paganetti, *Nuclear Physics in Particle Therapy: a review*, Reports on Progress in Physics, 79, p 59, 2016.
- [6] R. Serber, *Nuclear reactions at high energies*, Physical review, vol 72, p 1114–1115, 1947.
- [7] International Commission on Radiation Units & Measurements (ICRU), *Quantities and units in radiation protection dosimetry*, Report 51, 1993.
- [8] D. Schardt, T. Elässer, D. Schulz-Ertner, *Heavy-ion tumor therapy: Physical and radiobiological benefits*, Review of Modern Physics, vol 82, p 383425, 2010.
- [9] *WHO Cancer fact sheet 2017*, <http://www.who.int/mediacentre/factsheets/fs297/en/>
- [10] D.K. Ebner et al, *The immunoregulatory potential of particle radiation in cancer treatment*, Frontiers in Immunology, 8(99), 2017.
- [11] I. Mattei, *A novel on line dose monitoring technique tailored for particle therapy applications*, PhD in Physics Thesis, University Roma Tre, 2015.
- [12] U. Amaldi, *Particle accelerators: from Big Bang Physics to Hadron Therapy*, Springer, 2015.

- [13] R. R. Wilson, *Radiological use of fast protons*, *Radiology*, vol 47(5),487–491, 1946.
- [14] C. A. Tobias, *Radiological physics characteristics of the extracted heavy ion beams of the bevatron*, *Science*, 174: 1131-1134, 1971.
- [15] , *CNAO Centro nazionale di adroterapia oncologica per il trattamento dei tumori*. Available online: <http://www.cnao.it>
- [16] *Particle Therapy Co-Operative Group*, <https://www.ptcog.ch/>
- [17] *PTCOG: Statistics of patients treated in particle therapy facilities worldwide*, <https://www.ptcog.ch/index.php/ptcog-patient-statistics>
- [18] C. S. Chung et al, *Incidence of Second Malignancies Among Patients Treated With Proton Versus Photon Radiation*, *International Journal of Radiation Oncology*, 87, p 46-52, 2013.
- [19] H. Paganetti, *Relative Biological Effectiveness (RBE) values for proton beam therapy. Variations as a function of biological endpoint dose and linear energy transfer*, *Physics in Medicine and Biology*, vol 59, n 22, p R419, 2014.
- [20] F. Tommasino, M. Durante, *Proton Radiobiology*, *Cancers*, 2015.
- [21] F. Tommasino et al, *New Ions for Therapy*, *International Journal of Particle Therapy*, vol 2, p 428–438, 2015.
- [22] M. Marafini et al., *The INSIDE Project: Innovative Solutions for In-Beam Dosimetry in Hadrontherapy*, *Acta Physica Polonica A*, Vol. 127, p 1475, 2015.
- [23] M. Durante, F. A. Cucinotta, *Physical Basis of Radiation Protection Space Travel*, *Review of Modern Physics*, 83, 1245, 2011.
- [24] *NASA*, [https://www.nasa.gov/about/whats\\_next.html](https://www.nasa.gov/about/whats_next.html)
- [25] M. Cerri et al., *Hibernation for space travel: Impact on radioprotection*, *Life Sciences in Space Research*, vol 11, p 1–9, 2016.
- [26] R. E. McGuire, T. T. Von Rosenvinge, F. B. McDonald, *The composition of solar energetic particles*, *Astrophysical Journal*, vol. 301, p 938–961, 1986.
- [27] J. Dudouet et al., *Double-differential fragmentation cross-section measurements of 95 MeV/nucleon  $^{12}\text{C}$  beams on thin targets for hadron therapy*, *Physical Review C*, vol 88, p 024606, 2013.
- [28] M. Toppi et al, *Measurements of fragmentation cross section of  $^{12}\text{C}$  ions on thin gold target with the FIRST apparatus*, *Physical Review C*, vol 93, n 6, p 064601, 2016.

- [29] G. De Lellis et al., *Nuclear emulsions*, Elementary Particles: Detectors for Particles and Radiation, vol 21B, Springer, 2011.
- [30] G. De Lellis, S. Buontempo, *Emulsion Cloud Chamber technique to measure the fragmentation of a high-energy carbon beam*, J. Instrum, vol 2, p P06004, 2007.
- [31] National Institute of Standards and Technology, <https://www.nist.gov/>
- [32] M. De Serio et al., *Momentum measurement by the angular method in the Emulsion Cloud Chamber*, Nuclear Instruments and Methods in Physics A, vol 512, p 539-545, 2003.
- [33] J. Rauch and T. Schlüterb, *Genfit a generic track-fitting toolkit*, Journal of Physics, 608, 2015.
- [34] A. Strandlie, R. Frühwirth, *Track and Vertex Reconstruction: From Classical to Adaptive Methods*, Reviews of Modern Physics, vol 82, p 1419, 2010.
- [35] K. Fujii, *Extended Kalman Filter*, Reference Manual, 2013.
- [36] R. E. Kálmán, *A new approach to linear filtering and prediction problems*, Journal of Basic Engineering, 1960.
- [37] R. Frühwirth, *Application of Kalman filtering to track and vertex fitting*, Nuclear Instruments and Methods in Physics Research, Section A, p 444–450, 1987.
- [38] The PANDA Collaboration, *Physics performance report for PANDA: strong interaction studies with antiprotons*, arXiv:0903.3905 [hep-ex], 2009.
- [39] GENFIT, <http://sourceforge.net/projects/genfit>
- [40] C. Höppner, S. Neubert et al., *A novel generic framework for track fitting in complex detector systems*, Nuclear Instruments and Methods in Physics, Research A, vol 620, p 518–525, 2010.
- [41] C. Höppner, S. Neubert et al., *GENFIT: a Generic Track Reconstruction Toolkit*, v1.2 memo, 2009.
- [42] A. Alexandrov et al., *A new generation scanning system for the high-speed analysis of nuclear emulsions*, J. Instrum, vol 11, p P06002, 2016.
- [43] A. Alexandrov et al., *The continuous motion technique for the new generation scanning system*, J. Instrum, n 7310, 2017.
- [44] FLUKA, <http://www.fluka.org/fluka.php>

- [45] G. Battistoni et al., *The FLUKA code: an accurate simulation tool for Particle Therapy*, *Frontiers in Oncology*, vol 6, p 116, 2016.
- [46] I. Mattei et al., *Secondary radiation measurements for particle therapy applications: prompt photons produced by  $^4\text{He}$   $^{12}\text{C}$  and  $^{16}\text{O}$  ion beams in a PMMA target*, *Physics in Medicine and Biology*, vol 62, n 4, p. 1438, 2017.
- [47] V. Vlachoudis et al., *FLAIR: A powerful but user friendly graphical interface for FLUKA*, *International Conference on Mathematics, Computational Methods & Reactor Physics*, p 11, 2009.
- [48] *SHOE Reconstruction software*, <http://arpg-serv.ing2.uniroma1.it/twiki/bin/view/Main/FOOTReconstruction>